Department of Precision and Microsystems Engineering

Design of an Integrated Photonic Distributed Force Sensor

Xu-Feng Eric Hsu

Report no : 2023.036

Coach : W.J. Westerveld, G.J. Verbiest

Specialisation : Engineering Dynamics

Type of report : Master's thesis
Date : June 28th, 2023



Design of an Integrated Photonic Distributed Force Sensor

By

Xu-Feng Eric Hsu

A thesis submitted in partial fullfilment of the requirements for the degree of Master of Science in Mechanical Engineering

Student number: 5630126

Project duration: August 1st, 2022 - June 28th, 2023

Thesis committe: Dr. W.J. Westerveld TU Delft, Supervisor

Dr. G.J. Verbiest TU Delft, Supervisor

Dr. M. Mirzaali Mazandarani TU Delft, External Member



Acknowledgements

I would like to thank Wouter Westerveld, Tufan Erdogan, Gerard Verbiest and Mohammad Mirzaali for assisting my thesis at different times throughout the year. They have introduced me to the research field of integrated photonics, given me the background of the cohesion project as well as given me tips on all aspects of the thesis. I also want to thank all W-Lab members for the meetings we had where I could share my progress. With the end of my thesis, I would like to hand over my results to the new PhD candidate Sahar, who will continue working on the cohesion project and wish everyone involved in that project the very best of luck.

Finally, I would also like to thank my mother and my brother for their continuous support throughout my years in graduate school.

 $Xu ext{-}Feng\ Eric\ Hsu$ $Delft,\ June\ 2023$

Abstract

From the research in the field of mechanobiology, it is evident that cells exert different force magnitudes while growing based on the biomaterial these are in contact with. The magnitude of the exerted force determines certain behaviors and mechanisms of the cells, such as differentiation. For this reason, it is proposed to develop a distributed force sensor using a photonic integrated circuit with a PDMS top layer to measure the exerted forces, which can be used to study the behavior of the cells. Unlike conventional measurement techniques, this method allows cell exerted distributed forces at μN levels to be detected and monitored over a continuous time-span of multiple days and weeks. The photonic integrated circuit design consists of a 28 × 28 array of silicon photonic ring resonators for force sensing with radii of around $2 \mu m$ and a ring resonator spacing of $8\,\mu m$ in both the vertical and horizontal directions. On each sensor row, three reference ring resonators are applied as well to cancel out the spectral noise caused by temperature drifts and laser wavelength repeatabilities. The reference ring resonators are shielded against cell exerted forces with a commercial hybrid-polymer called Ormocore, which has a Young's modulus of around 1 GPa. Using three reference ring resonators resulted in a theoretical measurement resolution of potentially as small as approximately 0.012 pm. The force sensing and reference ring resonator have waveguide cross-sections of $450 \times 220 \, nm$ and $410 \times 220 \, nm$ respectively. Both ring resonator types also have an inner slab layer with a thickness of $100 \, nm$ to increase the confinement of the electromagnetic field that is propagating inside the ring resonators. Finally, the force limit-of-detection of the designed distributed force sensor remains below $1 \mu N$ when the force exertion area does not exceed $100 \mu m^2$ and assuming a sensitivity of $65.41 \, nm/RIU$ for one of the multiplexed ring resonators.

Contents

1	Intr 1.1	oduction Project Motivation	6
	$1.1 \\ 1.2$	Proposed Sensing Method and Scope	
	1.3	Requirements	
			_
2			10
	2.1	Light Propagation in Integrated Photonic Waveguides	
	2.2	Interrogation	15
3	Desi	ign Concept Selection	16
	3.1		16
	3.2	Waveguide Geometries	17
	3.3	Integrated Photonic Sensing Devices	
	3.4	Methods for Temperature Drift Compensation	24
	3.5	Array Configurations of Integrated Photonic Sensing Elements	25
4	Inte	errogation Performance of Integrated Photonic Resonators	27
•	4.1	Measurement Resolution and Limit-of-Detection	
	4.2	Performance Determination in Presence of Intensity Noise	
5			33
	5.1	Device Specifications	
	5.2	Waveguide Bend Loss Modeling	
	5.3	· · · · · · · · · · · · · · · · · · ·	36
	5.4	Coupling Simulations	
	5.5	Temperature Drift Modeling	
	5.6	Cross-Talk Analysis	41
6	Fab	rication Error Analysis	43
	6.1	Wafer-Scale Dimension Deviations	43
	6.2	Die-Scale Dimension Deviations	43
	6.3	Sidewall Roughness and Absorption Loss	49
7	Res	ults	53
•	7.1	Medium-Sized Sensor Design	
	7.2	Small-Sized Sensor Design	
	7.3	Chip Design and Fabrication	
	7.4		72
6	D!		75
8	8.1		77 77
	8.2	Intrinsic Ring Resonator Performance	
	8.3	Interrogation Performance	
	8.4	Distributed Force Sensor Design	
	8.5		78

9	Conclusion and Outlook	79
	9.1 Conclusion	
	9.2 Outlook	80
Bi	bliography	87
A	CMOS Fabrication Process Flow	88
\mathbf{B}	Polymer Cladding Fabrication Process Flow	90

Chapter 1

Introduction

Anno 2022, a collaboration project between Wouter J. Westerveld (TU Delft, Precision and Microsystems Engineering) and Mohammad J. Mirzaali (TU Delft, Biomechanical Engineering) is running to develop a novel sensing platform for mechanobiological analysis of cells. Part of this research is to develop a new array of integrated photonic sensors to meassure the mechanical and molecular properties of cells at high spatial resolutions. Photonic integrated circuit (PIC) is a microchip that can manipulate light at microscale by guiding light through fiber-like structures called waveguides. Part of the light that is guided through the waveguide will leak out and interact with the medium or material that is surrounding the waveguide. In this case, a polymer layer is applied on top. More of it will be explained in section 1.2. This way, (distributed) force of cells can be sensed by detecting refractive index changes of the polymer layer caused by the force of cells. Photonic integrated circuit is a promising method to sense the cellular forces, as it has been shown that for example highly sensitive and compact biosensors can be created with it [1].

1.1 Project Motivation

In the field of mechanobiology, it has been shown that different mechanical and physical cues of cells, for example elastic stiffness, shear stress, local geometries and surface properties, could indicate certain cell growth, proliferation and differentiation [2][3]. The behaviors of these biophysical cues are complex processes, which makes it still unclear how each individual cue or combined cues affects the cell mechanisms, notably the mechanotransductions which modulates the tissue growth and remodelling. Therefore, it is important to accurately measure the forces exerted by the cells while these are growing over a span of days and weeks in order to analyze and understand the cell behaviors and mechanisms. The cell force sensing method must satisfy the following requirements.

- Cell exerted force detection limits at the micronewton level.
- Real-time force sensing over a span of potentially multiple days and weeks.
- Distributed cell exerted force sensing.
- Submersion in solution to allow nutrients to be provided to the cells in order for these to grow.

There are different existing methods for measuring cellular forces (see Figure 1.1) which are explained in the next subsections.

1.1.1 Traction Force Microscopy

Traction force microscopty (TFM) can measure cell forces by putting cells on top of a synthetic elastic polymer layer. This layer can deform as a result of the traction force exerted by the cells. Due to this, the beads that are placed inside the polymer layer will displace as well. The displacement can be tracked using imaging analysis and the force required for the displacement to happen can subsequently be deduced. Forces smaller than $1 \mu N$ are detectable with TFM [4]. However, the drawbacks of TFM is its sensitivity to experimental noise (i.e. low microscope resolution, image processing uncertainties and non nonhomogeneities in in the polymer layers) [5].

1.1.2 Micropillars

Micropillars measures cell forces by determining the deflection of the pillars due to forces exerted by the cells. The deflection can be determined by using optical microscopy [6]. When knowning the deflection, the exerted force can be determined using linear beam theory. Forces smaller than $1 \mu N$ are detectable with micropillars [4]. However, it has also been shown that pillars with small diameters and seperation distances ($< 1 \mu m$) can map a more detailed cell force distribution due to better mimicing a continuous adhesion surface with the cell.

1.1.3 Cantilever

Cantilevers of atomic force microscopes (AFM) have been used to measure single cell force [7]. The cantilever is placed on top of the cell and gets deformed due to forces exerted by the cell. The force detection limit goes down to pN levels. However, this method only allows a single or few forces to be measured instead of measuring force distribution over an area.

1.1.4 Comparison of Force Sensing Methods

The comparison of different force sensing methods using the aforementioned requirements is shown in Table 1.1.

Sensing	μN force	Continuous sensing over	Distributed	Allowing for
method	\det ection	${ m multiple\ days/weeks}$	force sensing	$\operatorname{submersion}$
TFM	1	✓	✓	Х
Micropillar	✓	X	✓	X
Cantilever	✓	X	X	X

Table 1.1: Comparison of existing force sensing methods for detecting forces exerted by biological cells

All three sensing methods can detect cell exerted forces at μN levels. However, only the TFM can potentially allow force sensing in a time-span of multiple days and weeks. Unlike TFM, the cells are fixated on the micropillar and the cantilever. The cell fixation prevents the cells from growing beyond the pillars and cantilevers that have already been covered by the cells, making these options only suitable for short-term force sensing. Also, the cantilever method is the only option that can measure cell exerted force at a single location, making distributed force sensing with this method impossible. Finally, none of the three options allow to be submerged for providing nutrients to the cells. The reason for this is that submerging entire imaging devices, microscopes (for TFM and micropillars) or AFM systems (for the cantilever sensing method) is unsuitable. The liquid solution will also make image analysis even more difficult.

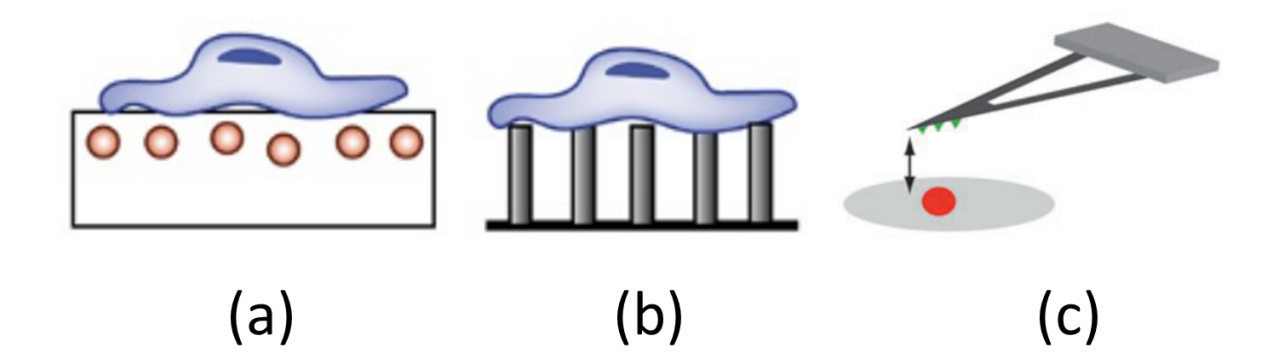


Figure 1.1: (a) Traction force microscopy [8], (b) micropillars [8], AFM [7]

1.2 Proposed Sensing Method and Scope

Because of the limitations of the existing cell force sensing methods, it has been proposed to use photonic integrated circuits to measure the forces exerted by the cells due to the high precision sensing capabilities and small footprints of integrated photonic devices. The current sensing method or measurement platform proposal

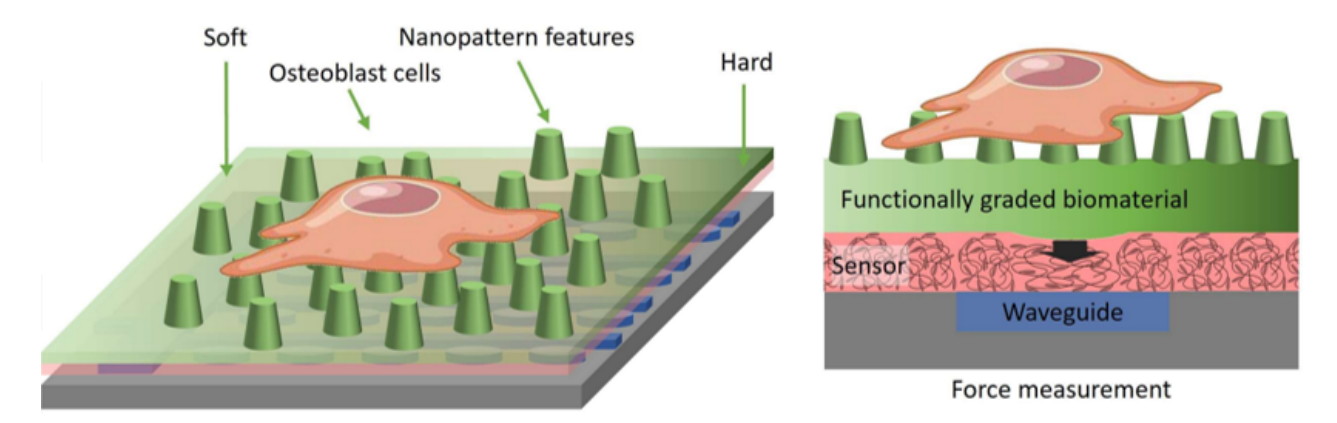


Figure 1.2: Proposed measurement platform

The proposed measurement platform consists of a biomaterial and an elastic polymer layer put on top of a photonic integrated circuit. Forces exerted by cells go through the biomaterial and causes the polymer layer to deform and strain. Due to the photoelastic effect [9], the strain of a material causes its refractive index to change as well. Subsequently, the change of refractive index of the polymer layer can alter the light signal that goes through the photonic integrated circuit. Therefore, the alteration of the light signal can be used to detect cell exerted forces.

With integrated photonics, all the requirements as shown in Table 1.1 can (potentially) be satisfied. Using an elastic polymer cladding for refractive index sensing, forces of below $1\,\mu N$ can in theory be detected as shown in section 7.4. Due to a lack of cell fixations, the cells can grow freely, making force sensing over multiple days and weeks possible. Using small integrated photonic sensors (as explained in section 3.3), an array of force sensors can be developed, allowing it to sense distributed forces. Finally, the photonic integrated circuit can be submerged in liquid while being connected to the outside world (i.e. laser and photodetector) using fiber-optics (see Figure 2.4). Unlike integrated photonic refractive index sensors, the footprint of optomechanical sensors (i.e. sensors that utilize both optical as well as mechanical structures such as membranes or cantilevers) are much larger in order measure small forces [10][11][12][13], making it very hard to develop compact sensor arrays with it.

This thesis focuses on designing a distributed integrated photonic sensor that can detect static forces. This includes a mask design of the photonic integrated circuit that can be used to fabricate the sensor using CMOS process (a fabrication process that has already been utilized for fabricating electronic chips) as well as analytical and numerical calculations to theoretically describe the sensor performance. These goals will contribute to the overall research collaboration between Westerveld and Mirzaali by providing a photonic integrated circuit that is suitable for meassuring (distributed) static forces of cells as well as the knowlegde of designing such sensor (i.e. what methods are possible to improve the sensor performance and compactness in the case of distributed static cell force sensing etc.). However, the design of the polymer cladding that exhibits high photoelastic response for refractive index sensing is outside of the scope of the thesis, although the presence of such material (and its optical properties) on top of the photonic integrated circuit will be taken into account.

1.3 Requirements

From the start of the cell measuring research collaboration, several requirements are created for the distributed force sensor.

- Micronewton force limit-of-detection: The forces exerted by biological cells are very small. The distributed force sensor must have the capabilities to detect forces at micronewton levels.
- Measuring cell mechanics: to enable cell sensing, a polymer layer must be put on top of the distributed force sensor. The polymer acts as a cladding of which the refractive index can change if cell force is subjected to it. Since this thesis assignment is carried out at a very early stage of the research collaboration, the polymer type is unknown.

- High spatial sensing resolution: the distributed force sensing elements must be around $5 \mu m$ to $10 \mu m$ separated from each other.
- Simultaneous interrogation of multiple sensing elements: the distributed force sensor will have many sensing elements, partially caused by the requirement for high spatial sensing resolution. To increase productivity, the user should be able to detect forces from multiple sensing elements at the same time.
- Fabrication at Cornerstone: Cornerstone is a (photonic chip) foundry in the UK, which is the currently the main provider of photonic integrated circuits for W-Lab. Due to the fact that the entire measurement platform (i.e. photonic integrated circuit, polymer cladding and cells) are comsumables, the cost of each die (i.e. chip on a wafer) becomes more important. In that case, having the photonic integrated circuits made by Cornerstone is from a financial standpoint a viable choice.

Chapter 2

Background

In this section, the waveguide theory of integrated photonics and the requirements of the distributed force sensor will be discussed.

2.1 Light Propagation in Integrated Photonic Waveguides

In this section, light propagation in slab waveguides (i.e. a 2D problem) is initially studied and later expanded upon to analyze rectangular waveguides (i.e. a 3D problem). Slab waveguides are 2D representations of a waveguide, consisting of three layers: a core layer representing the light guiding structure that is sandwiched between two outer layers. The thickness of the core layer is finite, while its width is considered to be infinite due to the two-dimensional representation of a waveguide. Light propagation in slab waveguides can be described with both geometrical optics and wave optics. Afterwards, the slab waveguide theory based on wave optics will be expanded to describe the light propagation in a rectangular waveguide, which considers both the width and the height to be finite. The theory in this section closely follows the work from Westerveld et. al.[14][15] and Reeds et al. chapter 2 [16].

2.1.1 Slab Waveguides described by Geometrical Optics

Light can travel in a medium (core) with outer media surrounding it that have refractive indices different compared to the core medium by internally reflecting at the interfaces. The light interaction at this interface can be described with Snell's law:

$$n_1 sin(\theta_1) = n_2 sin(\theta_2) \tag{2.1}$$

where n_i , i = 1, 2 are the refractive indices of the media of interest and θ_i , i = 1, 2 are the angles of incidence and refraction respectively. When n_1 is larger than n_2 , then the refraction angle θ_2 becomes 90° if θ_1 is large enough. In that case, θ_1 becomes the critical angle, which is determined by substituting $\theta_2 = 90^\circ$ in Equation 2.1 and rewriting it to:

$$sin(\theta_c) = \frac{n_2}{n_1} \tag{2.2}$$

where θ_c is the critical angle. When $\theta_1 > \theta_c$, no light will be transmitted to the second medium, as all the light gets internally reflected in the medium of incidence. When this happens multiple times as shown in Figure 2.1, then light can propagate forward in a fiber-optic stucture.

2.1.2 Slab Waveguides described by Wave Optics

Light propagation in integrated photonics waveguides can also be described by propagating electromagnetic waves in linear and passive materials. Linear materials means that light propagates through a linear isotropic dielectric material, indicating a material polarization direction that is propertional to the one of the electric field E and a polarization magnitude that is independent of the electric field direction. Also, photonic integrated circuits do most of the time not have (light) sources, meaning the utilized materials are passive (they do not induce electric and magnetic fields). This means that both the current of the electric charge and the electric charge density can be omitted from the Maxwell's equations. Furthermore in Westerveld et. al., the

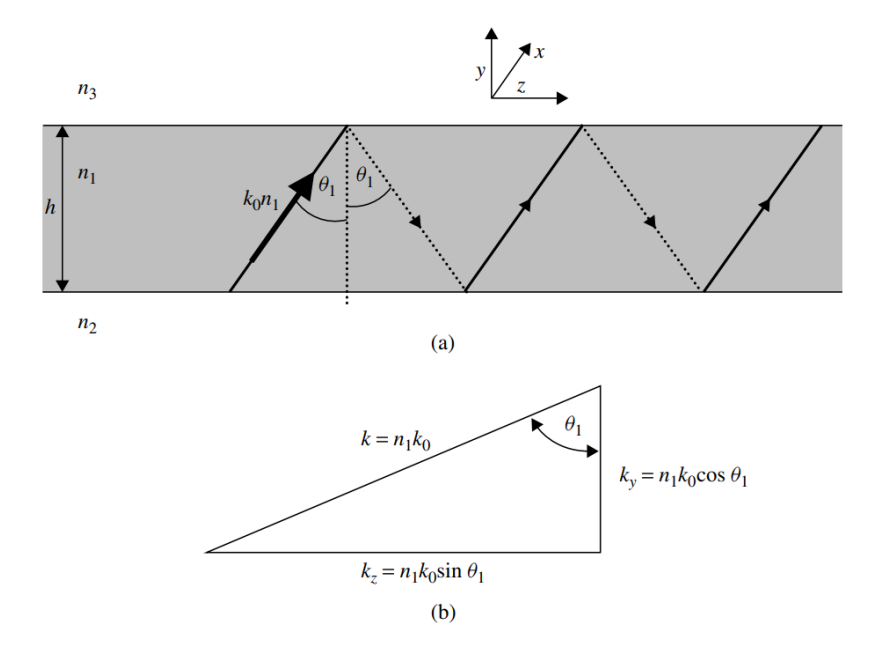


Figure 2.1: (a) Total internal reflection in a waveguide (b) wavevectors in y,z-direction [16]

permeability μ and optical properties (e.g. angular frequency ω and wavelenth λ) is taken in vaccuum and the light is considered monochromatic.

An electromagnetic wave contains both the electric field E and the magnetic field H. Both fields are plane harmonic waves and can be expressed with the complex exponential function.

$$E = E_0 e^{i(kz \pm \omega t)} = E_0 e^{i\theta} \tag{2.3}$$

$$H = H_0 e^{i(kz \pm \omega t)} = H_0 e^{i\theta} \tag{2.4}$$

where E_0 and H_0 are the amplitude of the electric and magnetic field respectively and θ is the phase of the wave. kz, where $k=2\pi/\lambda$ (with λ being the free-space wavelength) is the free-space wavenumber and z is the respective propagation direction, represents the spatial phase. ωt is the phase varying over time t, where $\omega=2\pi f$ is the angular frequency of the wave. Finally, the exponetial term of Equation 2.3 and Equation 2.4 represents the oscillatory part, since $e^{i\theta}=\cos(\theta)+i\sin(\theta)$.

The wavevectors defined in Equation 2.3 and Equation 2.4 can subsequently be applied to the geometrical optics model of light propagation in a slab waveguide, as explained in section 2.1. The reason for this is to add "phase" in the rays of the geometrical optics model. As a result, the zig-zag path of the light can be divided into a horizontal propagation and a vertical reciprocal propagations. The propagation constants or wavevector of each of these three propagation directions are:

$$k = k_0 n_1 \tag{2.5}$$

$$k_y = k_0 n_1 cos(\theta_1) \tag{2.6}$$

$$k_z = k_0 n_1 \sin(\theta_1) \tag{2.7}$$

where k_0 is the wavenumber in vaccuum space. These wavevectors are also illustrated in Figure 2.1. Propagation constant k_z is often written as β , which will also be denoted as in this report from now on. Since the propagation in the y-direction is reciprocal, it is considered a standing wave, completing a round trip after each zig-zag propagation. If the height of the waveguide is equal denoted as h, then the phase shift in the y-direction can be defined in the following way:

$$\theta_y = 2k_y h = 2k_0 n_1 h \cos(\theta_1) \tag{2.8}$$

In order for light to propagate along a waveguide, the total phase shift of the light propagation must be a multiple (m) of 2π to ensure constructive interference after a single round-trip.

$$\theta_y - \theta_u - \theta_l = 2\pi m \tag{2.9}$$

where θ_u and θ_l is the phase delay due to the reflection in the upper and lower interface of the slab waveguide respectively.

From the wavevectors, propagation constant in the z-direction β describes the propagation rate of light along the waveguide length direction. Due to the fact that part of the light leaks out of the waveguide during propagation (which will be explained in more detail later in this section), the light bundle will travel through media with multiple different refractive indices simultaneously The multiple different refractive indices can also be denoted as a single effective refractive index n_e , which is only applicable to light propagation along the waveguide length direction (in this case it is the z-direction). The effective index can be determined with the following equation:

$$n_e = \frac{\beta}{k_0} \tag{2.10}$$

The effective group index n_g can be approximated as the first-order dispersion in the effective index.

$$n_g(\lambda_c) \equiv \frac{\partial \beta}{\partial k} = n_e(\lambda) - \lambda \frac{\partial n_e}{\partial \lambda}$$
 (2.11)

where wavelength dependence as a linear function has been applied to n_e and a center wavelength dependence (λ_c) as a linear function to n_g . The center wavelength is the wavelength around which the function is linearized. $\partial n_e/\partial \lambda$ can be determined by taking a center wavelength dependence of the effective index $(n_e(\lambda_c))$ and subsequently rewriting Equation 2.11 with $n_e(\lambda_c)$ and $\lambda = \lambda_c$ substituted in it. For photonic integrated circuits, the telecom wavelength (1550 nm) is usually taken as the center wavelength. After determining $\partial n_e/\partial \lambda$ and considering $k = 2\pi/\lambda$, the phase delay with an arbitrary wavelength dependence can be expressed in the following equation:

$$\beta(\lambda) \equiv n_e(\lambda)k = 2\pi \left(\frac{n_e(\lambda_c) - n_g(\lambda_c)}{\lambda_c} + \frac{n_g(\lambda_c)}{\lambda}\right)$$
(2.12)

When considering that light propagates through multiple refractive indices simultaneously due to evanescent fields, the wavenumber k from plane harmonic wave equations Equation 2.3 and Equation 2.4 is replaced by the propagation constant in the z-direction (β) , resulting in the following equations.

$$E = E_0 e^{i(\omega t - \beta z)} \tag{2.13}$$

$$H = H_0 e^{i(\omega t - \beta z)} \tag{2.14}$$

where the sign notation $\omega t - \beta z$ that is different from Equation 2.3 and Equation 2.4 is taken from Westerveld et. al. [14].

Slab waveguides being planar means that it has an infinite width w in the x-direction and therefore the change of electric and magnetic field is equal to zero in that direction $(\partial/\partial x = 0)$. Substituting this condition in the Maxwell's equations result in equations of which the electric and magnetic field terms are divided between E_x , H_y , H_z and H_x , E_y , E_z . The solution of the Maxwell's equations with the first combination of field terms result in mode fields of a TE mode, while the solution of the latter combination result in mode fields of a TM mode. In a slab waveguide, TE mode means the electric field is only in the x-direction, while for TM mode the magnetic field is only in the x-direction.

Any mode field can be determined by solving the Helmholtz equation, which is an eigenvalue problem derived from the Maxwell's equations. In the case of a slab waveguide with TE mode, invariance in the x-direction and an effective propagation in the z-direction, the Helmholtz equation can be written as the following:

$$\frac{\partial^2 U}{\partial y^2} = (\beta^2 - \omega^2 \mu_0 \epsilon_0) U$$

$$= (\beta^2 - k^2 n_i^2) U$$

$$= -k_y^2 U$$
(2.15)

where U can be either E_x , H_y , H_z for TE modes. The following equations are also applied.

$$k = \frac{2\pi}{\lambda_0} = \frac{\omega}{c} \tag{2.16}$$

$$\frac{1}{c^2} = \mu_0 \epsilon_0 \tag{2.17}$$

k and n_i are the wavenumber in the resulting propagation direction of light and the refractive indices of the slab waveguide layers (e.g. core or cladding depending on the layer that is being studied) respectively. λ_0 is the wavelength of the plane harmonic wave in vacuum. k_y is the wavenumber in the y-direction, which according to Equation 2.15 is defined as:

$$k_y = \sqrt{k^2 n_i^2 - \beta^2} (2.18)$$

The sign of k_y can change depending on the slab waveguide layer. In the case of the core layer, $k^2 n_{core}^2 > \beta^2 > k^2 n_{clad}^2$. Since in this case $n_i = n_{core}$, k_y is positive, resulting in the Helmholtz equation as shown in Equation 2.15. On the other hand, when $\beta^2 < k^2 n_{clad}^2$ and thus $n_i = n_{clad}$, k_y will be negative instead. This results in the following Helmholtz equation for solving the TE mode outside the core layer.

$$\frac{\partial^2 U}{\partial x_i^2} = k_y^2 U \tag{2.19}$$

Solving the Helmholtz second order differential equations result in the following TE and TM mode field.

$$E_{x}(y) = \begin{cases} E_{up}exp\left[-\gamma_{y,up}(y - b/2)\right] & y > -b/2\\ E_{core}cos(k_{y}y) & b/2 \ge y \ge -b/2\\ E_{low}exp\left[\gamma_{y,low}(y + b/2)\right] & y < -b/2 \end{cases}$$

$$\begin{cases} H_{exp}\left[-\gamma_{y,up}(y - b/2)\right] & y > -b/2\\ H_{exp}\left[-\gamma_{y,up}(y - b/2)\right] & y > -b/2 \end{cases}$$
(2.20)

$$H_{x}(y) = \begin{cases} H_{up}exp\left[-\gamma_{y,up}(y - b/2)\right] & y > -b/2\\ H_{core}sin(k_{y}x) & b/2 \ge x \ge -b/2\\ H_{low}exp\left[\gamma_{y,low}(y + b/2)\right] & y < -b/2 \end{cases}$$
(2.21)

where all the modal amplitudes are chosen that satisfies the boundary conditions at the interfaces (i.e. the field magnitude of both the core layer and the evanescent field are equal to each other). Also the following equations have been used for γ_i :

$$\gamma_j = \sqrt{\beta^2 - k^2 n_j^2} = \sqrt{k^2 (n_{core}^2 - n_j^2) - k_y^2},$$
(2.22)

where j denotes the outer layers of a slab waveguide. Equation 2.20 can be also used to determine the magnetic field modes of TE and Equation 2.21 for the electric field modes of TM. Westerveld et. al. [14] have shown that Equation 2.20 and Equation 2.21 can be used to calculate the only unknown k_y , which in turn can be substituted back into the same equations in order to plot the modal fields of a slab waveguide.

2.1.3 Rectangular Waveguides

Light propagation in rectangular waveguides can be analytically approximated by placing both a dominant electric and magnetic field of a slab waveguide orthogonal to each other in a 2D refractive index profile n(x, y), as shown in Figure 2.2. It can be seen from Figure 2.2 that there are five regions of interest. A core region (1) and the surroundings (2-5). The corner regions are neglected, since the light intensities are low there. Due to the fact that both the width and the height of the waveguide are finite, light can propagate in all three directions now. This means that electric and magnetic fields in all directions are present, no matter the mode. That is why the modes in rectangular waveguide are sometimes called "TE-like" and "TM-like". The electric field of the TE-like modes are mostly normal to the side-walls, while the electric fields of the TM-modes are for the most part located at the top and bottom surface of the waveguide. For this reason, the propagation constant β can be determined with the following equation:

$$\beta = \sqrt{n_1^2 k^2 - k_x^2 - k_y^2} \tag{2.23}$$

where k_y can be determined from the slab waveguide theory as explained in subsection 2.1.2. k_x is similar to k_y , but for TM mode instead. The propagation constant β can then be used to determine the effective refractive index of the rectangular waveguide with Equation 2.10.

Similar to Westerveld et. al. [15], a coordinate system is taken such that E_x is the biggest electric field and H_y is the dominant magnetic field. In Figure 2.3, the equations modal field shapes of the rectangular waveguide

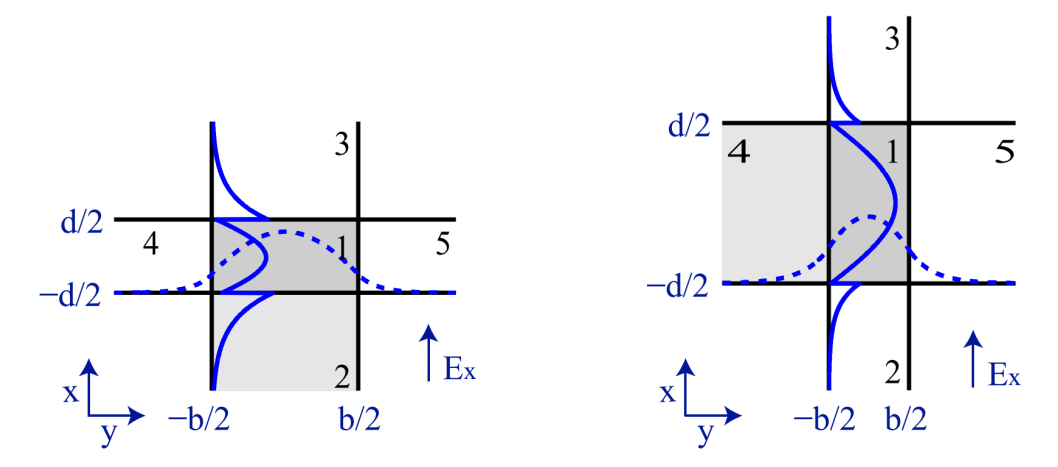


Figure 2.2: Left: fundamental TM-like mode with region 2 being the BOX layer, right: fundamental TE-like mode with region 4 being the BOX layer. This is due to the orientation of the electric field E_x . [15]

(a)	region 5:	y x
	$E_x \propto \cos[k_x(x+\xi)]$ $\cdot \exp[-\gamma_5(y-b/2)]$	
	$\exp[-\gamma_5(y-b/2)]$	
region 2:	region 1:	region 3:
$E_x \propto \exp[\gamma_2(x+d/2)]$	$E_x \propto \cos[k_x(x+\xi)]$	$E_x \propto \exp[-\gamma_3(x-d/2)]$
$\cdot \cos[k_y(y+\eta)]$	$\cdot\cos[k_y(y+\eta)]$	$\cdot\cos[k_y(y+\eta)]$
	region 4:	
	$E_x \propto \cos[k_x(x+\xi)]$ $\cdot \exp[\gamma_4(y+b/2)]$	
	$\cdot \exp[\gamma_4(y+b/2)]$	

(b)	$E_z = A_9 \sin[k_x(x+\xi)]$ $\cdot \exp[-\gamma_5(y-b/2)]$ $H_z = A_{10} \cos[k_x(x+\xi)]$	y
	$\cdot \exp[-\gamma_5(y-b/2)]$	
$E_z = A_3 \exp[\gamma_2(x + d/2)]$	$E_z = A_1 \sin[k_x(x+\xi)]$	$E_z = A_5 \exp[-\gamma_3(x - d/2)]$
$\cdot\cos[k_y(y+\eta)]$	$\cdot \cos[k_y(y+\eta)]$	$\cdot\cos[k_y(y+\eta)]$
$H_z = A_4 \exp[\gamma_2(x+d/2)]$	$H_z = A_2 \cos[k_x(x+\xi)]$	$H_z = A_6 \exp[-\gamma_3(x - d/2)]$
$\cdot \sin[k_y(y+\eta)]$	$\cdot \sin[k_y(y+\eta)]$	$\cdot \sin[k_y(y+\eta)]$
	$E_z = A_7 \sin[k_x(x+\xi)]$	
	$\cdot \exp[\gamma_4(y+b/2)]$	
	$H_z = A_8 \cos[k_x(x+\xi)]$	
	$\cdot \exp[\gamma_4(y+b/2)]$	

Figure 2.3: (a) Mode shape equations of a rectangular waveguide (b) Modal amplitudes A_i , i=1,2,...10 [14]

is shown. All transverse fields (E_x, E_y, H_x, H_y) can be expressed in terms of fields parallel to the propagation direction (E_z, H_z) .

It can also be seen from Figure 2.3 that there are ten field amplitudes $(A_i, i = 1, 2, ...10)$ in the mode field equations. This is an *ansatz* that is made to satisfy the Maxwell's equations in all five regions, with some

errors present at the interfaces of these regions. The field amplitudes should be chosen in order to ensure accurate continuity of electromagnetic fields tangential to these interfaces. If that is the case, then the normal electromagnetic fields will obey the Maxwell's equations. There are different approximate methods to calculate these modal amplitudes. A famous example is the Marcatili's method [17], where H_x is set to zero in order to satisfy the boundary condition at interface 1-2 and 1-3 at the cost of the continuity at interface 1-4 and 1-5. Instead of $H_x = 0$, E_y can be set to zero instead [17][18], but continuity quality of all interfaces swap. Westerveld et. al. [15] have developed a method that optimizes and minimizes all the amplitude field mismatches (that result in interface continuity errors) by analyzing the average energy densities of the discontinuities. This method, which is called Amplitude Optimization, gives full field profiles that are more accurate than Marcitili's approach (which is also not limited to low-index-contrast waveguides) and will therefore be used in this thesis for fast explorative modeling of the distributed force sensor. The Amplitude Optimization method can be performed with an open-source Matlab code [19].

2.2 Interrogation

The method of providing light sources for the photonic integrated circuit and determining changes in external factors (e.g. force or temperature) is often referred as interrogation, as shown in Figure 2.4. Typically a (wavelength) tunable laser, a broadband laser or a monochromatic laser are used as light sources for interrogations, depending on the application. Light from these light sources are coupled onto the chip via e.g. fiber-optics or in free space. Out-of-plane grating couplers is one way to couple light. These have limited supported bandwidth of e.g. $30\,nm$ [14]. Afterwards on the chip, light is used to detect cell forces. For the distributed cell force sensor, the detection of static force changes is done by sensing the refractive index changes of the cladding material (a polymer in this case) caused by static force changes. Cladding refractive index can be sensed due to the fact that part of the light in the waveguide leaks out and is essentially also propagating through the cladding, as explained in subsection 2.1.2. The alteration of the light signal as a result of changes in static external factors is usually in the form of a shift in resonance peaks for resonator devices or a phase shift for interferometers. Altered light signals due to static force changes is then coupled away from the chip using an out-of-plane grating coupler as well and sent to a photoreceiver. Finally, an oscilloscope can be used to read the light signal changes (due to force exertion of the biological cells).

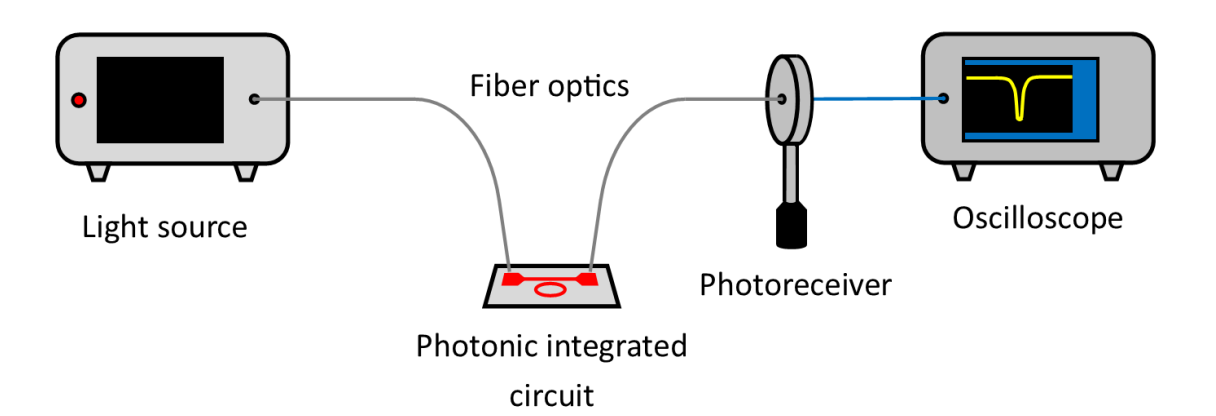


Figure 2.4: Schematic interrogation setup

Chapter 3

Design Concept Selection

In this section, different aspects of integrated photonics are analyzed to check the suitability for distributed biological cell force sensing. It starts with the study of possible material platforms. Then different waveguide geometries are considered. Afterwards, several integrated photonic sensing devices are analyzed. Finally, multiple approaches to compensate temperature drift as well as integrated photonic sensor array configurations are studied as well.

3.1 Material Platforms

Different materials can be utilized to develop photonic integrated circuits. The design criteria that are important for material platforms are the possibility of designing small-sized integrated photonic devices, the possibility of designing a sensor array that can cover the $80 \times 80 \,\mu m$ biological cell and low-cost PIC fabrication. Designing small-sized devices is possible if the minimum waveguide bends using a certain material platform is also small (i.e. $R < 3 \,\mu m$). The cost of fabricating PIC's can be brought down by using material platforms that are CMOS-compatible, since CMOS fabrication processes are already being widely used for the semiconductor industry. As an example, Cornerstone can provide DUV projection lithography service for $200 \, nm$ SOI-wafer costing around 2300 euros per wafer. Finally, when the light propagation loss in a certain material platform is high, the size of the integrated photonic device and therefore the entire sensor array fabricated from that material will be limited in size, making it difficult to cover the entire biological cell.

3.1.1 Silicon Photonics

Silicon is the most common material platform for developing photonic integrated circuits. The most important aspect of silicon photonics is the availability of high-end fabrication. The existing CMOS-compatible processes for the semiconductor industry (i.e. fabrication processes and tools) can be also used to fabricate silicon photonic chips. A silicon-on-insulator (SOI) wafer is used to fabricate silicon photonic devices, which consists of three different layers: a bottom silicon substrate layer, a buried SiO_2 (BOX) layer in between and a silicon layer on top of the SiO_2 layer. The latter layer gets etched in order to manufacture waveguides and other integrated photonic devices. The high refractive index of silicon $n_{Si} = 3.46$ allows for very high confinement of light due to the high refractive index contrast with the cladding, which makes small waveguide bending radii ($<= 3 \,\mu m$) possible [14][20]. Similar to silicon-on-insulator, silicon nitride Si_3N_4 is another material platform that is CMOS compatible. Notable aspects of Si_3N_4 include wide operable wavelength range ($400-2350\,nm$) and low propagation losses due to its transparency [21]. However, it is shown that the minimum bending radius for silicon nitride waveguides is from $50\,\mu m$ to milimeter scales [22][23], which is unideal for densely integration of small force sensors.

3.1.2 Non-Silicon Platform

Both III-V materials and metals are other options used to develop integrated photonic sensors. Indium phosphide (InP) is a common platform among III-V materials. The bending radii of InP waveguides can be as small as $10 \,\mu m$ [24]. Unlike silicon, InP is not CMOS-compatible. As for metals, light can be confined and guided along metal-dielectric interfaces. These types of waveguides are also known as plasmonic waveguides. In this way, very small waveguide bends can be made [25][26]. However, it has been shown that waveguide losses are high

[27]. Different metals can be used to fabricate plasmonic devices. However, CMOS-compatibility depends on the metal type [28].

3.1.3 Comparison of Material Platforms

The overview of possible footprint and costs of different material platforms are shown in Table 3.1.

Material Platform	Possible Footprint in	CMOS-compatibility	Additional notes
	Bending Radius		
Silicon	$<=3\mu m$	Compatible	-
Silicon Nitride	$=50\mu m$	Compatible	-
Indium Phosphide	$=10\mu m$	${\bf Incompatible}$	-
Metals	$< 1 \mu m$	Depends on the metal	High propagation losses

Table 3.1: Comparison of material platforms

It can be seen that silicon material platofrm shows both small possible waveguide bends and CMOS-compatibility. The former makes designing small integrated photonic devices possible, while the latter is more economical due to the CMOS-compatibility. Due to a large minimum bending radius, the footprint of devices from silicon nitride are also very large. Unlike silicon, indium phosphide devices are more expensive to fabricate since this material is not CMOS-compatible. Finally, plasmonic devices may look promising at first due to the possible small footprint (due to small possible waveguide bends) and CMOS compatibility. However, the high propagation losses makes it impossible to design a large sized distributed force sensor. In conclusion, silicon-on-insulator is the most ideal platform for this project. Therefore, this material platform with be considered in the next sections.

3.2 Waveguide Geometries

The shape of a waveguide can have an effect on optical properties e.g. light confinement, propagation losses and mode intensity distributions. In this section, strip, rib, sub-wavelength and photonic crystal waveguides are discussed.

3.2.1 Strip Waveguides

Strip waveguides are the most general type of waveguides. These are rectangular shaped and its optical properties can be accurately described by the rectangular waveguide theory, as explained in subsection 2.1.3. In practice due to the etching process, the side-walls of the waveguide can be slanted, creating a trapezoidal-shaped waveguide instead. However, it has been shown that its effective (group) index can be approximated with a rectangular waveguide having width that is the average of the trapezoidal waveguide [14]. It should be noted that the slanted side-walls can cause a mode conversion, which is a source of propagation loss [29]. Other losses for strip waveguides are scattering due to side-wall roughness [30], radiation due to bending [14] and absorption of materials (depending on the propagation wavelength) [31]. Also from the analysis using RectWG, strip waveguides with lower width and height result in higher sensitivities (which is a sensor performance criteria and will be explained in more detail in subsection 3.3.1) due to the lower light confinement that causes larger evanescent fields. Strip waveguide dimensions of around 450x220 nm are very common, but the height is usually decreased to 150 nm or even 90 nm for increased light interaction with the cladding [32].

3.2.2 Rib Waveguides

Rib waveguides are low thickness strip waveguides (also called the ridge part) stacked on top of a slab layer made from the same material. To fabricate this structure from SOI, a silicon layer must be partially etched in order for the slab layer to remain. As explained in subsection 3.2.1, this etch process causes side-wall roughness, which can cause propagation losses. Due to the absence of side-wall roughness in the slab layers, the mode fields only experience the side-walls/interface at the ridge part, reducing the scattering loss. Rib waveguides with very low propagation losses of below $0.5 \, dB/cm$ at a wavelength of $1550 \, nm$ have been shown [33][34]. The slab part of the rib waveguide results in low light confinement [31]. Since the slab waveguide is made from the same material as the ridge part, the effective index contrast between the side cladding and the ridge waveguide will be very small. At rib waveguide bends, the mode that is propagating in the ridge part will for this reason leak

into the slab part, with more leaks for smaller bending radii. This means large radii is required to minimize bending losses [34]. From research carried out by Westerveld Lab, a rib waveguide with a slab height of $100\,nm$, a rib height of $220\,nm$ and a rib width of $450\,nm$ has a propagation loss of $1\,dB/cm$ for a bending radius of $10\,\mu m$ (W.J. Westerveld, personal communication, December 5, 2022). A trend of further exponential increase in propagation losses below a bending radius of $10\,\mu m$ was shown.

3.2.3 Sub-Wavelength Waveguides

In this report, the term sub-wavelength waveguides refers to both slot waveguides and sub-wavelength gratings, since both waveguides have gap sizes that are smaller than the propagating wavelengths. Slot waveguides consists of two small strip waveguides placed closely together with a small gap in between. This gap is much smaller than the decay length of the evanescent field, allowing light to propagate between these two strip waveguides. On tho other hand, sub-wavelength gratings are strip waveguides that contain small periodic gaps along the length direction. The gap length is smaller than the wavelength, causing light to keep propagating along the sub-wavelength grating. What both waveguides have in common is that high intensities are present in these gaps, which are reachable for analytes. This allows for increased in sensitivity compared to strip waveguides [35][36][37]. However due to the small dimensions, it is very challenging to fill these gap with non-fluids, such as the polymer cladding for force sensing as explained in section 1.2.

3.2.4 Photonic Crystals Waveguides

Photonic crystal (PhC) are nanostructures that contains periodically changes in refractive indices, creating a region where light is unable to propagate through. This is also known as (photonic) bandgap. PhC's can be divided 1D-, 2D- and 3D-PhC's [38]. One-dimensional photonic crystals are also known as Bragg gratings [39], which contain periodically placed low refractive index gaps along the sidewalls of the waveguide. This type of waveguide can be used to create integrated photonic sensors, which will be discussed in subsection 3.3.4. Two-dimensional photonic crystal structures consists of an array of holes (cavities) in the material platform, which reprents the photonic bandgap. Light can only propagate at places where no cavities are presents. Missing cavities or changes of cavity radii in the photonic bandgap are called defects (i.e. the disruption of periodic refractive index changes). Three-dimensional photonic crystals will not be discussed, since photonic integrated circuits are most of the time two-dimensional. However, photonic crystals (notably 2-dimensional variants) are sensitive to fabrication errors [40]. This can be a problem for an array of resonator sensors, where multiple resonance peaks can overlap as a result. However, the bandgap can strongly confine light [41].

3.2.5 Comparison of Waveguide Geometries

The comparison of the rib, slot and photonic crystal waveguide to the strip waveguide is shown in Table 3.2.

Waveguide geometry compared to strip	Pro(s)	Con(s)
Rib	Less affected by side-wall roughness	Small bending radii show high radiation
	scattering	losses into the slab
Subwavelength	High sensitivities	Not applicable to polymer cladding
Photonic crystals	Strong light confinement	Prone to fabrication errors

Table 3.2: Comparison of material platforms

Due to the slab layer which decreases the sidewall area, rib waveguides show lower scattering losses compared to strip waveguides. However, the slab layers also result in higher radiation loss in the bends compared to strip waveguides. This makes it impossible to design integrated photonic devices with rib waveguides that is small enough to satisfy the sensor size requirement defined in section 1.3. This makes rib waveguides an unideal design choice compared to strip waveuigdes.

Slot waveguides and subwavelength gratings are not suitable for this project either, due to the challenge of putting polymer material between the very small gaps. Despite having higher sensitivities compared to strip waveguides due to more light interaction with the cladding in these gaps, the fabrication challenges makes these two waveguide types less appealing compared to strip waveguides.

Similar to slot waveguides and subwavelength gratings, the fabrication error sensitivity of photonic crystals has a higher chance of resulting in low yields (i.e. percentage of all fabricated chips on a wafer that work as

desired) compared to strip waveguides, which increases the fabrication costs per chip. As defined in section 1.3, low-cost photonic integrated circuit fabrication is required to treat the measurement platforms as consumables.

As a conclusion, photonic devices from strip waveguides can be very small and are not as sensitive to fabrication errors compared to photonic crystals, making it the most optimal choice for this project.

3.3 Integrated Photonic Sensing Devices

Biological cell forces can be sensed by detecting changes in light signals due to refractive index differences of the polymer cladding. This will also result in a different effective refractive index n_e . Various integrated photonic devices can be used to use this phenomenon to sense external effects such as biological cell forces. All integrated photonic devices described in this section make use of n_e change to detect changes in the light signal.

3.3.1 Ring Resonators

Ring resonators are ring-shaped photonic devices (see Figure 3.1a) which can be used to divert light intensities at resonance wavelenghts from an input waveguide that passes along the ring resonator. A normalized intensity spectrum that is coupled to this input waveguide will then experience intensity drops at certain wavelengths, which resemble inverted resonance peaks (see Figure 3.1b).

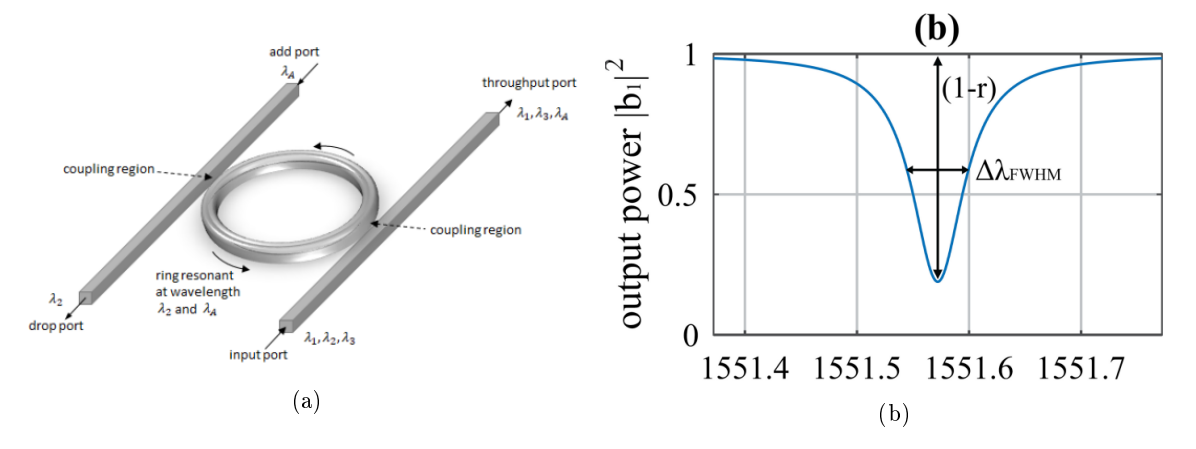


Figure 3.1: (a) Ring resonator [42]. (b) Resonance dip [14]

These certain wavelengths are called the resonance wavelengths (λ_m) , which can be determined from the resonance condition equation:

$$m\lambda_m = n_e(\lambda_m, \chi)L \tag{3.1}$$

where m is an integer number that describes the resonance number associated with the ring resonator. L is the total coupling length of the ring resonator and the term χ in n_e is a physical parameter (e.g. temperature or refractive index of the cladding). In this case, certain wavelengths fit m amount of times in the ring resonator, causing constructive interference and therefore can keep propagating in the ring resonator [43]. For a refractive index sensor, only n_e is affected by χ (not the coupling length L, since no mechanics are involved that can change the coupling length of the ring resonator). From Equation 3.1, it can be seen that a change in χ will also change n_e and therefore cause a resonance wavelength shift. Refractive index sensors work with this principle to detect any physical parameter.

When neglecting χ , the effective index $n_e(\lambda_m)$ is only expressed in terms of resonance wavelength λ_m . Equation 3.1 can then be rewritten to determine a specific resonance wavelength:

$$\lambda_m = \frac{n_g(\lambda_c)L}{m - \frac{n_e(\lambda_c) - n_g(\lambda_c)}{\lambda_c}L}$$
(3.2)

where $n_e(\lambda_m)$ is determined by rewriting Equation 2.11 with $\lambda = \lambda_m$ and subsequently substituted in Equation 3.1 to get Equation 3.2.

Going back to the physical parameter χ , an equation that represents a linear shift of the resonance wavelength caused by a change of χ (which will be referred as *sensitivity* from now on) can be derived from Equation 3.1 [14].

$$S \equiv \frac{\partial \lambda_m}{\partial \chi} = \frac{\lambda_c}{n_g} \frac{\partial n_e}{\partial \chi} \tag{3.3}$$

where $n_g = n_e(\lambda_c) - \lambda_c \partial n_e / \partial \lambda$. When $\chi = n_{clad}$, then $\partial \lambda_m / \partial n_{clad}$ represents the refractive index sensing sensitivity, that describes the wavelength shift per refractive index unit (RIU) of the cladding. With this, the limit-of-detection (LOD) can be calculated, which is a measure to determine a sensor's performance. In section 4.1, the LOD is explained in more detail. However when χ is temperature T, then $\partial \lambda_m / \partial T$ represents the temperature sensitivity or the temperature induced wavelength shift. This is caused by the thermo-optic coefficient property of a medium, which negatively affects sensors that is supposed to sense anything but the temperature. As an example, a small temperature drift can mimic refractive index changes of the cladding due to external forces (in the case of a force sensor that uses bulk refractive index sensing method), giving a false force detection. In section 3.4, different methods to combat this phenomena are discussed.

Light coupling and transmission processes are based on the coupled mode theory [14]. The principles of coupling and transmission in a racetrack-shaped ring resonator with and without a drop port (often referred as all-pass and add-drop configuration respectively [30]) are shown in Figure 3.2.

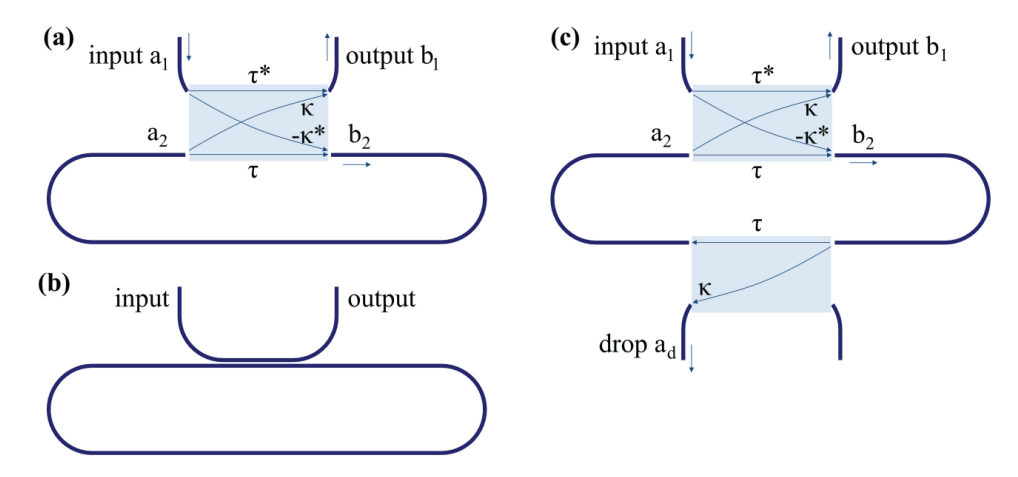


Figure 3.2: (a) An all-pass racetrack with couplings, transmissions and modal field amplitudes indicated. (b) Sketch of an all-pass racetrack resonator. (c) An add-drop racetrack resonator [14]

 a_1 , a_2 , b_1 and b_2 are the amplitudes of the travelling modes in the waveguides. Taking a square of these amplitudes gives intensities $|a_1|^2$, $|a_2|^2$, $|b_1|^2$, $|b_2|^2$. τ and κ are the transmission and coupling coefficients respectively, with $|\tau|^2 + |\kappa^2| = 1$ indicating a lossless coupler without any reflections. The drop port extracts light that is propagating in the ring resonator. This leaves a high extinction ratio's (a ratio between the highest and lowest point of a resonance peak) in output $|b_1|^2$, since less light is coupled back to the input waveguide. The intensity spectrum at output b_1 of an all-pass ring resonator can be analytically determined with the following equation [44].

$$|b_1|^2 = \frac{\alpha^2 + |\tau|^2 - 2\alpha |\tau| cos(\theta)}{1 + \alpha^2 |\tau|^2 - 2\alpha |\tau| cos(\theta)} |a_1|^2$$
(3.4)

where α is the light propagation loss (with $\alpha=1$ indicating no loss) and θ is the phase delay. If α is equal to τ (the roundtrip losses of a ring resonator equals the amount of optical coupled power), then critical coupling is achieved. This results in a very sharp resonance peak and a high measurement resolution as shown in subsection 4.2.4. When both waveguides of the coupler are identical in size, then θ can be determined with the following equation.

$$\theta = -\beta L \tag{3.5}$$

where L is the coupling length of the ring resonator and β is the propagation constant, which can be calculated with Equation 2.12. In the case of a ring resonator with a drop port, the intensity at output $|b_1|^2$ and the drop port $|a_d|^2$ can be determined with the following equations are applicable [44].

$$|b_1|^2 = \frac{(\alpha^2 + 1 - 2\alpha|\tau|\cos(\theta))|\tau|^2}{1 + \alpha^2|\tau|^4 - 2\alpha|\tau|^2\cos(\theta)}|a_1|^2$$
(3.6)

$$|a_d|^2 = \frac{(1 - |\tau|^2)\alpha}{1 + \alpha^2 |\tau|^4 - 2\alpha |\tau|^2 \cos(\theta)} |a_1|^2$$
(3.7)

The sensitivity of a SOI strip waveguide ring resonator is calculated to be around $40 - 80 \, nm/RIU$ using RectWG, depending on the waveguide dimensions and the cladding index. A $500x220 \, nm$ strip waveguide submerged in water (n=1.333) with a propagating TE mode gives a sensitivity of $45.3 \, nm/RIU$. This is somewhat close to the experimental result of Fard et al. of $38.2 \, nm/RIU$ [32]. However, De Vos et al. [45] have shown a similar ring resonator having a sensitivity of $70 \, nm/RIU$ and a LOD of $10^{-5} \, RIU$. But even higher performances are reachable, as Iqbal et al. [46] have shown identical ring resonators with a sensitivity of $163 \, nm/RIU$ and a LOD of $7.6 \cdot 10^{-7} \, RIU$ for TE mode. Therefore, it can be observed that the sensitivity can be different in practice compared to the theory.

The sensitivity can also be increased by choosing a TM propagation mode instead of TE. Due to TM mode's more leaky nature compared to TE modes, ring resonators with TM modes show higher sensitivies but experience higher radiation losses [47]. Another way to cause light to leak out of the waveguide more to increase the sensitivity is to lower the waveguide height [32], as explained in subsection 3.2.1. Furthermore, two rings can be cascaded (with the first ring being the reference and the second being the sensor) in order to obtain the Vernier effect, which can drastically increase the sensitivity [48]. However, the minimum detectable wavelength shift also increases, resulting in an identical LOD. The downside of Vernier effect is the larger required device footprint and the very small free spectral range (FSR, which is the distance between two resonance wavelengths from the same integrated photonic resonator), making interrogation of multiple sensors simultaneously difficult.

Xu et al. [49] have demonstrated ring resonators with long path lengths folded into a small area. The longer path lengths relaxes the resonance condition, making it easier to achieve critical coupling and high Q-factors (sharp resonance peaks). In other words, the decrease of Q-factor is less affected by coupling variations). On the contrary, longer path lengths also reduce the FSR. Decreasing it too much limits the amount of ring resonators that can be multiplexed. Many resonance peaks will quickly overlap each other, making it difficult to interrogate refractive index changes.

Finally, ring resonators can be very small to satisfy the requirement of 5 to $10 \,\mu m$ sensor separation as mentioned in section 1.3 [20]. Such small sensors show higher radiation losses due to low bending radii besides the scattering loss from side-wall roughness. This can explain why Q-factors of around 10^4 . Ring resonators with larger radii show Q-factors that are larger than 10^4 [32][46].

3.3.2 Mach-Zehnder Interferometers

In a Mach-Zehnder interferometer (MZI) on a photonic integrated circuit, a monochromatic light that propagates in a waveguide get split in two and recombined afterwards, causing interference. Due to an optical path difference, phase difference will be introduced. Based on the magnitude of the phase difference, light gets either constructively or destructively interfered, or somewhere in between. For a refractive index sensor based on a MZI, both the path length difference and the difference in the propagation constant result in a phase difference [43]. The reason for this is that a sensing arm is cladded with the analyte, while the reference arm is shielded from it. This results in a different effective (group) refractive indices $(\Delta n_e(\lambda_c))$ and $\Delta n_g(\lambda)c$) and therefore also a difference in the propagation constant $(\Delta\beta)$.

$$\phi = \Delta \beta \Delta L$$

$$= (\beta_{sense} - \beta_{ref}) \Delta L$$

$$= \frac{2\pi}{\lambda} \Delta n_e(\lambda) \Delta L$$
(3.8)

where $\Delta L = L_{sense} - L_{ref}$, k and λ is the wavenumber and wavelength of the monochromatic light input respectively. It can be seen from Equation 3.8 that the *phase sensitivity* $\partial \phi / \partial n_e$ scales with ΔL . This makes very high sensitivities possible if the path length difference is large, but it also increases the footprint.

In a MZI, light can get split by a Y-splitter, a multi-mode interference coupler or a directional coupler [14] (which uses coupled mode theory, similar to ring resonators). In this report, the analytical calculations of a MZI with directional couplers are discussed with parameters as shown in Figure 3.3. Similar to the coupled mode theory used for ring resonators, variables a_i , b_i , c_i and d_i where i = 1, 2 are amplitudes of the propagating light at different points of the MZI. a_i and d_i being the input and output amplitudes respectively. Knowing only the input amplitudes $a_1 \neq 0$ and $a_2 = 0$, transmission τ and coupling coefficient κ , propagation losses of both arms α_1 and α_2 as well as the phase difference $\phi_1 - \phi_2$, the output intensities $|d_i|^2$ can be calculated with the following equations.

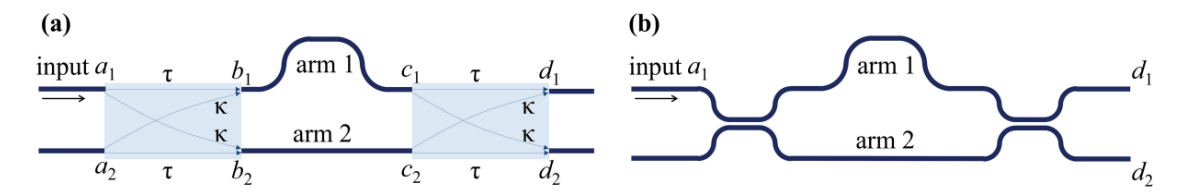


Figure 3.3: Mach-Zehnder interferometer sketch (a) Sketch with couplings, transmissions and modal field amplitudes included (b) Sketch with directional couplers [14]

$$|d_1|^2 = (|\tau|^4 \alpha_1^2 + |\kappa|^4 \alpha_2^2 - 2|\tau|^2 |\kappa|^2 \alpha_1 \alpha_2 \cos(\phi_1 - \phi_2)) |a_1|^2$$
(3.9)

$$|d_2|^2 = |\tau|^2 |\kappa|^2 \left(\alpha_1^2 + \alpha_2^2 + 2\alpha_1 \alpha_2 \cos(\phi_1 - \phi_2)\right) |a_1|^2$$
(3.10)

Plotting the output intensities at different optical path lengths differences (i.e. over different effective indices or path length differences), a sinusoidal wave can be seen, indicating constructive and destructive interferences at certain optical path length difference. This means that the interrogation method of a MZI refractive index sensor is to determine the change intensity caused by the difference in refractive index of the cladding in the sensing arm with a single-frequency light input.

Different MZI refractive index sensors are shown to have phase sensitivities from around $600 \, rad/RIU$ to all the way to $4710 \, rad/RIU$, depending on the sensing arm length and the modes, with TM being more sensitive than TE [50][51][52]. This results in detection limits of $10^{-5} \, RIU$ to $10^{-7} \, RIU$ for sensing arm lengths from $600 \, \mu m$ to $10 \, mm$. It has been shown in subsection 3.3.1 that these performances can also be reached by ring resonators for a fraction of MZI's footprint. The footprint of a MZI can be made somewhat compact by folding the path lengths [51][53], but ring resonators will always be superior in this regard. MZI's can be cascaded with a ring resonator to obtain a Vernier effect as well [53]. This increases the sensitivity but requires larger footprint and a large part of light spectrum gets occupied by resonance peaks of a single Vernier sensing element, similar to the ring resonator's case. Finally, it is shown that MZI's can show low fabrication error sensitivity [54].

3.3.3 Disk Resonator

Disk resonators are circular shaped with light travelling along a path length that is equal to the perimeter of the disk. Equations (the ones discussed in subsection 3.3.1) are used to determine the characteristics of a disk resonator [55]. Unlike ring resonators, disk resonators only have a single side-wall. This means there is less side-wall interaction with light, reducing scattering losses. As a result, the disk resonators can show high Q-factor resonance curves $(Q = 33000 \text{ to } 10^6)$ [56][57] or be very small in size $(R \le 3 \mu m)$ [56][58][59]. If the disk radius is small, the optical path length will also be small, resulting in high FSR. All these characteristics make multiplexing disk resonators possible [56][60] [61]. It should be noted that very small disk resonator is only suitable for TE modes, since the bending losses for TM will be very high [56]. The sensitivities of disk resonators vary from different research. In general, higher sensitivies are caused by TM modes, utilizing smaller disk radii or to use suspended disks to allow additional analyte interaction below the resonator [59]. It is also shown that the sensitivities can be quite low (around $30 \, nm/RIU$) [56][62]. A probable reason for this is the strong light confinement resulted from the combination of TE mode and the single side-wall of a disk resonator. The limits-of-detection for a disk resonators is around $10^{-3} RIU$ to $10^{-5} RIU$ [56]. Another downside to disk resonators is the possibility of multi-mode propagation [58][59]. Single-mode propagation is desired, especially for sensor arrays, to prevent excess amount of resonances in the spectrum. It has been shown that higher-order modes have higher losses, therefore suppressing these resonance peaks to a certain extend [59]. A compromise is to use a hybrid ring-disk resonator, which is a ring resonator that uses a high-width strip waveguide. The amount of propagating modes can be minimized while exploiting the lower side-wall scattering found in disk resonators [63].

3.3.4 Phase-Shifted Bragg Gratings

As for Phase-shifted Bragg gratings, based on the phase of these periodic refractive index changes (which depends on both the length and refractive indices), specific wavelengths of a light spectrum can be reflected back and therefore create a resonance peak or dip. A notable advantage of Bragg gratings over ring resonator is the lack of bends, which decreases propagation losses [61]. The footprint is very small in the width direction

as well. However, smaller grating lengths lead to lower Q-factor (Bragg gratings become a broadband filter instead)[64][65], which results in lower minimum detectable wavelength shift, as explained in section 3.5. Having a longer grating length means the sensing element is not compact in the length direction, which is undesirable for distributed sensing. On the other, longer grating lengths are also more susceptible to fabrication errors [66]. A Bragg grating biosensor has been shown that has a sensitivity of $90 \, nm/RIU$, a $Q \approx 10^4$ and a limit-of-detection of approximately $5 \cdot 10^{-5} \, RIU$ [64], which is roughly in the same order of magnitude for smaller ring resonators.

3.3.5 Photonic Crystal (Cavity) Resonators

There are two different types of 2D photonic crystal defect types: a line defect and a point defect [41]. With line defects, entire rows of cavities are removed or its radii have changed. This allows light to propagate similar to a waveguide. Light is confined in-plane by photonic bandgaps and cofined out-of-plane by internal reflection. When cavity holes are removed, the line defect becomes a regular waveguide. However, refractive index sensors can be created with points defects acting as an optical resonator [67]. Point defects are local removal, size changes or shift of cavities. At these point defects, light will reflect back and forth. This means only resonant wavelengths (at which light will constructively interfere with each other) can keep propagating in the point defect wavelengths [68] while light with the remaining wavelengths can propagate through the defect to the photoreceiver. As a result, resonance dips as shown in Figure 3.1b will be measured. These resonance wavelengths can shift if for example the cladding refractive index changes (that causes the optical path length in the defect to change). This method can be combined with PhC line defect waveguide to create multiple compact add/drop filters along a waveguide [67][69]. It has been shown that these types of refractive index sensors with 2D photonic crystals can obtain good sensing performance (sensitivity $\geq 200 \, nm/RIU$ and/or Q > 50000 possible) [41][69][70]. However, photonic crystal resonators have very short cavity lengths (e.g. $L = 95 \, nm$ [71]), meaning that the smallest fabrication error can result in a large percentage cavity length change and therefore a large shift in resonance wavelength (W.J. Westerveld, personal communication, Januari 23, 2023). This problem is more apparent when considering an entire array of sensors. Ring resonators have larger cavity lengths (e.g. for $R=1.5\,\mu m,\ L=9425\,n m$), which reduces the sensitivity to dimension nonuniformities compared to photonic crystal cavity resonators.

3.3.6 Comparison of Integrated Photonic Sensing Devices

The properties of different integrated photonic sensing devices are shown in Table 3.3.

Device	Sensitivity	Q-factor	Footprint	Robustness to Fabrication Errors
Ring	40160*	$>=1\cdot 10^4$	$R >= 1.5 \mu m$	Robust
Disk	30*	$3\cdot 10^4\dots 1\cdot 10^6$	$R >= 1.5 \mu m$	Robust
MZI	600 4710**	N/A	$L_{sense} = 600 \mu m \dots$ $10 mm$	Robust
Phase-Shifted Bragg Gratings	90*	$1 \cdot 10^4$	$L > 10 \mu m$	Sensitive
PhC Cavity	>= 200*	> 50000	L = 95 nm	Sensitive

Table 3.3: Qualtitative comparison of sensing devices. *Unit in nm/RIU. **Unit in rad/RIU.

From the table, it can be seen that the MZI, phase-shifted Bragg gratings and photonic crystal cavity resonators are either too large or are prone to fabrication errors, making these options unideal for this project. This leaves the ring and disk resonator as the only viable options, since these sensing device types can be small and are more robust to fabrication variations due to having a longer cavity length compared to other devices. Disk resonators show additional robustness to fabrication errors, since having a single side-wall reduces the scattering losses due to side-wall roughness. The Q-factors of disk resonators are in general higher compared to the ones of the ring resonators. This allows more disk resonators to be multiplexed on a single bus waveguide without the resonance peaks overlapping one another (resonance peak overlap is explained in more detail in subsection 6.2.2). However, ring resonators show higher sensitivities compared to disk resonators. The ring resonator design presented in section 7.2 strikes a balance between the higher sensitivity of the ring resonator and the sharpness of a resonance peak (i.e. high Q-factor) found in disk resonators.

3.4 Methods for Temperature Drift Compensation

Changes in refractive index of the cladding due to external forces is not the only way to induce resonance peak shift, temperature drifts can do it as well (as explained in subsection 3.3.1). This is caused by the thermo-optic coefficient (TOC) of a material, which is a gradient that describes the change of refractive index due to temperature changes. Also due to the nature of thermodynamic entropy and the small footprint of a photonic integrated circuit, the temperature is considered to be uniform all over the distributed sensors. Using Rect WG, a temperature sensitivity of around $53 \, pm/K$ for a silicon photonic ring resonator with PDMS cladding $(TOC_{PDMS} = -4.5 \cdot 10^{-4} \, RIU/K \, [72])$ has been calculated. This means a temperature drift of as small as $0.1 \, K$ can shift the resonance peak by $5.3 \, pm$. In chapter 4, it has been shown that this has a huge effect on the sensor performance. For this reason, different methods are discussed in this section to combat the effects of temperature drifts.

3.4.1 Temperature Reference

Integrated photonic temperature sensors can be employed to determine wavelength shift caused only by temperature drifts, which can be used as a reference for the force sensors [73]. This is done by shielding the temperature sensor from other external effects (in our case, it is the force from the cells). SiO_2 or SU8 are options to cover these reference sensors. Resonance peak shift determined from the reference sensor can be subtracted from the resonance peak shift of the force sensor (which can contain contributions of both force and temperature changes). The remaining observed resonance peak shift of the force sensor after the subtraction is then considered to be only caused by changes of external factors other than the temperature. It should be noted that both the reference and force sensors need to be interrogated at the same time in order to obtain the same temperature induced resonance peak shift.

This is one method to decrease the temperature dependence of the sensor. Current research has not taken into account the wavelength repeatability of a tunable laser (which also causes wavelength variations in the resonance peak after each sweep). This means the resonance peak shift of both the reference and force sensor is also contributed by the wavelength repeatability. This tunable laser property cannot be cancelled out with reference sensor unless the temperature sensitivities of both the reference and force sensors are the same. Having different cladding materials, the width of either sensor type can be tuned to equalize the temperature sensitivities.

3.4.2 Different Waveguide Widths

Research has shown that MZI's with different (tuned) widths in each arm can be used to cancel out the temperature sensitivity [74][75][76]. The different widths of each arm result in different temperature sensitivities and can also be used to make the device fabrication error intolerant [77]. With a MZI configuration, these temperature sensitivities can be subtracted with each other, effectively cancelling out the overal temperature dependence. However, using MZI as a sensor is not suitable for designing a densly integrated array of force sensors due to its large footprint. Another research shows a MZI can be cascaded to a drop port of a ring refractive index sensor [78]. This way, ring resonators can be used to create a dense array of sensors, while still utilizing MZI's athermal effects. However, this method utilizes instead of wavelengths to interrogate. section 3.5 shows that intensity fluctuations present caused by the laser source and the read-out instruments, which decreases the signal-to-noise ratio.

3.4.3 Negative Thermo-Optic Materials

The large resonance peak shift due to temperature drift is mainly caused by the large TOC of silicon ($TOC_{Si} = 1.8 \cdot 10^{-4} \, RIU/K^{-1}$) [79] and the high intensities in the waveguide core. Negative TOC materials (mainly polymers) can be used to decrease the overall (effective) temperature sensitivity. This is done by allowing part of the total light intensity to propagate through negative TOC materials (via evanescent fields). Since the intensities of the evanescent fields are small in comparison to the intensity in the waveguide core, the contribution of negative TOC materials will also be small. This makes it difficult to completely cancel out the overall temperature sensitivity. In this project, it has already been decided to add a polymer cladding on top of the integrated photonic sensor for cell force sensing. Since polymers generally have negative TOC, the partial temperature cancellation is already considered. As an example, when the TOC of the cladding is neglected, then the temperature sensitivity becomes $78 \, pm/K$ [14], which is higher than taking PDMS cladding into account (see the introduction of this section).

3.4.4 Dual Mode Sensing

It is possible for a waveguide to have multi-mode propagation (e.g. TE0 and TM0). Each mode has its own resonance peak in the spectrum and sensitivity of both temperature and force. In this way, a sensitivity matrix can be created, which can be used with the resonance peak shifts of both modes to seperately determine the temperature drift and RI change due to external factors (e.g. force) [47][62][80]. Compared to temperature reference method, this method has a smaller footprint due to the lack of extra reference sensors. However, TM modes are less confined, resulting in large radiation losses (but higher sensitivities) for small bending radii. Furthermore, the wavelength repeatability issue is present here as well.

3.4.5 Active Temperature Control

The temperature of a photonic integrated circuit can be stabilized using an active temperature controller. This can be done in two ways: a PID temperature controller for ambient temperature control or integrated microheater or thermoelectric cooler onto the chip. The first option is always helpful, since the lab temperature can change during the day. However, on-chip temperature compensation methods are still desirable to assure local chip temperature stabilization, hence the existence of integrated microheaters [81]. These devices can be put on top or next to the resonators with isolation in between to prevent propagation losses [30]. The device performances are the tuning efficiency (related to the amount of power input) and the tuning speed [82]. For distributed sensors, either each sensor gets a microheater placed on top which makes the chip layout very complicated, or only a few microheaters are spread over the sensor array. The latter option is less efficient, since heat gets diffused further away from the microheater. Placing heaters above of resonators mean the top evanescent field does not propagate through any cladding of which the refractive index can change due to external factors like biological cell forces, making the sensor less sensitive. For these reasons, integrated microheaters are not considered for this project from now on.

3.4.6 Comparison of Temperature Drift Compensation Methods

The properties of all the temperature compensation methods are shown in Table 3.4.

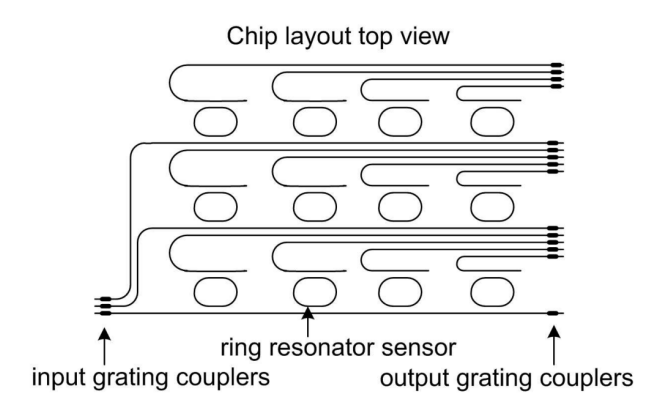
Temp. compensation method	Pro(s)	$\operatorname{Con}(\operatorname{s})$
Temperature reference	Can potentially cancel out wavelength repeatability	Requires interrogating two resonance peaks
MZI with diff. widths	Low temperature sensitivity, passive	Large footprint
Materials with negative thermo-optic coefficient	Passive	Decrease sensitivity, CMOS incompatible
Dual mode sensing	Local ring resonator temperature compensation	Twice the amount of resonance peaks, requires interrogating two resonance peaks
Active temp. control	Temperature stabilization	Requires extra fabrication steps

Table 3.4: Comparison of material platforms. Note: none of the methods takes into account the wavelength repeatability.

Although every method can compensate temperature to a certain degree, only the temperature reference sensor can potentially cancel out wavelength repeatability as well when the temperature sensitivity of the reference sensor is the same as the one from the force sensor. This means even if another temperature compensation method is chosen to combat the temperature drift, a reference ring resonator is still required to eliminate the wavelength repeatability, making these temperature compensation methods redundant. Therefore, the temperature reference sensor is the most ideal option.

3.5 Array Configurations of Integrated Photonic Sensing Elements

Different array of integrated photonic sensors designs have been shown [1][46][83][84]. One method to multiplex ring resonators is to put these ring resonators on the same bus waveguide, as shown in Figure 3.4. Poon et al. [85] have shown different ring resonator array configurations for creating on-ship switch interconnections, which can also be used for refractive index sensing. A promising ring resonator array configuration is



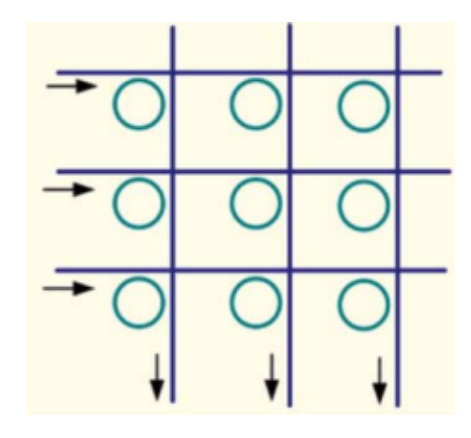


Figure 3.4: Rings on a bus [1]

Figure 3.5: Grid array of ring resonators [85]

the grid-type, which consists of add and drop ports placed perpendicularly to each other (see Figure 3.5). This is the most compact way to add drop ports to an array of integrated photonic sensors, allowing the spacing between the ring resonators in both the horizontal as well as the vertical direction to be the same, unlike parallel add and drop ports [1]. Due to a lack of completed research specifically focusing on integrating multiple small photonic sensors closely together, it has been decided to go more in depth to array design after the literature review.

Chapter 4

Interrogation Performance of Integrated Photonic Resonators

From chapter 3, it has been concluded that resonator-based sensors can be small enough to satisfy the array density requirement mentioned in section 1.3, with ring resonator shown to be the most robust to fabrication errors. In this chapter, the performance of resonator-based sensors will be determined in presence of different noise sources and improved by decreasing these noises.

4.1 Measurement Resolution and Limit-of-Detection

Besides the refractive index sensing sensitivity as discussed in subsection 3.3.1, the minimum detectable wavelength shift (i.e. the measurement resolution) $\Delta \lambda_{min}$ is also a performance parameter of an resonator-based sensor. It represents the possible variation of resonance wavelengths between tunable laser sweeps, even if no force is exerted on the sensor. $\Delta \lambda_{min}$ depends mainly on the noise from the measurement setup, such as the temperature drift (as explained in subsection 3.3.1), wavelength repeatability of a tunable laser and the intensity noise, which is shown in Figure 4.1.

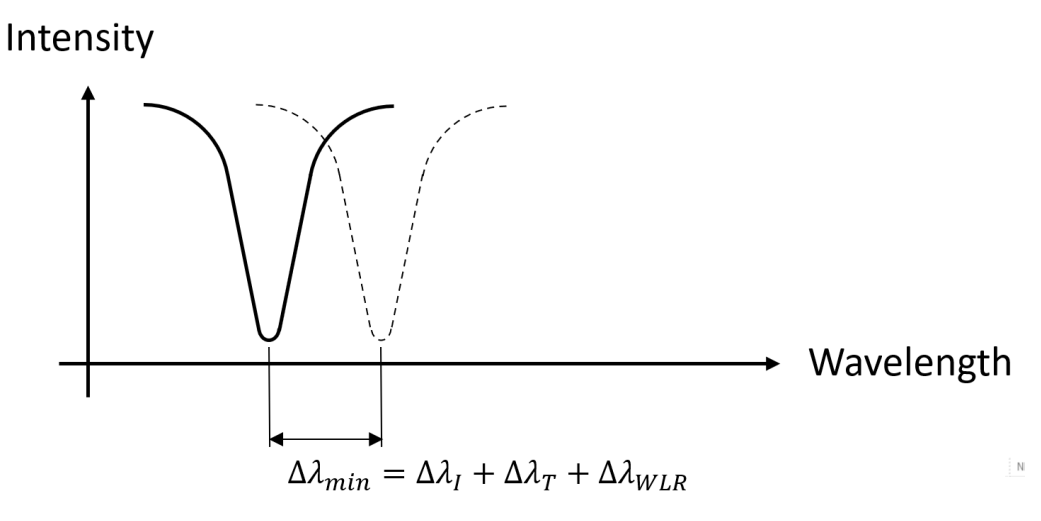


Figure 4.1: Schematic illustration of the measurement resolution. $\Delta \lambda_I$, $\Delta \lambda_T$ and $\Delta \lambda_{WLR}$ is the resonance wavelength shift due to intensity noise, temperature drift and wavelength repeatability respectively

Taking both the refractive index sensing sensitivity and $\Delta \lambda_{min}$ into account, the limit-of-detection (LOD) can be determined with the following equation [86].

$$LOD = \frac{\Delta \lambda_{min}}{S} \tag{4.1}$$

The limit-of-detection describes the minimum detectable refractive index unit change (smaller LOD indicates higher performance). Another method to indicate the refractive index sensor performance without considering

the noise (i.e. only taking into account the properties of the ring resonator) is to determine the intrinsic limit-of-detection (iLOD).

$$iLOD = \frac{\Delta \lambda_{FWHM}}{S} = \frac{\lambda_m}{Q \cdot S} \tag{4.2}$$

where $\Delta \lambda_{FWHM}$ is the full-width half maximum (FWHM) of the resonance peak, which can be calculated using the following equation.

$$\Delta \lambda_{FWHM} = \frac{\lambda_m^2}{\pi L n_g(\lambda_m)} cos^{-1} \left[\frac{2\alpha \tau}{1 + \alpha^2 \tau^2} \right]$$
 (4.3)

It can also be seen that a higher Q-factor (Q) results in a lower iLOD. The equation for the Q-factor can be derived from Equation 4.2, resultin in Equation 4.4.

$$Q = \frac{\lambda_m}{\Delta \lambda_{FWHM}} \tag{4.4}$$

In general, iLOD is less accurate than LOD. The reason for this is that $\Delta \lambda_{min}$ is much smaller than $\Delta \lambda_{FWHM}$, which will be shown in section 4.2.

4.2 Performance Determination in Presence of Intensity Noise

As mentioned in section 4.1, the measurement resolution is dependent on the measurement setup noise. Both the light source and the photodetector show intensity fluctuations at very small time scales, meaning the intensity of all the measurement points on the transmission spectrum (Equation 3.4) vary independently. In this subsection, the effect of the independent intensity variation at each measurement point on $\Delta \lambda_{min}$ and subsequently the LOD is analyzed. The influence of the intensity noise on the measurement resolution will be compared to the influence of the temperature drift and the wavelength repeatability in subsection 4.2.5.

4.2.1 Considered Setup and Noise Modeling

A schematic interrogation setup has already been shown in Figure 2.4. For this analysis, a general case of a photonic integrated circuit with a silicon strip waveguide ring resonator with a radius of $10 \,\mu m$, propagation loss $2 \, dB/cm$, waveguide dimensions of $450x220 \, nm$, fundamental TE mode, a central resonance wavelength of $1550 \, nm$ and air cladding is taken. With the propagation loss and the ring radius, the power loss after one roundtrip in the ring can be calculated with the Equation 4.5, resulting in $\alpha^2 \approx 0.997$.

$$\alpha^2 = 10^{-(2dB/cm) \cdot 2\pi R/10} \tag{4.5}$$

Besides the photonic integrated circuit, a Santec TSL-570 (Type A) [87] tunable laser and 1811-FC InGaAs Fiber-Optic Receiver [88] (which has a saturation power of $55\,\mu W$) have also been chosen as a part of the considered setup. A schematic interrogation setup is shown in Figure 2.4. As mentioned above, these two instruments causes noise in the measurement signal. For the laser, the relative intensity noise (RIN) is the dominant intensity noise source. As for the fiber-optic receiver, the intensity noise is primarily caused by the noise equivalent power (NEP). The intensity fluctuation caused by the laser can be determined with the following equation:

$$\left(\frac{\delta P_{RIN}}{\overline{P}}\right)^2 = RIN \cdot BW_{PD} \tag{4.6}$$

where δP is the power fluctuation, \overline{P} is the average power and BW_{PD} is the photoreceiver bandwidth. The RIN of Santec TSL-570 (Type A) is equal to $-145\,dB/Hz$ for a photoreceiver bandwidth from $1\,MHz$ to $3\,GHz$ [87]. The bandwidth of 1811-FC is $BW_{PD}=125\,MHz$ [88], which is in range. \overline{P} is in this case the saturation power of the fiber-optic receiver $(55\,\mu W)$. Substituting these values in Equation 4.6 result in a power fluctuation caused by the relative intensity noise of $\delta P_{RIN}=34.58\,nW$.

The noise equivalent power (NEP) describes the noise experienced by the fiber-optic receiver. The power fluctuation caused by this noise can be calculated with the following equation:

$$\delta P_{NEP} = NEP \cdot \sqrt{BW_{PD}} \tag{4.7}$$

where the NEP of 1811-FC is $2.5 \, pW/\sqrt{Hz}$ and $BW_{PD} = 125 \, MHz$. Substituting these values in Equation 4.7 results in $\delta P_{NEP} = 28 \, nW$. The total power fluctuation caused by these two noises can be determined with the following equation:

$$\delta P_{max} \equiv 3\delta P_{stdev} = 3\sqrt{\delta P_{RIN}^2 + \delta P_{NEP}^2} \tag{4.8}$$

It can be seen that δP_{max} in Equation 4.8 is modeled using normal distribution and represents three standard deviation of the mean (3 σ). The standard intensity deviation is $\delta P_{stdev} = 44.49 \, nW$, which has been calculated with the two aforementioned intensity noise values.

To randomize the intensity noise in Matlab, the command $normrnd(0, \delta P_{max}/3)$ will be used. The value generated with this command will subsequently be added to a measurement point. The zero represents the mean and $\delta P_{max}/3$ is the standard deviation. This process is done seperately for all the measurement points in the entire transmission spectrum (Equation 3.4) that is going to be analyzed in order to obtain different intensity noise for each measurement point. Figure 4.2 shows how a transmission spectrum can change when intensity noise is added to it.

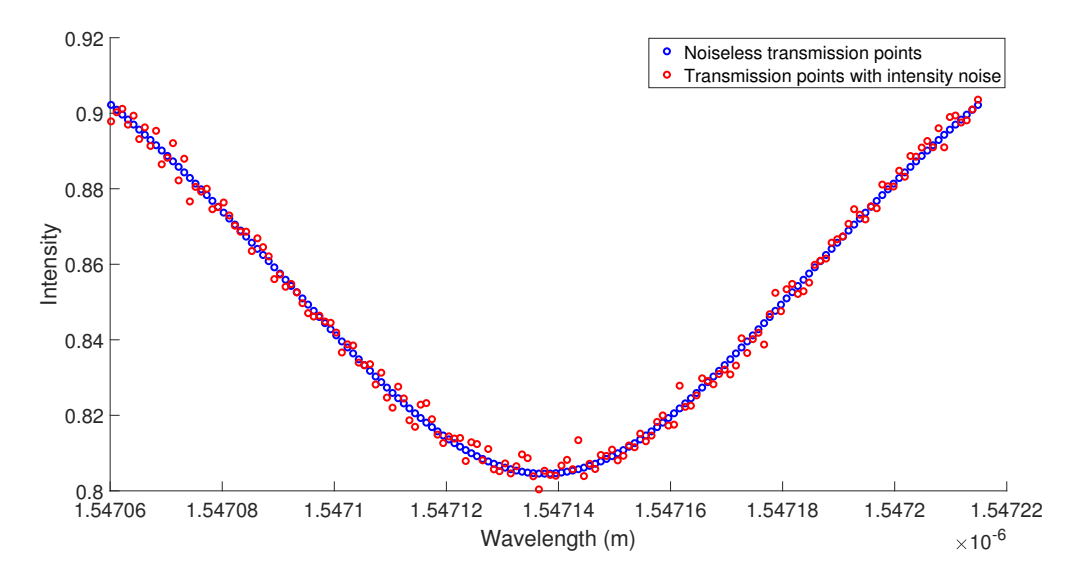


Figure 4.2: Transmission points with and without intensity noise example. Each measurement point has a seperate intensity noise value determined using Equation 4.8

Besides RIN and NEP, (out-of-plane) coupling variations can also fluctuate intensities. However due to the very fast sweep speed of TSL-570 (up to $200 \, nm/s$) [87], the entire transmission spectrum will be entirely swept before the (out-of-plane) coupling variations start to become noticable. Also, optical fibers can be glued on the grating couplers, making the (out-of-plane) coupling process even more robust to scattering variations.

4.2.2 Measurement Resolution Determination using Curve-Fitting Methodology

A common way to determine the measurement resolution $\Delta \lambda_{min}$ is by curve-fitting both noisy and noiseless resonance data points with a Lorentzian distribution curve and get a statistical average resonance wavelength difference between these two curve-fits over multiple (Monte-Carlo) simulations [1][48] (note that subsection 6.2.2 shows Monte-Carlo simulations as well, but these are intended for analyzing resonance peak overlaps instead). The shape of the Lorentzian distribution is identical to the resonance peak plotted with Equation 3.4 and is also suitable for curve-fitting (due to easily optimizable variables, which are shown in this section). The intensity noise applied to the transmission points as shown in Figure 4.2 can cause the resonance peak wavelength to deviate as illustrated in Figure 4.3.

In this section, the curve-fitting steps of Hu et al. are followed [89]. It starts by plotting the FWHM of a resonance peak from a transmission determined using Equation 3.4. The values of n_e , n_g and $\partial n_e/\partial \lambda$ that are required for Equation 3.4 can be determined using RectWG. Different intensity noises calculated with Equation 4.8 can be added to each data point of this FWHM transmission, which mimics a measurement with noise as shown in Figure 4.2.

An inverse Lorentzian distribution can then be curve-fitted in this transmission (with and without intensity noise) consisting of discrete measurement points using the following equation.

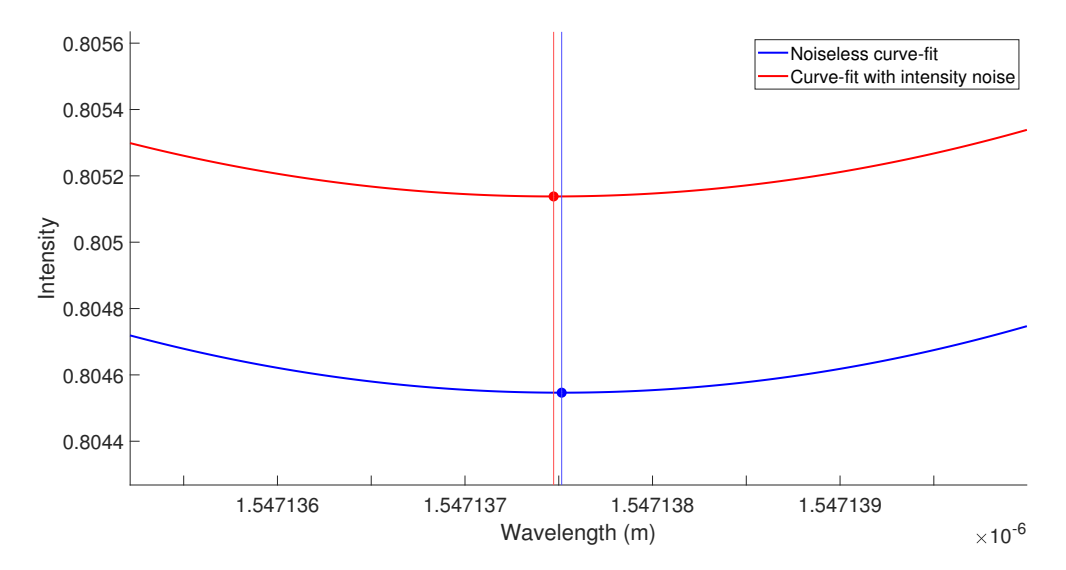


Figure 4.3: Two Lorentzian curve-fits of transmission points from Figure 4.2 at the resonance peaks. Due to the presence of intensity noise, the resonance peak can deviate from the resonance peak of the noiseless transmission curve-fit

$$P_{Lorentz}(\lambda) = P_{max} - \frac{A}{1 + \left(\frac{\lambda - \lambda_{peak}}{0.5 \cdot \Delta \lambda_{FWHM}}\right)^2}$$
(4.9)

where P_{max} , A, λ_{peak} and $\Delta\lambda_{FWHM}$ are the input power (This can be either the absolute input power such as the photoreceiver saturation power $55\,\mu W$ or a normalized power), the dip height of the resonance peak, the resonance wavelength and the full width half maximum of the resonance peak respectively. The dip height of the resonance peak with a normalized intensity transmission spectrum can be determined using the following equations [30], wit R_{min} representing the lowest point in the transmission spectrum.

$$A = 1 - R_{min} \tag{4.10}$$

$$R_{min} = \frac{(\tau - \alpha)^2}{(1 - \tau \alpha)^2} \tag{4.11}$$

Both the noiseless and the noisy transmission data points can be curve-fitted by optimizing these four variables using the Nelder-Mead simplex method (i.e. Matlab's *fminsearch* function) by minimizing the least-squares:

$$SSE = \sum_{i=1}^{n} (P_{data,i} - P_{Lorentz}(\lambda_i))^2$$
(4.12)

where i is the current data point, n is the total amount of data points, $P_{data,i}$ is the power value of the data point and $P_{Lorentz}(\lambda_i)$ is the power value of the Lorentzian distribution at a wavelength of the current data point. As for Matlab's fminsearch settings, the maximum function evaluations (MaxFunEvals) and the termination tolerances (TolFun and TolX) should be sufficiently large and small enough respectively (see Matlab's optimset function) in order to get the most accurate curve-fits. For this test, the maximum function evaluations is set to 10^5 and both termination tolerances to 10^{-12} .

Due to the random power fluctuations of the noisy transmission, the curve-fit and therefore also the resonance wavelength deviation will change for each calculation. For this reason, Monte-Carlo simulations must be carried out to provide a statistical average resonance peak deviation due to intensity noise. A thousand Monte-Carlo simulations for Lorentzian curve-fitting will be carried out, as it has been done before [1][89]. However, Figure 7.33 shows that more simulations are required to get a more accurate result. The minimum detectable wavelength shift can then be determined by first calculating the difference between the optimal λ_{peak} values of the noiseless and each of the noisy transmission curve-fit, and then taking the root-mean-square of all the λ_{peak} difference (see Equation 4.13).

$$\Delta \lambda_{min} = \sqrt{\frac{1}{N} \sum_{i=1}^{N} (\lambda_{peak,noiseless} - \lambda_{peak,i})^2}$$
(4.13)

where N is the amount of simulations carried out and $\lambda_{peak,noiseless}$ is the resonance wavelength of the noiseless transmission curve-fit.

4.2.3 Test Methodology

Different curve-fitting tests have been conducted with varying wavelength steps $(1.6\ fm,\,0.01\ pm,\,0.1\ pm,\,1\ pm,\,10\ pm)$ of the data points, different photoreceiver bandwidths $(100\ kHz,\,1\ MHz,\,10\ MHz,\,125\ MHz,\,1\ GHz)$ and different transmission coefficients τ that result in Q-factors of $(10^3,\,5\cdot10^3,\,10^4,\,5\cdot10^4,\,10^5,\,10^6,\,1.94\cdot10^6,\,3\cdot10^6,\,3.855\cdot10^6)$ with $Q=1.94\cdot10^6$ resulting in critical coupling with $\alpha^2\approx0.997$ and $R=10\ \mu m$. The Q-factors are increased by increasing the transmission coefficient τ while keeping α constant. The wavelength step of $1.6\ fm$ is taken from the linewidth of Santec TSL-570 type A of $200\ kHz$ [87] and the photoreceiver bandiwdth of $125\ MHz$ is the specification of 1811-FC InGaAs Fiber-Optic Receiver [88].

For varying wavelength steps test, a photoreceiver bandwidth of $125 \, MHz$ and a Q-factor of roughly 10^4 is taken. For varying photoreceiver bandwidths test, a wavelength step of $0.1 \, pm$ and a Q-factor of around 10^4 is chosen. Finally for varying Q-factors test, a wavelength step of $0.1 \, pm$ and a photoreceiver bandwidth of $125 \, MHz$ is utilized.

In this analysis, the photoreceiver bandwidths is varied solely to change the intensity noise values using Equation 4.6 to Equation 4.8 and observe the effects of the intensity noise on $\Delta\lambda_{min}$. Also, the different Q-factors are caused by varying the transmission coefficient τ . This also causes the extinction ratio (ER) to change, which is the ratio between the highest and the lowest point of a resonance peak. This can be calculated with the following equations [30], with T_t representing the highest intensity point on the transmission spectrum.

$$ER = \frac{T_t}{R_{min}} \tag{4.14}$$

$$T_t = \frac{(\tau + \alpha)^2}{(1 + \tau \alpha)^2} \tag{4.15}$$

4.2.4 Test Results

The minimum detectable wavelength shifts versus different wavelength steps, receiver bandwidths and Q-factors are shown in Figure 4.4, Figure 4.5 and Figure 4.6 respectively.

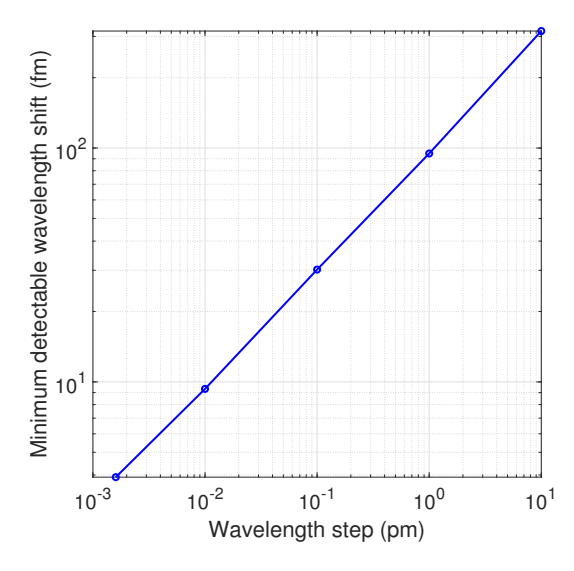


Figure 4.4: $\Delta \lambda_{min}$ versus wavelength steps

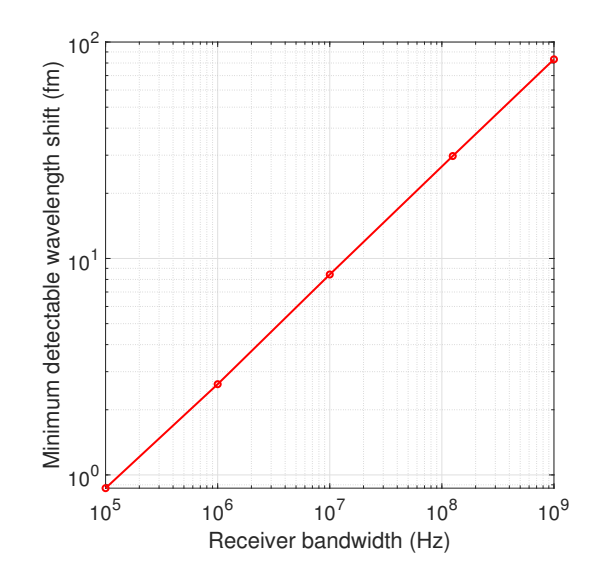
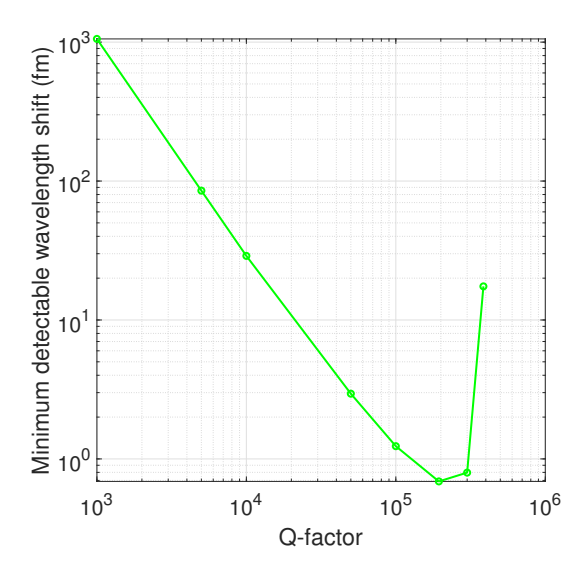


Figure 4.5: $\Delta \lambda_{min}$ versus photoreceiver bandwidths



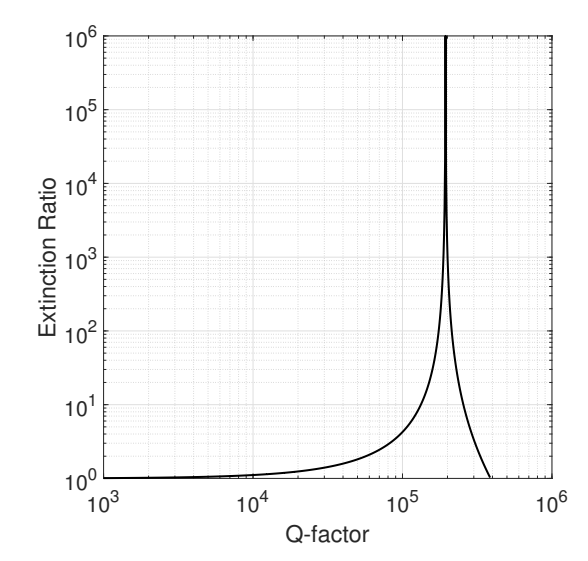


Figure 4.6: $\Delta \lambda_{min}$ versus different Q-factors

Figure 4.7: Extinction ratio versus different Q-factors

It can be seen that the wavelength shift $(\Delta \lambda_{min})$ starts from roughly 4 fm to 316 fm for wavelength steps from 1.6 fm to 10 pm. The increase of $\Delta \lambda_{min}$ for varying wavelength steps increases with a logarithmic slope of 0.5. This makes sense, since higher wavelength steps mean there are less data points considered, making it harder to accurately curve-fit these points.

For varying photoreceiver bandwidths, $\Delta \lambda_{min}$ starts from 0.87 fm and increases up to 83.2 fm with a logarithmic slope of 0.5 fm as well. This result makes also sense. From Equation 4.6 and Equation 4.7, the receiver bandwidth is positively correlated with the intensity noise levels, which can affect $\Delta \lambda_{min}$ as mentioned before.

When varying the Q-factor, $\Delta \lambda_{min}$ (and therefore also the LOD) decreases from 1055 fm for a Q-factor of 1000 to 0.69 fm for a Q-factor of 1.94 · 10⁶ (critical coupling), resulting in a fitted logarithmic slope of roughly -1.39. This result matches with Equation 4.2, where it has been shown that the iLOD decreases with an increasing Q-factor. However, when the Q-factor passes $1.94 \cdot 10^6$, the ring resonator becomes undercoupled and starts to show a large increase in $\Delta \lambda_{min}$. When a ring resonator gets undercoupled, R_{min} from Equation 4.11 starts to increase and therefore the extinction ratio decreases as shown in Figure 4.7. Having a smaller extinction ratio due to a higher R_{min} makes it harder to accurately curve-fit transmission points subjected to intensity noise, resuting in a larger $\Delta \lambda_{min}$. From this, it can be concluded that the smallest $\Delta \lambda_{min}$ can be obtained when the ring resonator gets critically coupled.

Finally, the limit-of-detection obtained from this analysis ranges from $2.6 \cdot 10^{-5} \, RIU$ for a Q-factor of 1000 up to $1.7 \cdot 10^{-8} \, RIU$ in case of a critical coupling when considering a sensitivity of roughly $40.2 \, nm/RIU$ calculated using RectWG and the chosen ring resonator specifications mentioned in subsection 4.2.1.

4.2.5 Influence of Noise Sources on Measurement Uncertainties

It can be seen from these results that the minimum detectable wavelength shift remain below 1 pm most of the time. This is small compared to the calculated temperature sensitivity of the respective ring resonator of around 80 pm/K (using RectWG) and the wavelength repeatability of $\pm 8 pm$ (from Santec TSL-570 Type A [87]). It can therefore be concluded

that the latter noise sources are dominant compared to the influence of the intensity noise on the measurement resolution. Therefore, methods for compensating thermal effects as well as wavelength repeatability are discussed in section 3.4. Wavelength repeatability noise can also be decreased by choosing Santec TSL-570 (Type C) [87] instead, valued at $\pm 1.5 \, pm$ (which still causes a larger minimum detectable wavelength shift). Finally, an overview of different noise sources and their effect on the measurement resolution $(\Delta \lambda_{min})$ are shown in Table 4.1.

Noise source	Effect on $\Delta \lambda_{min}$
Intensity noise	$<= \pm 1 pm$
Temperature drift	$\pm 80 pm/K$
Wavelength repeatability	e.g. $\pm 1.5 pm$ or $\pm 8 pm$

Table 4.1: Comparison of the effect of different noise sources on $\Delta \lambda_{min}$

Chapter 5

Modeling of Integrated Photonics for Distributed Force Sensing

In the next sections, the steps for modeling the photonic integrated circuit for distributed force sensing are shown and explained. It starts with the device specifications, which provides an overview of both the requirements as explained in section 1.3 and the corresponding design challenges that arise. Afterwards, the actual modeling methods using RSoft (Synopsys) simulation software are introduced.

5.1 Device Specifications

Several requirements for the distributed force sensor have been shown in section 1.3. In this section, different methods to satisfy the requirements are discussed.

An elastic polymer layer must be used as a cladding material for sensing the forces exerted by the cells. For this design thesis, a PDMS cladding is used with the measured refractive index of $n_{PDMS} = 1.3892$ from Zhang et al. [90]. However, other polymer types can also be considered after this thesis design project. Besides the refractive index, the thermo-optic coefficient and the stress-optic coefficient are also important properties to consider. Special attention must be paid to the thermo-optic coefficient, since subsection 5.5.4 has shown that the temperature sensitivity (influenced by the thermo-optic coefficient) of both the force sensor and the reference sensor must be equal to cancel out all the spectral noise sources (i.e. temperature drift and wavelength repeatability, which are discussed in chapter 4). Note that it was concluded in subsection 3.4.6 that the reference sensor method is the optimal solution to combat temperature drift. The stress-optic coefficient of a polymer is important for characterizing the mechanical sensitivity of the distributed force sensor.

Since reference sensors are going to be used, the seperation distance between the reference, force sensors and the out-of-plane grating couplers as well as the cladding material for the reference sensors need to be determined. Since both type of sensors will have a different cladding material (as explained in subsection 3.4.1), the fabrication processes of depositing these polymers on top of the same chip should not interfere with each other. Putting the sensors far away from the grating coupler prevents the latter component getting covered by polymer (grating couplers must have air cladding). The distance between these three component types must be around hundred of microns (T. Erdogan and W.J. Westerveld, personal communication, November 2, 2022). The cladding material should also be chosen based on the refractive index, thermo-optic coefficient and the youngs modulus, similar to the polymer cladding for force sensing. Since it has been shown subsection 5.5.4 that the temperature sensitivity of both sensor types should be equal, the thermo-optic coefficient of the reference sensor cladding material should be as close as possible to the one of the cladding material for force sensing (PDMS in this case, which has a thermo-optic coefficient of $-4.5 \cdot 10^{-4} \, K^{-1}$ [91]). A commercial hybrid polymer from Fraunhofer ISC called Ormocer [92] is a promising material for this, since it has a thermo-optic coefficient of -4 to $-1.5 \cdot 10^{-4} \, K^{-1}$, a refractive index of around $n_{Ormocer} = 1.5$ and a Youngs modulus of potentially in the gigapascal levels, which allows the reference sensor to be shielded from the forces exerted by the cells. Since the optical properties of both polymer types aren't exactly equal, the waveguide width of either the force or reference sensor should be adjusted in order to equalize both temperature sensitivities.

To obtain high spatial sensing resolution, the sensors must have a very small footprint. It has been concluded that ring and disk resonators are for this reason the ideal integrated photonic devices as mentioned in section 3.3. Small ring and disk resonators to show higher radiation losses due to the sharp constant waveguide bends, resulting in a lower Q-factor and therefore also a lower measurement resolution. To prevent excessive propagation

loss, fundamental transverse electric (TE0) mode is preferred over transverse magnetic (TM) mode. Also, using silicon with its high refractive index provides high confinement of the mode compared to other material platforms discussed in section 3.1.

For this thesis, the distributed force sensor should also have as many sensors as possible for distributed sensing over a wide spatial range. This means fitting as many resonance peaks as possible on an intensity spectrum with a bandwidth that is limited by the grating coupler. For this to happen, the free spectral range (FSR) of a resonator, which is the seperation distance between multiple resonance orders m, should be as high as possible. The FSR can be calculated with the following equation.

$$\Delta \lambda_{FSR} = \frac{\lambda_m^2}{n_q(\lambda_m)L} \tag{5.1}$$

It can be seen from Equation 5.1 that a smaller roundtrip length of a resonator (L) will result in a larger FSR. This means the ring or disk radii should be small in order for this to happen, which conveniently aligns with the previous requirement of having small sensors for high spatial sensing resolution. The resonance peaks should also be as sharp as possible (i.e. high Q-factor) to fit more resonance peaks without overlapping one with another, which requires high mode confinement. Again, this is also the case for the previous requirement. However, higher mode confinement generally means light with lower optical intensity is propagating in the cladding, resulting in a lower sensitivity.

Finally, the device will be fabricated with Cornerstone's photolithography machine that operates at a wavelength of $\lambda = 248 \, nm$ [93]. This does put a limit on the smallest features and gaps that can be fabricated. The waveguide width cannot be smaller than $350 \, nm$ to prevent the collapse of the photoresist during the patterning. The absolute minimum gap between structures is $200 \, nm$.

5.2 Waveguide Bend Loss Modeling

5.2.1 Study

Due to constant bending of the waveguide, light propagation inside ring resonators will continuously experience radiation loss. Combined with absorption and scattering losses, the propagation loss of ring resonators for each roundtrip can be determined (i.e. the term α in Equation 3.4), which affects the shape of the resonance peak (i.e. the Q-factor and exctinction ratio). This in turn influences the measurement resolution and the limit-of-detection, which has been shown in subsection 4.2.4. The radiation loss due to bending can be determined using RSoft's simulation software FemSIM (in 3D). This simulation tool can solve Helmholtz equations, plot the mode field distribution and calculate the corresponding complex effective index. The latter can be used to determine the radiation. The next sections show how to obtain the complex effective index and how to calculate the bend loss with it.

5.2.2 Model and Parameters

For calculating the mode fields of a bend, only a single strip waveguide with the desired cross-section dimensions is required. The length of this waveguide is for this simulation study irrelevant. A waveguide width of $450\,nm$ and a thickness of $220\,nm$ will be applied for most of the simulations, except for analyzing the effect of fabrication errors that result in a change of these cross-sectional dimensions. For RSoft's bend simulations, the horizontal center of the waveguide should be placed at X=0 of the spatial domain to simulate a bend waveguide at an arbitrary radius, since the bend origin is located at X=-R (where R is the radius of the bend). The propagation wavelength is set as $1.55\,\mu m$, which is wavelength used for telecommunication [30].

The waveguide is located on top of a SiO_2 BOX, which has a refractive index of $n_{SiO_2} = 1.444$. This model can implemented in RSoft with either the Rib/Ridge or the Multilayer 3D structure with the latter being chosen for this simulation study. Silicon is used as the waveguide material, which has a refractive index of $n_{Si} = 3.476$. Therefore, the index difference between the waveguide and the BOX layer is $\Delta n = 2.032$. For the force sensor cladding, a PDMS cladding with a mass ratio between the main agent and the curing agent of 5:1 is used with the measured data from Zhang et al. [90]. The complex refractive index at a wavelength of $1550\,nm$ is measured to be $n_{PDMS} = 1.3892 + i7.83 \cdot 10^{-6}$. For the reference sensor cladding (i.e. Ormocer), a refractive index of 1.53 and a TOC of $-2 \cdot 10^{-4}\,K^{-1}$ have been chosen, since these values are within the specified range [92]. In subsection 7.2.2, both optical property values are replaced by n = 1.543 and $-3.385 \cdot 10^{-4}\,K^{-1}$, representing another commercial hybrid polymer called "Ormocore" [94], which is based on Ormocer. The new optical property values are required to equalize temperature sensitivities for both sensor types for the new ring resonator design shown in section 7.2 (this cannot be done with the former optical property values).

The spatial domain as shown in Figure 5.1 should encompasse the entire waveguide as well as the evanescent fields. A grid size of $0.01\mu m$ in all directions is utilized, which is small enough to accurately plot the mode field. As for the domain boundaries, putting the vertical boundary edges around $Y=\pm 2\,\mu m$ (above and below the waveguide) is sufficient to cover most of the evanescent fields at those parts of the waveguide. The same cannot be said about the boundary edge location on the left and the right of the waveguide when considering bends. Due to the bend, the mode field radiates outwards, creating a larger evanescent field at the outer radius of the bend. For this reason, the domain boundary edge should be placed around $X=5\,\mu m$ (to the right waveguide center) to encompasse the large evanescent field. The simulation parameter Allow Leaky Modes in Advanced Options must be enabled to simulate this large evanescent field due to radiation. The domain boundary edge location to the left hand side of the waveguide cannot decrease below X=-R/2 in order for the solver to give correct results. Therefore, the boundary edge location to the left of the waveguide should change accordingly especially for bends with smaller radii.

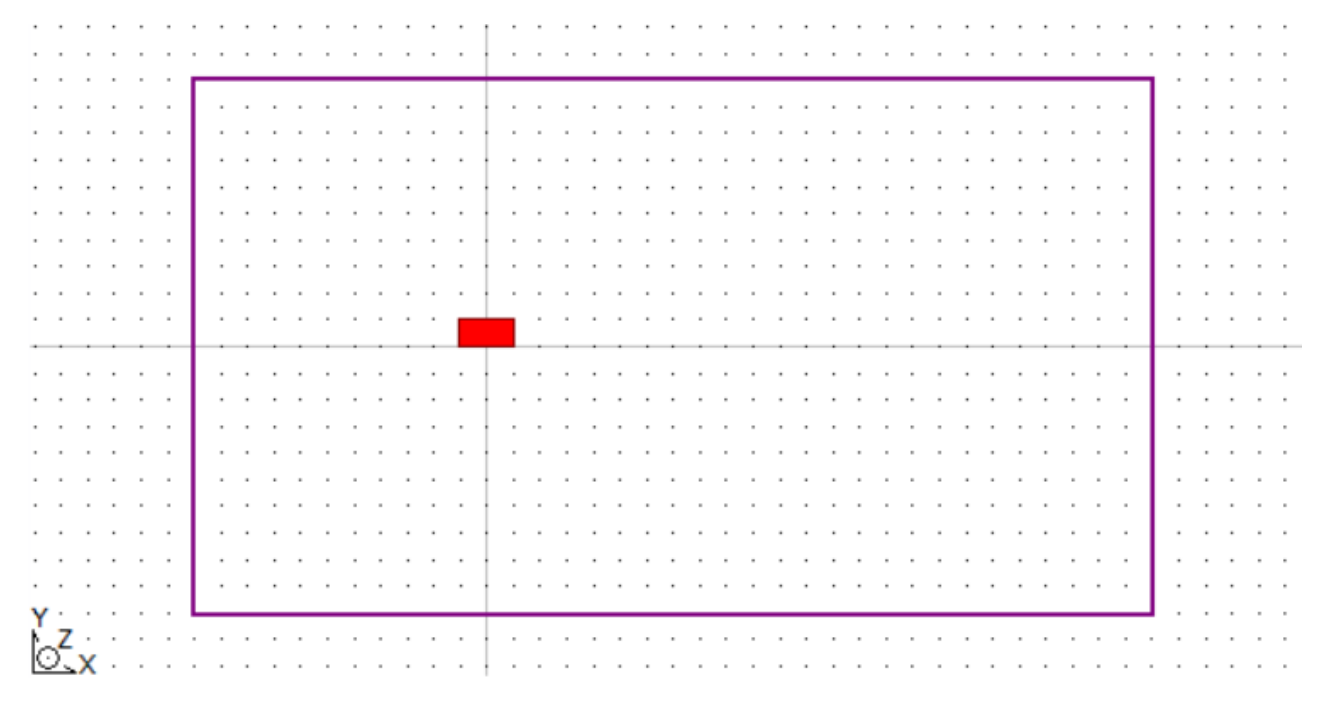


Figure 5.1: Cross-sectional view of CAD model in FemSIM

Besides the domain boundary edges as explained above, perfectly-matched layers (PML) are placed at these edges outside of the spatial domain. These layers absorb the mode fields hitting the boundary edges. Without it, light will be reflected from the edges instead, which is an inaccurate phenomenom. Increasing the PML-thickness gives more accurate results, but is also more computational demanding. For bend simulations using FemSIM, having PML added to the boundary edges in the horizontal direction is obligatory, since optical power is radiating in this direction. No PML have been added in the vertical direction, since the mode field in that direction is well confined. For this study, a PML-thickness in the X-direction of $1 \mu m$ is chosen.

By enabling the dispersion option in the simulation parameters, the both the effective indices as well as the group indices $n_g(\lambda)$ can be calculated at different wavelengths. This can be used to calculate for example the FWHM with Equation 4.3 or the FSR with Equation 5.1.

Finally, the number of modes that needs to be determined can also be chosen. Increasing this number allows the amount of supported modes in a waveguide to be determined. However, this number is set to 1 for waveguide cross-section of $450x220\,nm$ which only supports TE0 mode. Higher order mode analysis for the new ring resonator design introduced in section 7.2 is left as a follow-up research.

5.2.3 Post-Processing

After simulating, the complex effective index will be given for each calculated mode. As mentioned before, the complex effective index can be used to calculate the propagation loss in bends. It starts by substituting the following equation in plane harmonic wave equation (in e.g. Equation 2.3).

$$k = \frac{\omega(n+i\kappa)}{c} \tag{5.2}$$

where $n+i\kappa$ is the complex refractive index. Equation 5.2 is similar to Equation 2.5, but for a space not limited to vacuum. Substituting it in Equation 2.3 results in:

$$E = E_0 e^{i\left(\frac{\omega(n+i\kappa)}{c}z - \omega t\right)} \tag{5.3}$$

which can be rewritten into:

$$E = E_0 e^{-\frac{\omega \kappa z}{c}} e^{i(kz - \omega t)} \tag{5.4}$$

It can be seen that a exponential decaying term $e^{-\frac{\omega\kappa z}{c}}$ is in Equation 5.4. The power term can be rewritten to $\frac{2\pi\kappa}{n\lambda}z$ using the following equations

$$v = -\frac{c}{n} \tag{5.5}$$

$$f = \frac{v}{\lambda} \tag{5.6}$$

$$\omega = 2\pi f \tag{5.7}$$

where v is the propagation speed of light and f is the frequency of the wave. The rewritten power term contains terms that are common in integrated photonics. Finally, the following equations can be used to calculate α and the propagation loss in dB respectively.

$$\alpha_{rad} = e^{-\frac{2\pi\kappa}{n\lambda}z} \tag{5.8}$$

$$Loss_{dB} = -20log_{10} \left(e^{-\frac{2\pi\kappa}{n\lambda}z} \right) \tag{5.9}$$

Afterwards, the calculated roundtrip loss α can be substituted in Equation 3.4 to plot the optical power spectrum. When assuming the transmission coefficient τ is equal to α , then the FWHM, Q-factor and the extinction of the resonance peaks corresponding to critical coupling can be determined.

With the known bending radius R as well as the calculated effective index n_{eff} and the group index n_g , the resonance wavelengths of a ring resonator with a radius R can be determined using Equation 3.2 with $\lambda_c = 1550 \, nm$.

5.3 Refractive Index Sensitivity for Force Detection

5.3.1 Study

This section specificially focuses on the force detection sensitivity of biological cells, of which the working principle has already been explained in section 1.2. As shown for the first time in subsection 3.3.1, the sensitivity is a measure of how much the resonance peak shifts due to changes in the optical path length of the ring resonator caused by in this case changes in the effective index n_{eff} . The force detection sensitivity can be calculated using Equation 3.3 with χ being refractive index n_{clad} , resulting in Equation 5.10.

$$\frac{\partial \lambda}{\partial n_{clad}} = \frac{\lambda_c}{n_g} \frac{\partial n_{eff}}{\partial n_{clad}} \tag{5.10}$$

Therefore, the terms n_g and $\frac{\partial n_{eff}}{\partial n_{clad}}$ from Equation 5.10 must be obtained using FemSIM bend simulations, similar to what has been shown in section 5.2. The latter can be obtained by simulating twice using different cladding refractive indices n_{clad} in order to get two different n_{eff} .

5.3.2 Model and Parameters

Most settings from subsection 5.2.2 can be used for this simulation as well, except for the (real) refractive index of the PDMS cladding. For force sensing of biological cells, only the refractive index of the PDMS cladding changes due to its deformation which is caused by the exerted cell forces. The effective index does not scale linearly with the cladding refractive index n_{clad} over a large n_{clad} range as shown in Figure 5.2. Therefore, the change in the cladding refractive index should be sufficiently small to linearize the relation between n_{eff} and n_{clad} , which in turn also linearizes the sensitivity of the integrated photonic sensor. For this simulation, the refractive index of the PDMS has been rounded to 1.39 from 1.3892 in subsection 5.2.2.

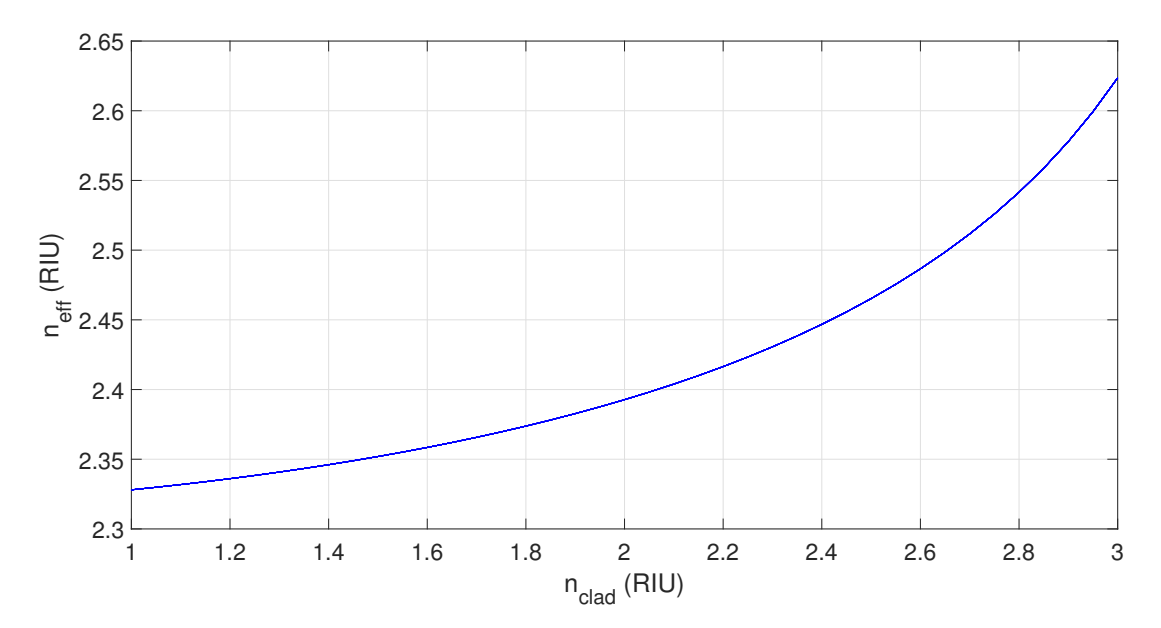


Figure 5.2: Effective index n_{eff} versus the cladding refractive index n_{clad} for silicon strip waveguide with a cross-sectional area of $450x220\,nm$ on top of SiO_2 BOX layer calculated using RectWG

Another method to determine $\frac{\partial n_{eff}}{\partial n_{clad}}$ is to curve-fit a polynomial function in multiple data points (e.g. at $n_{clad} = 1.37$ to 1.41 with increments of 0.05) and subsequently derive the polynomial function at $n_{eff} = 1.3892$. As explained in subsection 5.3.1, the group index n_g needs to be determined among others in order to calculate the sensitivity using Equation 3.3. Just like in subsection 5.2.2, this can be done by enabling the

calculate the sensitivity using Equation 3.3. Just like in subsection 5.2.2, this can be done by enabling the dispersion option in the simulation parameters. The wavelength at which the sensitivity is calculated is most of the time at $\lambda_c = 1550 \, nm$. However in section 7.4, the sensitivity of a force sensing ring resonator $(R_1 = 1.949 \, \mu m)$ is evaluated at $\lambda_{m=19} = 1553.167 \, nm$ instead.

5.3.3 Post-Processing

After obtaining different effective indices for varying cladding refractive indices, the term $\frac{\partial n_{eff}}{\partial n_{clad}}$ from Equation 3.3 can be calculated, as shown in Equation 5.11.

$$\frac{\partial n_{eff}}{\partial n_{clad}} \approx \frac{\Delta n_{eff}}{\Delta n_{clad}} = \frac{n_{eff,2} - n_{eff,1}}{n_{clad,2} - n_{clad,1}}$$
(5.11)

The derivate term is approximated as a slope that intersects at $[n_{clad,1}, n_{eff1}]$ and $[n_{clad,2}, n_{eff2}]$, with $n_{clad,1} = 1.3892$ and $n_{clad,2}$ is 1.39. Subsequently, the sensitivity can be computed with $\frac{\partial n_{eff}}{\partial n_{clad}}$, n_g that has been determined from the simulations and the wavelength from the input parameters. For most simulations in this report, the sensitivity is evaluated at $\lambda_c = 1.55 \, \mu m$. In section 7.3, the sensitivity of a force sensing ring resonator is analyzed at $\lambda_{m=19} = 1.553167 \, \mu m$ instead.

As explained in subsection 5.3.2, the term $\frac{\partial n_{eff}}{\partial n_{clad}}$ can also be determined by curve-fitting a polynomial function in multiple data points) and subsequently derive the polynomial function at $n_{eff} = 1.3892$.

5.4 Coupling Simulations

5.4.1 Study

Similar to the roundtrip loss in a ring resonator (α) , the transmission coefficient τ from Equation 3.4 also plays an important role for shaping the resonance dips in the spectrum. Determining τ together with α in section 5.2 is an efficient way to plot the wavelength spectrum with the resonance peaks. There are multiple simulation methods to achieve this. Both Beam Propagation and Eigenmode Expansion (EME) are more suitable for parallel waveguides. For ring resonators (especially when the radius is very small), Finite Difference Time Domain (FDTD) or RSoft's FullWAVE software is a better option, since it can account for sharp bends in the spatial-domain. With FDTD, the propagation of a mode field calculated with FemSIM along a photonic device

model can be rigorously simulated (i.e. solving Maxwell's equations without approximations). This way, τ can be derived by monitoring the intensity differences between the mode launch input and either the transmitted or coupled output. The following sections show how to perform these simulations.

5.4.2 Model and Parameters

To obtain the transmission coefficient τ , two separate simulations need to be carried out. The first simulation is a FemSIM analysis where the mode field of the input bus waveguide is simulated. For this, most parameters mentioned in section 5.2 can be used again. This time, the bend simulation option must be disabled, since the bus waveguide is (generally) straight. The cross-sectional dimension can be chosen to be different, meaning both the width and height should be adjusted accordingly. The mode fields determined with FemSIM can then subsequently be used as a launch parameter in FullWAVe (by choosing the launch type: file).

The FullWAVE model as shown in Figure 5.3 consists of a straight input bus waveguide and a bend waveguide (with a certain radius) representing a part of the ring resonator, with the width-direction of the input bus waveguide representing the x-direction and waveguide thickness-direction the y-direction (which is similar to FemSIM). This bend is located right next to the bus waveguide with a gap length in between that is going to be varied from $200\,nm$ to $300\,nm$. The gap length of $200\,nm$ being the smallest gap size that Cornerstone can fabricate. The 3D structure used here is multilayer with silicon waveguide, SiO_2 BOX and PDMS cladding, which results in the same structure as the one from FemSIM simulations.

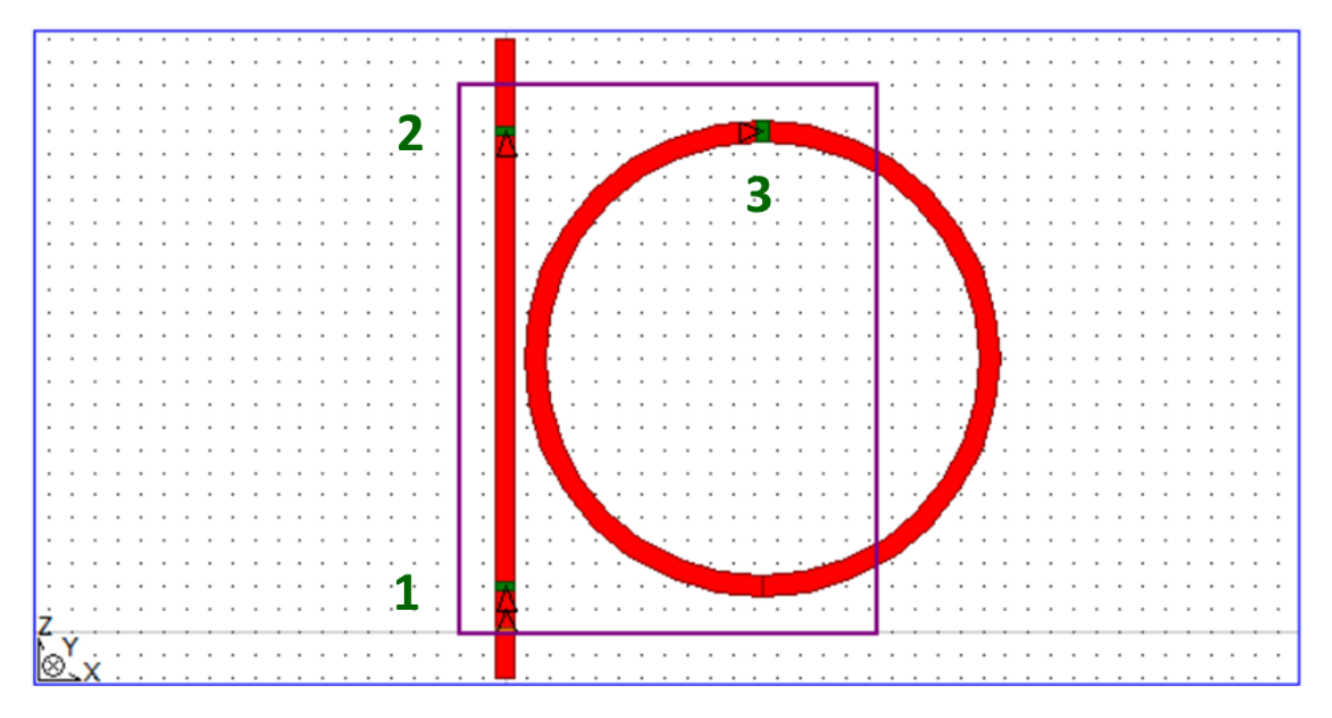


Figure 5.3: Top view of the CAD model in FullWAVE. Overlap integral monitors are shown in green. The launch field is located at the bottom of the bus waveguide. The ring resonator radius in this example CAD model is $5 \,\mu m$

Three overlap integral monitors are placed in the CAD model. Monitor 1 is located at the input close to the launch field, monitor 2 is placed at the output of the bus waveguide and monitor 3 is placed on the ring resonator. The overlap integral monitors can measure the optical power at the monitor locations relative to the launch location. This is also the reason why the simulation domain does not include the entire ring resonator, since a ring structure will result in the mode fields eventually returning to the coupling part and interfere with the overlap monitors. By partially covering the ring resonator in the simulation domain as shown in Figure 5.3, the propagating mode fields will eventually propagate into the PML layer and disappear. The transmission coefficient τ can be determined by comparing the monitor values at the input and output of the bus waveguide.

Besides the spatial-domain covering a part of the ring resonator and the entire input bus waveguide, evanescent fields for all waveguides should also be included in the domain. For the latter, a domain boundary edges are placed $1\mu m$ away from the center of all waveguides (i.e. in the x- and y-direction). This is smaller than the waveguide-boundary seperation distance of $2\mu m$ in FemSIM as stated in section 5.2, since seperation distance

of $1 \mu m$ is found to be already sufficient after multiple explorative simulations and is also less computationally demanding especially for computation heavy simulation such as FDTD.

Remaining essential simulation parameters for FullWAVE include continuous wave (CW) simulation at a wavelength of $1550\,nm$, PML widths of $0.5\,\mu m$ in all directions and the enabling of a nonuniform grid. For getting an estimate of τ , a FDTD analysis with the mode field propagating at a single wavelength is sufficient, hence CW. Multiple wavelength simulations can be used to directly determine the resonance spectrum of a ring resonator. However, this is very computationally demanding, which is why it has been chosen to use CW in combination with Equation 3.4 instead (see also subsection 5.4.3), similar to FemSIM simulations. The PML widths of $0.5\,\mu m$ are standard parameters that gives accurate results after multiple test simulations while preventing the simulation time to become to long. By enabling nonuniform mesh, the grid structure is automatically smoothened at the material interfaces. This allows waveguide dimensions to be chosen in which the grid size does not have to fit integer amount of times.

5.4.3 Post-Processing

After obtaining the overlap monitor values, τ and κ can be determined by using the following equations.

$$\tau_{RSoft} = \sqrt{\frac{Monitor_2}{Monitor_1}} \tag{5.12}$$

$$\kappa_{RSoft} = \sqrt{\frac{Monitor_3}{Monitor_1}} \tag{5.13}$$

With both τ and κ , the intensity loss calculated by RSoft can be determined using Equation 5.14.

$$I_{Loss} = 1 - \tau_{RSoft}^2 - \kappa_{RSoft}^2 \tag{5.14}$$

If $I_{loss} \ll \kappa_{RSoft}^2$, then I_{loss} can be neglected and the unit power expression of $\tau_{RSoft}^2 + \kappa_{RSoft}^2 \approx 1$ can be assumed. This means that the actual transmission coefficient is close to the value of τ_{RSoft} . On the other hand when $I_{loss} \approx \kappa_{RSoft}^2$, then the intensity loss cannot be neglected anymore. This indicates that the actual transmission coefficient is somewhere between τ_{RSoft} and $\sqrt{1-\kappa_{RSoft}^2}$, which cannot be $\sqrt{1-\kappa_{RSoft}^2}$ itself. The reason for this is that κ_{RSoft}^2 from this term also includes radiation losses of the waveguide bend.

The computed transmission coefficient can then be compared with α_{rad} determined with FemSIM as explained in section 5.2 to determine whether the ring resonator is critically coupled or not.

5.5 Temperature Drift Modeling

5.5.1 Study

The duration of the measurement of forces exterted by the cells takes several hours to a few days. This means the ambient temperature in the laboratory will change during the measurement. It has been shown in subsection 4.2.5 that the temperature drift can shift the resonance wavelength as well, due to the temperature changes inducing refractive indices of all the materials used for the photonic integrated circuit. The magnitude of the resonance wavelength caused by the temperature drift is the temperature sensitivity (also explained in section 3.3). This can be calculated using Equation 5.15.

$$\frac{\partial \lambda}{\partial T} = \frac{\lambda_c}{n_a} \frac{\partial n_{eff}}{\partial n_{material}} \frac{\partial n_{material}}{\partial T}$$
 (5.15)

It can be seen from Equation 5.15 that the temperature induces a refractive index change for all the materials (not just the cladding). This subsequently affects n_{eff} , similar to what is shown in Equation 5.10. The rate at which the refractive index changes per Kelvin differs for each material due to a material property called thermo-optic coefficient $(TOC \text{ or } \frac{\partial n}{\partial T})$. In this study, multiple simulations are carried out to determine the change in effective index for varying temperatures in order to obtain the temperature sensitivity.

The temperature sensitivity calculation method described in this section holds for small temperature drifts (ΔT) . The reason for this is that the temperature sensitivity changes with the wavelength (as shown in Figure 7.9 and Figure 7.23). If the resonance wavelength shifts due to changes in temperature, the rate at which this resonance wavelength shifts for varying temperatures (i.e. the temperature sensitivity) also changes.

5.5.2 Model and Parameters

Many parameters mentioned in subsection 5.2.2 can be used here again, except for the refractive indices of all the materials and the dimensions of the waveguide. The change of refractive index due to temperature drift can be determined with Equation 5.16.

$$\Delta n = \frac{\partial n}{\partial T} \Delta T \tag{5.16}$$

The thermo-optic coefficient for silicon, silicon-dioxide, PDMS is $1.83 \cdot 10^{-4} \, K^{-1}$, $0.95 \cdot 10^{-5} \, K^{-1}$ and $-4.5 \cdot 10^{-4} \, K^{-1}$ [91] respectively. For Ormocer, the refractive index can be varied between $-4 \cdot 10^{-4} \, K^{-1}$ to $-1.5 \cdot 10^{-4} \, K^{-1}$. Due to thermal expansion, both the width and the height of the waveguide can also increase or decrease depending on the temperature. The thermal expansion coefficient for silicon is $2.6 \cdot 10^{-6} \, K^{-1}$.

 ΔT is chosen to be $\pm 10\,K$. Multiple FemSIM simulations as described in section 5.2 have been carried out to determine n_{eff} at different temperatures in order to obtain $\frac{\partial n_{eff}}{\partial T}$. It should be noted that the thermo-optic coefficient also changes with temperature [73]. Due to the lack of data (specifically the provided data for Ormocer), the thermo-optic coefficient is assumed to be uniform over this temperature range in this study. However, the effect of temperature difference on the thermo-optic coefficient should be experimentally characterized to obtain a more accurate temperature sensitivity model. Although it has been stated in subsection 5.2.1 that the temperature sensitivity holds for small temperature drift ranges only, which isn't the case for $\Delta T = \pm 10\,K$, the term $\frac{\partial n_{eff}}{\partial T}$ from Equation 5.17 remains linear even at this temperature drift range (as long as the propagation wavelength is constant). Example of this can be found in Figure 7.8 and Figure 7.22. This means the final temperature sensitivity result does not get affected by the chosen temperature drift range in this analysis.

Finally, the temperature sensitivities are for the most part analyzed at $\lambda_c = 1550 \, nm$. Only in few cases (e.g. in section 7.4), the temperature sensitivity is analyzed at a different wavelength.

5.5.3 Determining Temperature Sensitivity

After obtaining different effective indices corresponding to different ΔT as well as n_g from the simulation, then the temperature sensitivity can be calculated with Equation 5.17.

$$\frac{\partial \lambda}{\partial T} = \frac{\lambda_c}{n_q} \frac{\partial n_{eff}}{\partial T} \tag{5.17}$$

where the term $\frac{\partial n_{eff}}{\partial T}$ can be approximated with Equation 5.18, similar to Equation 5.11.

$$\frac{\partial n_{eff}}{\partial T} \approx \frac{\Delta n_{eff}}{\Delta T} = \frac{n_{eff,2} - n_{eff,1}}{T_2 - T_1} \tag{5.18}$$

The term $\frac{\partial \lambda}{\partial T}$ is sometimes denoted as S_T in this report.

Another method to determine $\frac{\partial n_{eff}}{\partial T}$ is to line-fit the data points of effective refractive indices n_{eff} at different temperatures T using a first-order polynomial equation (since relation between the effective refractive index and different temperature is linear for a constant TOC-value) and subsequently determining the slope of the fitted line.

5.5.4 Spectral Noise Compensation

In section 3.4, it has been explained that a ring resonator with a different cladding material can be used as a reference temperature sensor for the force sensor in order to cancel out the resonance wavelength shift due to temperature drift. The following relevant calculations are from Xu et al.[73]. The total resonance shift for both the force sensing and the reference ring resonator (both of which can be determined from interrogation) can be determined with the following equations.

$$\Delta \lambda_{sense,tot} = \Delta \lambda_{sense,force} + \Delta \lambda_{T,sense}$$

$$= \Delta \lambda_{sense,force} + \left(\frac{\partial \lambda}{\partial T}\right)_{sense} \Delta T$$
(5.19)

$$\Delta \lambda_{ref,tot} = \left(\frac{\partial \lambda}{\partial T}\right)_{ref} \Delta T \tag{5.20}$$

Equation 5.20 can be substituted in Equation 5.19 in order to remove the ΔT term. This results in the following equation.

$$\Delta \lambda_{sense,tot} = \Delta \lambda_{sense,force} + \frac{\left(\frac{\partial \lambda}{\partial T}\right)_{sense}}{\left(\frac{\partial \lambda}{\partial T}\right)_{ref}} \Delta \lambda_{ref,tot}$$
(5.21)

Equation 5.21 can then be rewritten to calculate $\Delta \lambda_{sense,force}$, resulting in Equation 5.22.

$$\Delta \lambda_{sense,force} = \Delta \lambda_{sense,tot} - \frac{\left(\frac{\partial \lambda}{\partial T}\right)_{sense}}{\left(\frac{\partial \lambda}{\partial T}\right)_{ref}} \Delta \lambda_{ref,tot}$$
(5.22)

It can be seen in Equation 5.22 that it does not matter whether the temperature sensitivities $(\frac{\partial \lambda}{\partial T})$ of both the (force) sensor and the reference ring are the same or not in order to calculate $\Delta \lambda_{sense,force}$. However, the difference in temperature sensitivity can become a problem when the wavelength repeatability is considered, which the analytical model described above did not do. Adding wavelength repeatability $(\Delta \lambda_{WLR})$ in Equation 5.19 and Equation 5.20 results in the following equations.

$$\Delta \lambda_{sense,tot} = \Delta \lambda_{sense,force} + \Delta \lambda_{T,sense} + \Delta \lambda_{WLR}$$

$$= \Delta \lambda_{sense,force} + \left(\frac{\partial \lambda}{\partial T}\right)_{sense} \Delta T + \Delta \lambda_{WLR}$$
(5.23)

$$\Delta \lambda_{ref,tot} = \left(\frac{\partial \lambda}{\partial T}\right)_{ref} \Delta T + \Delta \lambda_{WLR}$$
 (5.24)

Afterwards, the same steps from Equation 5.19 and Equation 5.20 to Equation 5.22 can be used for Equation 5.23 and Equation 5.24 to get Equation 5.25.

$$\Delta \lambda_{sense,force} = \Delta \lambda_{sense,tot} - \frac{\left(\frac{\partial \lambda}{\partial T}\right)_{sense}}{\left(\frac{\partial \lambda}{\partial T}\right)_{ref}} (\Delta \lambda_{ref,tot} - \Delta \lambda_{WLR}) - \Delta \lambda_{WLR}$$
 (5.25)

It can be seen from Equation 5.25 that $\Delta \lambda_{WLR}$ cannot be cancelled out unless both temperature sensitivities are equal, resulting in the fraction term becoming equal to 1. Since the reference ring resonator has a different cladding material to shield it from the forces exerted by the cells compared to the cladding material of the force sensor (PDMS), the temperature sensitivity of both sensors will likely not be same when similar cross-sectional dimensions are used for the waveguide (since the thermo-optic coefficient of both cladding materials are usually different). It has been proposed in this thesis to adjust the width of the reference ring resonator in order to tune its temperature sensitivity to be equal to the one of the force sensor.

5.6 Cross-Talk Analysis

5.6.1 Study

When designing a distributed force sensor by placing multiple bus waveguides and ring resonators close to one another as shown in Figure 7.29, the propagating electromagnetic field can potentially unintendedly couple to another ring resonator or bus waveguide (i.e. cross-talk). The distributed force sensor design from Figure 7.29 shows that the distance X_{min} is the smallest spacing between two waveguide besides the coupling gap, assuming both the horizontal and vertical seperation distance between ring resonators are the same. This means the cross-talk probability in this distributed force sensor design is the highest in that region. Therefore in this analysis, the cross-talk potential between a ring resonator and a bus waveguide from another ring resonator array will be explored.

5.6.2 Model and Parameters

The simulation model and parameters are similar to the ones of the coupling analysis (from section 5.4), since the cross-talk analysis also uses continuous wave (CW) FDTD simulations. However in the cross-talk analysis, a different CAD model is utilized as shown in Figure 5.4.

A ring resonator design from section 7.2 is used in this model (since the distributed force sensor design from Figure 7.29 also utilizes this design). The launch field is located at the right hand side of the ring resonator.

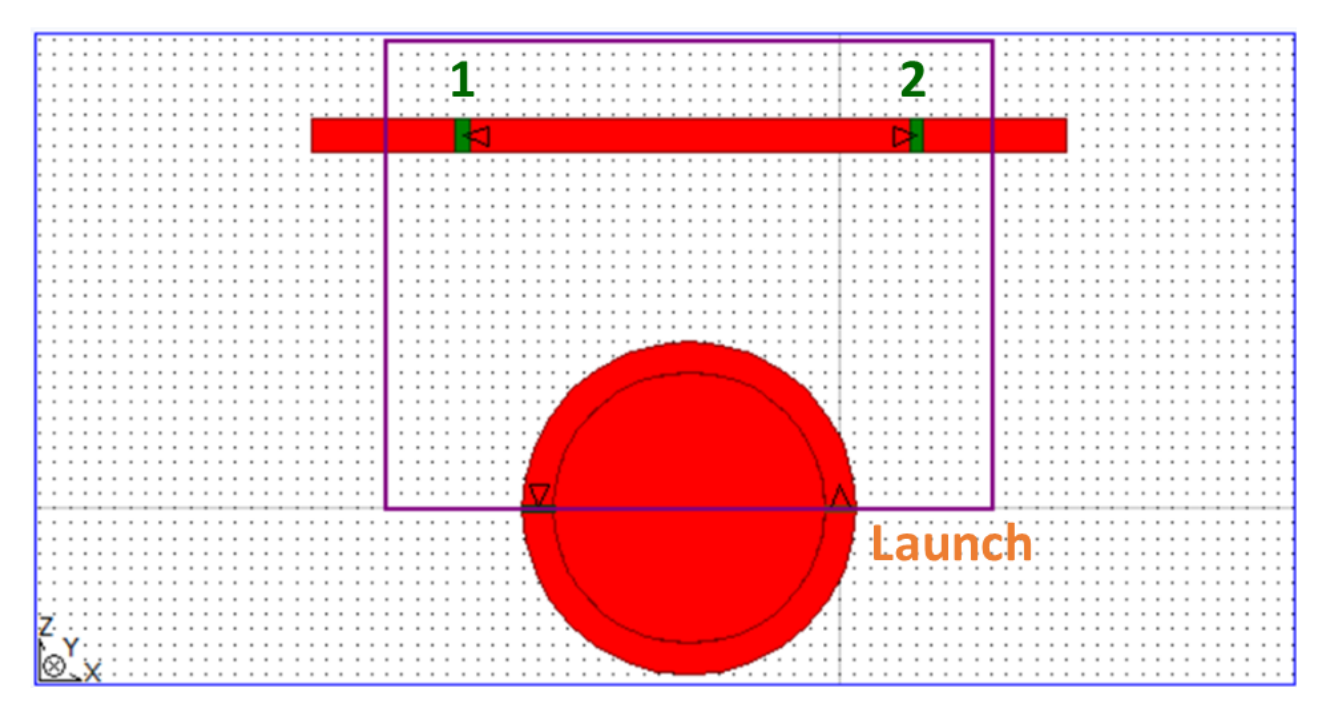


Figure 5.4: FDTD model for cross-talk analysis.

Since the launch field is located at a waveguide bend, the input launch field is therefore modeled with a FemSIM waveguide bend simulation (as explained in section 5.2). Afterwards, the electromagnetic field propagates and radiates along the 180° waveguide bend. Monitor 1 and 2 measures the overlap integral at both ends of the bus waveguide. The measurements of the latter two monitor is especially relevant, since these indiciate whether the distributed force sensor design experiences cross-talk.

A reference ring resonator from the design explained in section 7.3 will be analyzed for cross-talk. The reason for choosing to analyze a reference ring resonator is because the refractive index contrast ratio between the waveguide and cladding is lower compared to the one of the force sensor, resulting in a lower light confinement (see subsection 3.1.1) or higher radiation losses. The reference cladding refractive index is 1.543, representing the refractive index of Ormocore (as explained in subsection 7.2.1), which is higher than the refractive index of PDMS for the force sensor. The reference ring design has a cross-section of $410 \times 220 \, nm$ and a slab height of $100 \, nm$ as explained in subsection 7.2.1. However, the cross-section of the bus waveguide is $450 \times 220 \, nm$ instead. Finally, any spacing distance between the ring resonator and the bus waveguide (X_{min} from Figure 7.29) can be chosen, as long as the seperation distance of the ring resonator does not exceed $10 \, \mu m$ (due to the requirements of section 1.3).

The remaining simulation settings and parameters used in this analysis are the same as the ones described in the coupling analysis as shown in subsection 5.4.2.

5.6.3 Post-Processing

After obtaining the monitor values from the FDTD CW simulation, the presence of cross-talk can be determined by examining the monitor values of monitor 1 and 2.

Chapter 6

Fabrication Error Analysis

Since multiple integrated photonic resonators are going to be placed on a single bus waveguide, the resonance peaks of each resonator are placed close together. To be able to interrogate all these resonance peaks individually, the resonance peaks should not overlap each other. This makes the location of each resonance peaks relative to each other very important. However, fabrication errors can introduce deviated widths and thicknesses to the waveguide, resulting in a different effective index and therefore also an unwanted shift in the resonance wavelength. In this chapter, the consequences of fabrication errors and the influence on the design process are discussed.

6.1 Wafer-Scale Dimension Deviations

Wafer-scale dimension variations indicates the nonuniformity of the waveguide width and the thickness between multiple dies originating from the same chip. Cornerstone has stated that the silicon-on-insulator thickness can vary by $\pm 20 \, nm$ and the etch depth by $\pm 10 \, nm$ [93]. It also has been shown that the waveguide width can deviate around 10% [95]. Therefore in this thesis, it is considered that a nominal waveguide width of $450 \, nm$ can potentially decrease to $400\text{-}410 \, nm$ or increase to $490\text{-}500 \, nm$ due to fabrication errors at the wafer-scale.

6.2 Die-Scale Dimension Deviations

A more important source of fabrication error is the die-scale dimension deviation, where the widths of waveguides can vary within a single die. Unlike wafer-scale dimension deviations, this nonuniformity can potentially result in the overlap of resonance peaks due to individual waveguides being exposed to these small scale dimension variations. For example, research has shown that the die-scale width variation can be as small as 0.47 nm [96] or a resonance wavelength variation of < 0.6 nm [97]. This section analyzes magnitude of the die-scale waveguide dimension errors found in photonic integrated circuits fabricated at Cornerstone.

6.2.1 Width Nonuniformity Approximation from Measurements

Besides the existing research, W-Lab has also ordered photonic integrated circuits from Cornerstone consisting of varying ring resonator sizes and gap lengths intended for sensing graphene mechanics among others. The waveguide is designed to have $450x220\,nm$ cross-section and has $180\,nm$ thick SiO_2 hard mask layer on top. These photonic integrated circuits also contain five and ten multiplexed rings (with a ring radius of $5\,\mu m$) on a single bus waveguide as well, of which measurements have been made. Figure 6.1 and Figure 6.2 show the chip responses of 10 and 5 rings on a bus respectively with a gap length of $200\,nm$, resulting in critical coupling. These figures also show the assumed corresponding ring resonator radius for each of the resonance peak, where the first ring on the bus (with the smallest radius) corresponds to the first resonance peak in the FSR. The reason for assuming is that the corresponding resonance peak to a certain ring resonator cannot be determined with 100% certainty from the spectral response.

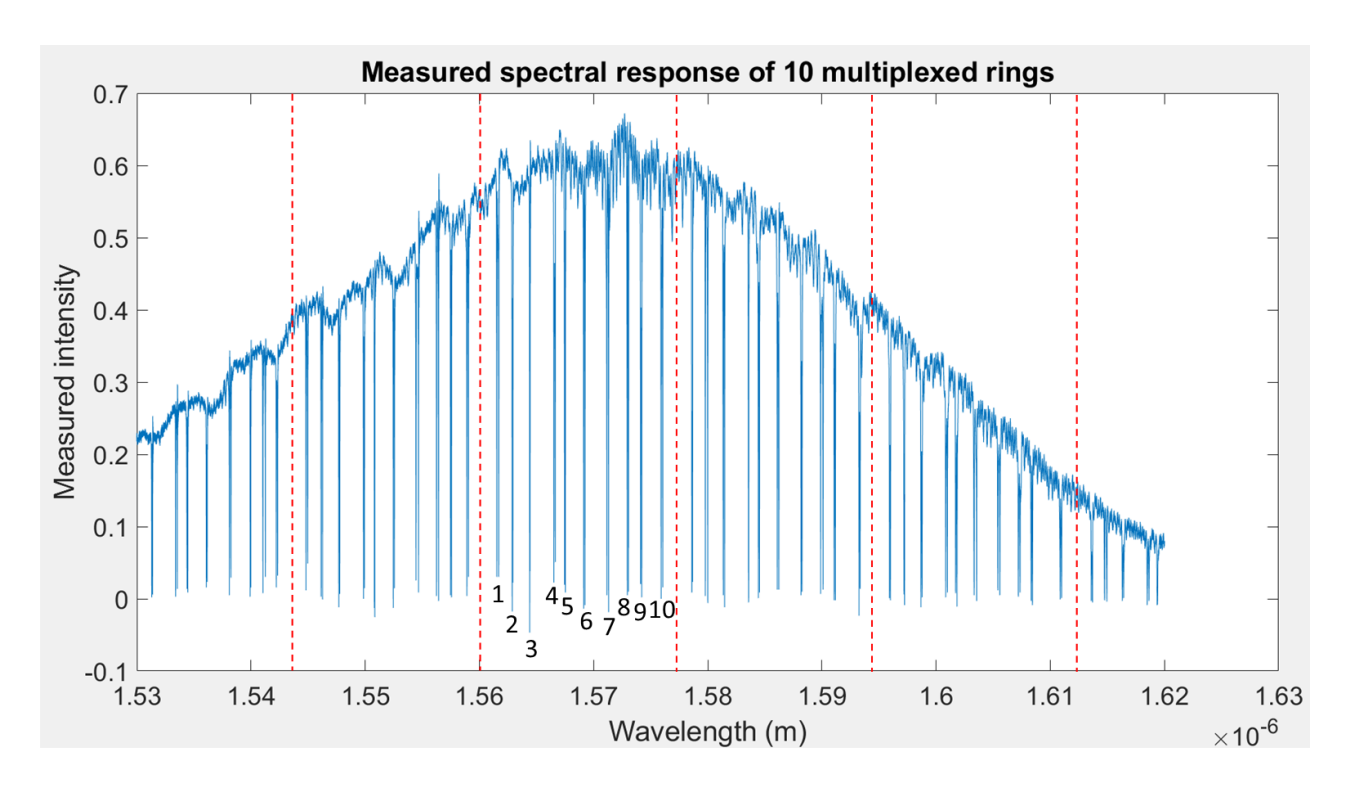


Figure 6.1: Spectral response of 10 multiplexed rings. Red dotted lines represent the FSR boundary. Although it cannot be determined from the spectral response, it has been assumed that the resonances numbers 1 to 10 represent rings with radius of $5.00 \,\mu m$ to $5.09 \,\mu m$.

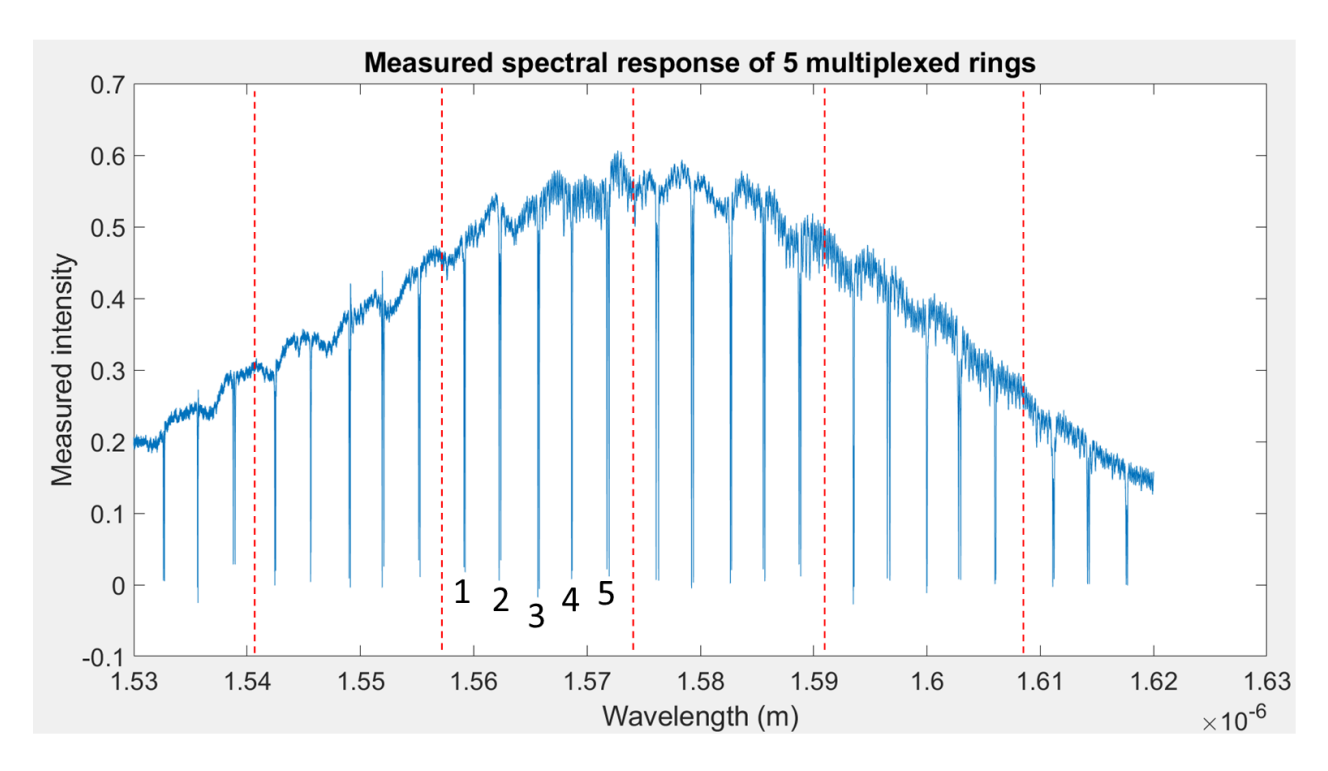


Figure 6.2: Spectral response of 5 multiplexed rings. Red dotted lines represent the FSR boundary. Although it cannot be determined from the spectral response, it has been assumed that the resonances numbers 1 to 5 represent rings with radius of $5.00 \, \mu m$ to $5.08 \, \mu m$.

The goal of this study is to estimate the potential die-scale width variation by analyzing the measured data. By using RectWG for determining n_{eff} and n_g as well as Equation 3.4, waveguide widths and heights that result in an analytically calculated resonance spectrum that results in the most accurate match with the

measurement can be obtained. The results of both measurements are shown in Table 6.1.

Ding no ding (width-thickness (nm)	width-thickness (nm)
Ring radius (μm)	10 Rings	5 Rings
5.00	410.5×202.5	411.9×200.1
5.01	410.4×202.5	N/A
5.02	413.5×200.3	412.0×200.2
5.03	412.3×201.6	N/A
5.04	412.6×201.1	413.0×199.8
5.05	411.6×202	N/A
5.06	411.3×202.6	412.7×200.1
5.07	411.2×202.9	N/A
5.08	410.2×203.5	413.1×200
5.09	424.3×203.4	N/A
Average	202.24	200.04
thickness (nm)	404.4 4	200.04

Table 6.1: Varying width and thickness of waveguide resulting in resonance spectrum that matches the measured data the best using RectWG. Width and height step size is 0.1 nm

It can be seen from Table 6.1 that both the width and thickness is much smaller than the standard 450x220 nm dimensions, which suggests the presence of wafer-scale nonuniformity as explained in section 6.1. Since the thickness is considered to be constant at the die-scale, new iterations are performed with varying widths and a fixed thickness valued at the average from Table 6.1.

Ring radius (μm)	width-thickness (nm)	width-thickness (nm)
$\frac{\text{ning radius }(\mu m)}{ }$	10 Rings	5 Rings
5.00	410.9×202.24	412.0×200.04
5.01	410.7×202.24	N/A
5.02	410.8×202.24	412.2×200.04
5.03	411.4×202.24	N/A
5.04	411.0×202.24	412.7×200.04
5.05	411.3×202.24	N/A
5.06	411.8×202.24	412.8×200.04
5.07	412.1×202.24	N/A
5.08	411.9×202.24	413.1×200.04
5.09	426.0×202.24	N/A
Average	411.32×202.24	412.56×200.04

Table 6.2: Varying widths and a constant thickness that results in resonance spectrum that matches the measured data the best using RectWG. Width and height step size is $0.1 \, nm$

The average width and thickness from Table 6.2 are considered to be the undeviated dimensions at the die-scale. In other words, the difference between the average and the other widths from Table 6.2 is then assumed to be a die-scale width deviation. In Figure 6.3 and Figure 6.4, a comparison can be made between the average (undeviated) dimensions and approximated (deviated) dimensions of Table 6.2 for the 5 rings measurement.

It can also be seen in Table 6.2 for the 10 rings measurement that the width of the ring resonator with a radius of $5.09 \,\mu m$ deviates substantially relatively to the other rings. This is considered to be an anomaly, which is why the average width does not take into account the width of this ring resonator. In that case, the root-mean-square error of the 10 and 5 rings measurements are $\Delta w = 0.485 \, nm$ and $\Delta w = 0.403 \, nm$ respectively, both of which are the standard deviation (1σ) . These results are close to the experimental value observed by Horikawa et al. [96].

Applying the standard width deviation of $0.485\,nm$ to the average cross-section of 411.32x202.24 (from the 10 rings measurement) with e.g. $R=5.05\,\mu m$, then the resonance wavelength shift is around $\Delta\lambda=\pm0.65\,nm$. For 3σ width deviation, the resonance wavelength shift becomes also around three times larger. The same thing can be done for the 5 rings measurements. Taking the standard width deviation of $\Delta w=0.403\,nm$ and add or substract it to/from the average cross-section of 412.56x200.04 for e.g. $R=5.02\,\mu m$, then the resonance shifts by around $\Delta\lambda=\pm0.5\,nm$ (1 σ width deviation) or $\Delta\lambda=\pm1.5\,nm$ (3 σ width deviation). Selvaraja et al. [97]

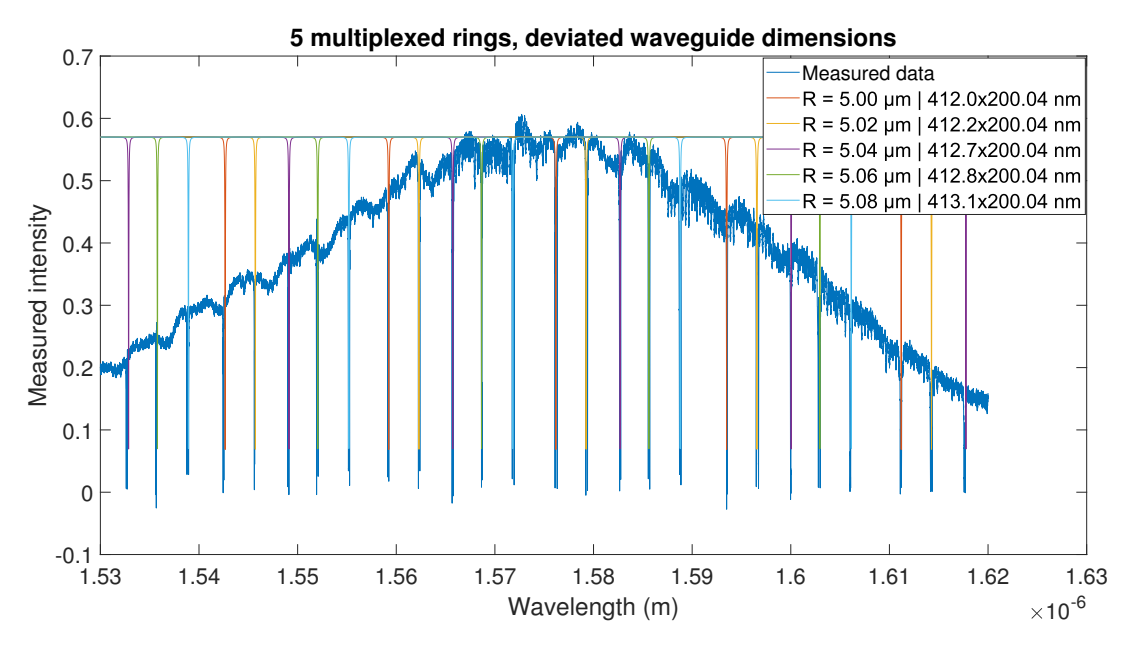


Figure 6.3: Spectral response of 5 multiplexed rings with approximated waveguide cross-sectional dimensions for each ring. Note that the approximated waveguide dimensions result resonance wavelengths that matches the ones of the measured data.

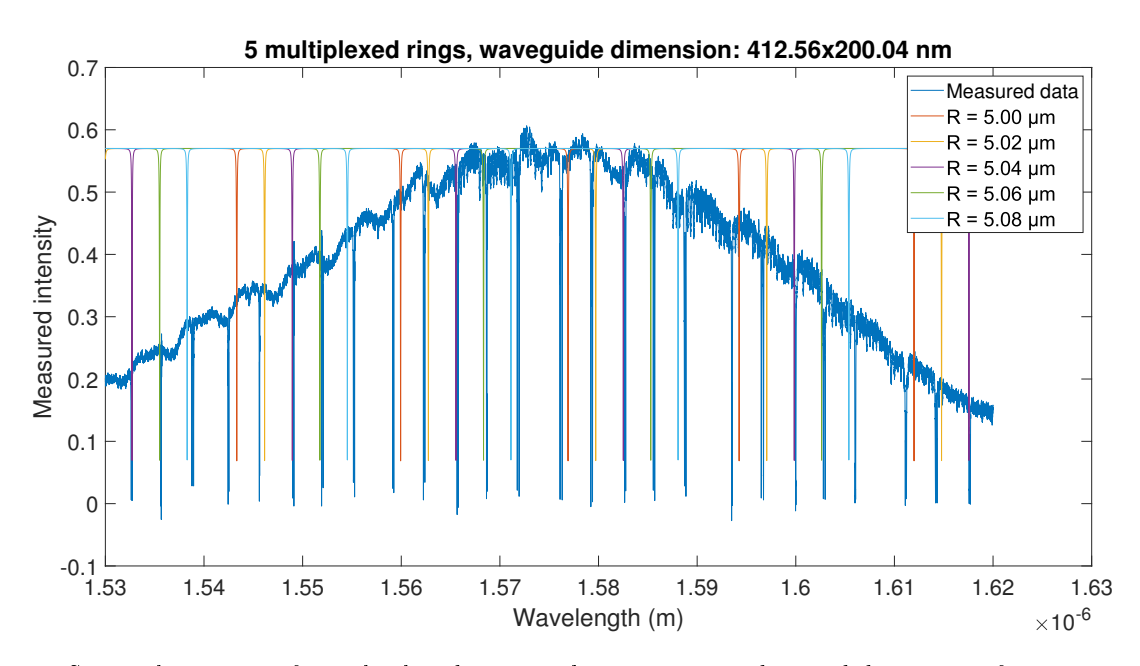


Figure 6.4: Spectral response of 5 multiplexed rings with an average undeviated dimension of $412.45x200.04\,nm$ for each ring. The difference between the resonance wavelengths of the approximation and the measured data illustrates the spectral deviation resulting from die-scale fabrication errors

show a maximum die-scale width deviation of $\Delta w = 0.6\,nm$ for a $\lambda = 193\,nm$ process. This indicates that the $\lambda = 248\,nm$ process from Cornerstone results in a die-scale width deviation that is at least three times larger than the one from $\lambda = 193\,nm$ process.

A similar analysis is also performed with a fixed waveguide width and varying thicknesses instead. The fixed widths of $411.32 \, nm$ and $412.56 \, nm$ (which are the averages from Table 6.2) are taken for the analysis of 10 and 5 rings measurements respectively. The respective waveguide thicknesses that result in matching resonance peaks are shown in Table 6.3.

Ring radius (μm)	width-thickness (nm)	width-thickness (nm)
Ting radius (µm)	10 Rings	5 Rings
5.00	411.32×201.9	412.56×199.6
5.01	411.32×201.8	N/A
5.02	411.32×201.9	412.56×199.84
5.03	411.32×202.3	N/A
5.04	411.32×202.0	412.56×200.1
5.05	411.32×202.2	N/A
5.06	411.32×202.6	412.56×200.2
5.07	411.32×202.8	N/A
5.08	411.32×202.7	412.56×200.4
5.09	411.32×213.0	N/A
Average	411.32×202.24	412.56×200.02

Table 6.3: Varying thickness and a constant width that results in resonance spectrum that matches the measured data the best using RectWG. Width and height step size is 0.1 nm

For the 10 rings measurement, the average thickness remain $202.24\,nm$, resulting in a thickness deviation of roughly $\Delta h = \pm 0.3563\,nm$ (1σ) and $\Delta h = \pm 1.0688\,nm$ (3σ) without including the thickness $R = 5.09\,\mu m$ due to its large thickness anomaly (similar to the width analysis). This thickness deviation results in resonance wavelength shifts for $R = 5.05\,\mu m$ of around $\Delta \lambda = \pm 0.60\,nm$ (1σ thickness deviation) and $\Delta \lambda = \pm 1.85\,nm$ (3σ thickness deviation). As for the 5 rings measurement, the average thickness is $200.02\,nm$. This results in a a thickness deviation of approximately $\Delta h = \pm 0.2857\,nm$ (1σ) and $\Delta h = \pm 0.8570\,nm$ (3σ). For $R = 5.02\,\mu m$, this means the resonance wavelength shift is around $\Delta \lambda = \pm 0.5\,nm$ and $\Delta \lambda = \pm 1.5\,nm$ respectively.

It can be observed that the standard thickness deviations of $\Delta h = \pm 0.2857 \, nm$ to $\Delta h = \pm 0.3563 \, nm$ result in a resonance wavelength shifts that are similar to the values observed for standard width deviations of $\Delta w = \pm 0.403 \, nm$ to $\Delta w = \pm 0.485 \, nm$. This indicates that both the width and thickness variations can influence the resonance wavelength shift. From now on in this thesis, only the standard width deviations will be used as a simplified description of the die-scall fabrication error induced resonance wavelength shift. However in practice, this spectral deviation can potentially be caused by a combination of both width and thickness errors.

6.2.2 Probability of Resonance Peak Overlap

In subsection 6.2.1, it has been shown that there is a linear correlation between die-scale width deviation of the waveguide and the resonance wavelength shift as a result of it. For this reason, the resonance wavelength uncertainty due to die-scale width nonuniformity can be described by a normal distribution with a standard deviation of e.g. $\Delta \lambda = 0.65 \, nm$ (based on the 10 rings measurement from subsection 6.2.1).

With this information, the probability of an arbitrary number of resonance peak overlap can be predicted using Monte-Carlo simulations that are different from the ones of subsection 4.2.3. This is done by first placing multiple points next to each other as shown in Figure 6.5, representing resonance peaks of different ring resonators in a spectrum. Two extra points are then added at the beginning and the end of the resonance points spectrum, representing one a mode order higher and lower of the first and last existing resonance point respectively (see Figure 6.5). Afterwards, each point individually deviates horizontally based on the normal distribution with the standard deviation of e.g. $0.65\,nm$ determined in subsection 6.2.1. Then the number of resonance peak overlaps can be counted by checking the seperation distance between each point pair. The definition of resonance peak overlap is subjective. For this analysis, the definition is chosen to be the minimum distance required between two peaks in order for both to be individually curve-fittable using the steps described in subsection 4.2.2. Curve-fits have been carried out for the 10 rings measurement in section 6.3. It was observed that resonance peaks with a seperation distance of approximately $> 3 \cdot \Delta \lambda_{FWHM}$ were individually curve-fittable. Reducing the seperation distance to below $3 \cdot \Delta \lambda_{FWHM}$ causes one resonance peak to interfere with the curve-fitting process of another resonance peak, resulting in less accurate curve-fit.

This entire process needs to be repeated 10000 times (from explorative calculations, more iterations do not give noticable different results) in order to get the overlap statistics. The 10 rings measurement is used as an example here. The bus waveguide contains 10 ring resonators. The resonance seperation distance without die-scale width deviations is $1.4 \, nm$, the FSR is $17 \, nm$ and the FWHM of $25 \, pm$ is taken (which is a rough average of the Q-factors from Table 6.4).

Taking these and the aforementioned information result in the overlap statistics for the 10 rings measurement as shown in Figure 6.6. It can be seen that the probability of zero overlap is 82.56% and 16.13% for a single

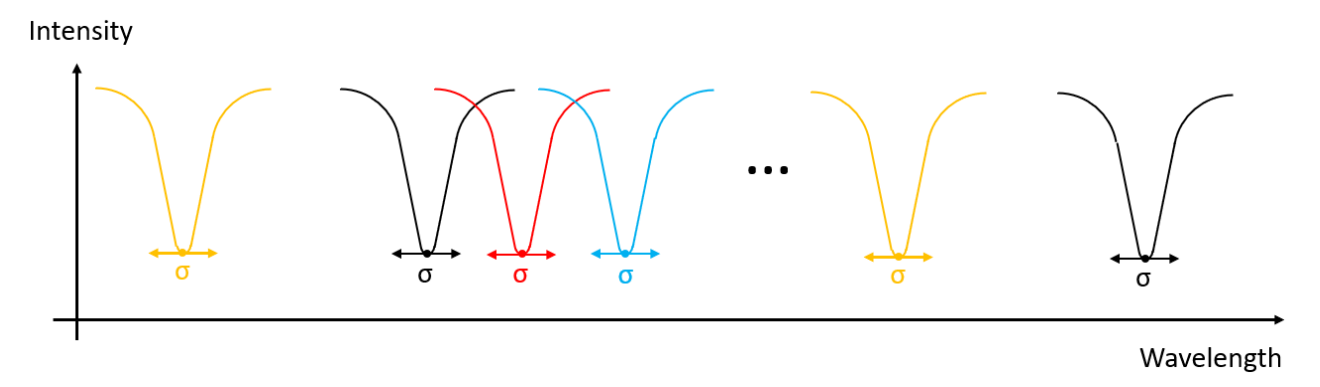


Figure 6.5: Schematic overview of resonance peak overlap analysis principle. The seperation distance between each resonance peak is initially the same. Afterwards, spectral deviation caused by die-scale fabrication error is applied individually to each of the resonance peak. The spectral deviation probability is modeled using a normal distribution with a standard deviation σ defined in subsection 6.2.1. The resonance points representing the higher and lower mode order of the first (black line) and last (yellow line) respectively are added as well.

overlap (with $\Delta\lambda_{FWHM}=25\,pm$). This indicates that this device configuration will most probably not result in a single resonance peak overlap, but it still not unlikely for that to happen. It can also be seen in Figure 6.6 that an increase of the FWHM while keeping the remaining simulations parameters the same results in a higher resonance peak overlap probability. For $\Delta\lambda_{FWHM}=50\,pm$ and $\Delta\lambda_{FWHM}=75\,pm$, the probability of zero resonance peak overlap decreases to 67.12% and 54.07% respectively.

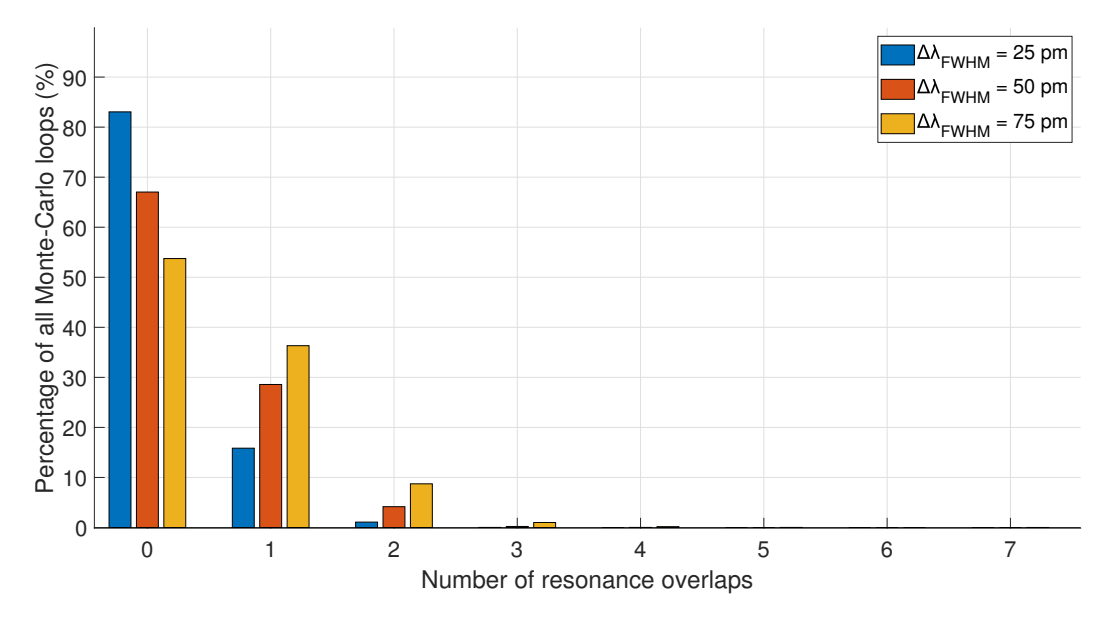


Figure 6.6: Overlap statistics of the 10 rings measurement for different $\Delta \lambda_{FWHM}$ of the resonance peaks.

In this way, tests can be carried out to determine the likelihood of resonance peaks overlapping one another for an arbitrary amount of ring resonators on a single bus waveguide. For large array of sensors for distributed force sensing, a certain percentage of resonance peaks that are overlapping can be considered acceptable. The determination of an acceptable overlap percentage is left as a follow-up research topic. It should be noted that this analytical model does not consider resonance splitting. This is caused by the back reflection of a certain wavelength inside the ring resonator that results in an excitement of a second mode and therefore also the appearance of a second resonance [98].

6.3 Sidewall Roughness and Absorption Loss

With RSoft, the transmission coefficient τ and the roundtrip propagation loss of a ring resonator α can be determined. The actual values of both τ and α can deviate due to fabrication nonuniformities and errors that cause the photonic integrated circuit to perform differently. In this section, both τ and α are determined from measured data of existing ring resonators and compared with the values obtained from RSoft.

From the measurements, the full width half maximum $(\Delta \lambda_{FWHM})$, free spectral range $(\Delta \lambda_{FSR})$, resonance wavelength (λ_m) and the roundtrip length (L) can be determined. The group index at the resonance wavelength of interest $n_g(\lambda_m)$ can be determined by rewriting Equation 5.1 resulting in the following equation.

$$n_g(\lambda_m) = \frac{\lambda_m^2}{\Delta \lambda_{FSR} L} \tag{6.1}$$

After obtaining the group index, Equation 4.3 can be rewritten to solve for $\alpha |\tau|$.

$$(A^{2}+1) \cdot \cos\left(\frac{\Delta \lambda_{FWHM} \cdot \pi L n_{g}(\lambda_{m})}{\lambda_{m}^{2}}\right) - 2A = 0$$

$$(6.2)$$

where $A = \alpha |\tau|$. There are two solutions for A in Equation 6.2. The one that has a value of lower than 1 must be taken. In the case of critical coupling, when $\alpha = \tau$, then both α and τ can be determined by taking the square root of A. However, the ring resonator is most of the time not perfectly critically coupled, meaning $\tau \neq \alpha$. Figure 6.7 shows the extinction ratios for different τ - α combinations.

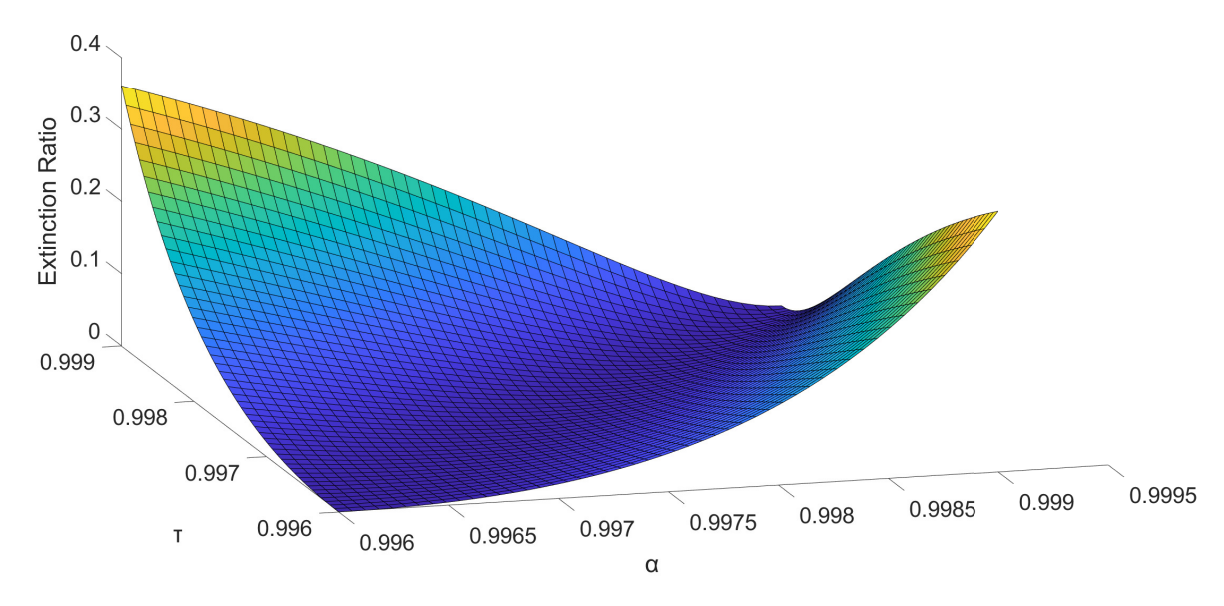


Figure 6.7: Extinction ratio for different α and τ combinations

The extinction ratio defined in Figure 6.7 is the inverse of Equation 4.14, with critical coupling corresponding to an extinction ratio of 0. The two possible τ and α combinations that corresponds to the measured extinction ratio and FWHM can be found by increasing α and decreasing τ by the same amount and vice versa and afterwards finding the combination that results in the same extinction ratio as the one found from the measurement. This process is also illustrated in Figure 6.8.

In all the measured data, the resonances of the ring resonators have been split. The two splitted resonances that partially overlap each other can be described by the sum of two seperate Lorentzian peaks. However, this makes curve-fitting much harder, since twice as many variables have to be optimized (for curve-fitting procedure, see subsection 4.2.2). Therefore, this analysis limits to measurements where the splitted resonance peaks do not overlap each other. Certain resonance peaks of the measurements discussed in section 6.2 do satisfy this requirement. Each resonance peak can be individually curve-fitted using Equation 4.9 to obtain $\Delta \lambda_{FWHM}$, λ_m and the extinction ratio, while the $\Delta \lambda_{FSR}$ can be directly determined from the measurement data (FSR values are between 16.3 nm and 17.6 nm). Subsequently, the calculation steps described earlier in this section can be applied to determine the possible τ - α combinations for each of these resonances. The results are shown in Table 6.4.

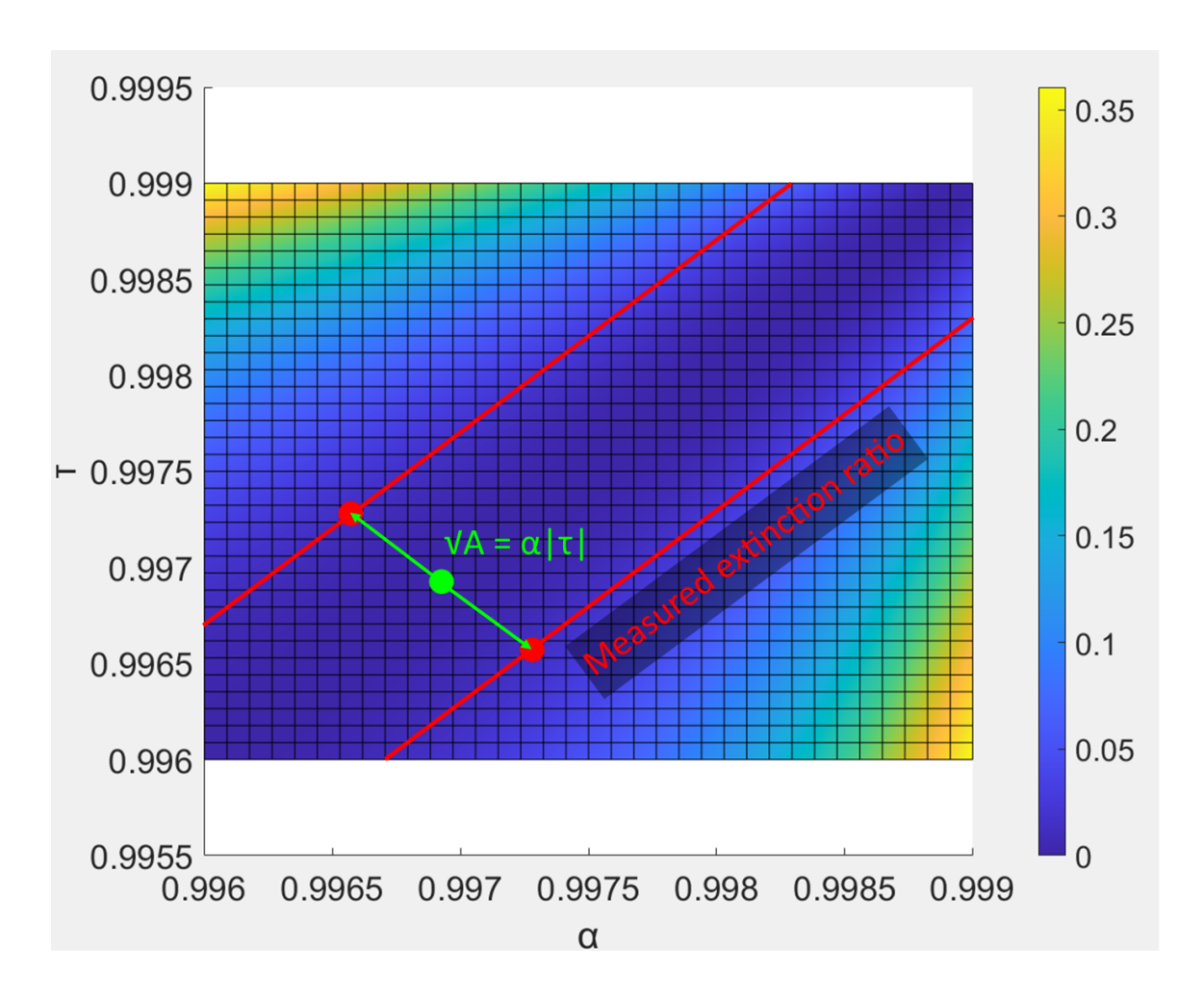


Figure 6.8: Top view of the plot from Figure 6.7. By solving Equation 6.2, the combination of τ and α at the green dot can be obtained. Afterwards, follow the green arrows until the location of the red dot has been reached, which corresponds to α - τ combinations that result in the measured extinction ratio as well as the measured FWHM.

$R(\mu m)$	Measurement	$\lambda_m (nm)$	$\Delta \lambda_{FWHM} \ (pm)$	R_{min}/T_t	$ au_{meas}$ or $lpha_{meas}$
5.08	10 rings	1541.044	19.88	0.00405/0.345	$(1) \ 0.99790, \ 0.99831$
5.06	10 Tings	1541.257	17.79	0.0222/0.3409	$(2) \ 0.99785, \ 0.99872$
F 07	10 rings	1556.253	20.73	0.0/0.534	$(1) \ 0.99853$
5.07	10 rings	1556.425	18.37	0.0/0.5344	$(2) \ 0.99827$
5.07	10 rings	1572.953	29.12	0.019/0.641	$(1) \ 0.99684, \ 0.99777$
5.07	10 Tings	1573.059	31.14	0.0/0.641	$(2) \ 0.99713$
5.08	5 rings	1538.780	19.53	0.0245/0.289	$(1) \ 0.99758, \ 0.99867$
5.00	5 rings	1538.946	28.05	0.0266/0.292	$(2) \ 0.99634, \ 0.99827$
5.08	5 ringa	1571.761	29.85	0.0293/0.539	$(1) \ 0.99649, \ 0.99781$
5.06	5 rings	1571.947	27.57	0.0266/0.575	$(2) \ 0.99689, \ 0.99799$
5.06	5 ringa	1585.552	30.58	0.0/0.537	$(1) \ 0.99722$
5.00	5 rings	1585.696	36.84	0.0/0.543	(2) 0.99666
5.02	5 ringa	1596.503	34.63	0.005666/0.425	$(1) \ 0.99657, \ 0.99728$
3.02	5 rings	1596.723	40.74	0.0/0.419	$(2) \ 0.99637$

Table 6.4: Variables obtained from measured spectral responses.

The last column of Table 6.4 represents the possible τ and α values that result in the extinction ratio, FWHM and resonance wavelengths as shown in the same table. For example in the first row of Table 6.4, τ and α are either 0.9979 and 0.99831 respectively in the case of overcoupling or vice versa in the case of undercoupling (corresponding to the first resonance of the resonance split).

Afterwards, τ and α can be determined using RSoft. The CAD model of the waveguide consists of cross-sections with a refractive index of 3.46 and dimensions taken from the ones shown in Table 6.2. The refractive index of the BOX layer and the cover is 1.444 and 1 respectively, representing SiO_2 and air. Finally, a 180 nm thick SiO_2 layer is put on top of the waveguide, which is the hard mask used for etching the die. This layer has not been removed at the time of measuring. Finally, the average resonance wavelength of the resonance split is taken. With this model as well as the relevant simulation settings and the post-processing steps discussed in chapter 5, τ and α can be obtained. The results are shown in Table 6.5.

Simulation number	R (μm)	Measurement	Wavelength (nm)	$\alpha_{rad} (dB)$	$\alpha_{swa} \ (dB/cm)$
1	5.08	10 rings	1541.150	$6.91 \cdot 10^{-7}$	(1) 5.73, 4.61 (2) 5.86, 3.47
2	5.07	10 rings	1556.339	$1.98 \cdot 10^{-7}$	(1) 5.31 (2) 4.74
3	5.07	10 rings	1573.406	$6.92 \cdot 10^{-7}$	(1) 8.64, 6.10 (2) 7.83
4	5.08	5 rings	1538.628	$7.39 \cdot 10^{-7}$	(1) 6.59, 3.61 (2) 9.97, 4.72
5	5.08	5 rings	1571.854	$2.08 \cdot 10^{-8}$	(1) 9, 57, 5.95 (2) 8.47, 5.47
6	5.06	5 rings	1585.624	$2.21 \cdot 10^{-6}$	(1) 7.61 (2) 9.15
7	5.02	5 rings	1596.613	$5.54 \cdot 10^{-6}$	(1) 9.46, 7.50 (2) 10.02

Table 6.5: Roundtrip loss results obtained with RSoft FemSIM. Note that the wavelength in the third column is the approximate average between the two resonances of the resonance split.

Simulation number	$ au_{RSoft}$	$\sqrt{1-\kappa_{RSoft}^2}$	Intensity loss $(1 - \tau_{RSoft}^2 - \kappa_{RSoft}^2)$	$ au_{loss}(dB)$
1	0.99334	0.99350	$3.11\cdot 10^{-4}$	(1) 0.0397, 0.0433 (2) 0.0393, 0.0469
2	0.99193	0.99212	$3.58\cdot10^{-4}$	(1) 0.0534 (2) 0.0553
3	0.99000	0.99020	$3.94\cdot10^{-4}$	(1) 0.0598, 0.0679 (2) 0.0623
4	0.99327	0.99345	$3.60\cdot10^{-4}$	(1) 0.0377, 0.0472 (2) 0.0269, 0.0436
5	0.98761	0.98992	$4.61\cdot10^{-4}$	(1) 0.0595, 0.0710 (2) 0.0630, 0.0726
6	0.98766	0.98796	$5.89\cdot10^{-4}$	(1) 0.0837 (2) 0.0788
7	0.98580	0.98605	$4.92\cdot10^{-4}$	(1) 0.0944, 0.1009 (2) 0.0926

Table 6.6: Coupling results obtained from the coupling simulations in FullWAVE.

It can be seen in Table 6.5 that α calculated using RSoft's FemSIM is much higher than the measured values, due to the fact that RSoft simulations only considers radiation losses. Therefore, by subtracting the radiation loss from the total loss determined with the measurements, the sidewall scattering and absorption loss α_{swa} (in dB/cm) can be obtained.

$$\alpha_{swa} [dB] = \alpha_{meas} [dB] - \alpha_{rad} [dB]$$
(6.3)

The results of α_{swa} are shown in the last column of Table 6.5. The sidewall scattering and absorption loss ranges from around $3\,dB/cm$ to $10\,dB/cm$ for a waveguide bend with a $5\,\mu m$ radius at different resonance wavelenghts. This is on average higher than what Cornerstone has specified for straight waveguides, but lower than another

research [99]. Therefore determining α , extra propagation loss should also be taken into account besides the radiation losses simulated with RSoft.

In Table 6.6, the coupling results from FDTD simulations are shown. It can be observed that the simulated transmission coefficient is lower than the ones obtained from the measurements in Table 6.4. The reason for this is that the simulations do not consider sidewall roughness, making it less difficult to couple mode fields from one to another waveguide. In other words, there are additional transmission losses in practice (due to optical intensity losses during coupling), which can be determined with .

$$\tau_{loss} [dB] = \tau_{RSoft} [dB] - \tau_{meas} [dB]$$
(6.4)

The results of τ_{loss} are shown in the last column of Table 6.6. The additional losses of the coupling process ranges from $\tau_{loss} = 0.027\,dB$ up to $\tau_{loss} = 0.1\,dB$.

It can also be determined from Table 6.6 that the intensity loss is much smaller than the κ_{RSoft}^2 (κ_{RSoft}^2 can be computed for each simulation number by taking the values of the third column (TC) of Table 6.6 and rewriting the equation $TC = \sqrt{1 - \kappa_{RSoft}^2}$ to $\kappa_{RSoft}^2 = 1 - TC^2$). As explained in section 5.4, this indicates the intensity loss can be neglected and the expression $\tau_{RSoft}^2 + \kappa_{RSoft}^2 \approx 1$ can be assumed (note that the values both τ_{RSoft} and $\sqrt{1 - \kappa_{RSoft}^2}$ are similar).

Chapter 7

Results

In this chapter, the final photonic integrated circuit design for distributed force sensing is shown. It starts by analyzing a medium-sized sensor design, which is a ring resonator with a radius of $5 \mu m$. Afterwards, smaller ring resonator designs are shown that satisfy the design requirements as mentioned in section 1.3. Subsequently, the entire chip design is shown, representing the photonic integrated circuit for distributed force sensing. Finally, the interrogation performance of the photonic integrated circuit is determined using a methodology described in subsection 4.2.2.

7.1 Medium-Sized Sensor Design

The medium-sized sensor design consists of a ring resonator with $R=5\,\mu m$, a cross-section of $450x220\,nm$ and PDMS cladding (remaining device specifications are found in section 5.1). A waveguide height of $220\,nm$ is chosen, since this is also the thickness of the top silicon layer of the SOI-wafer Cornerstone uses for fabricating photonic integrated circuits [93], while a waveguide width of $450\,nm$ is a typical dimension for guiding a single mode [14]. This sensor design is intended to test out both the temperature compensation using a reference ring as well as the multiplexibility when considering fabrication errors. The reason for this is that the spectral characteristics of silicon ring resonators with a $5\,\mu m$ radius are already well known by W-Lab. The design is presented by showing simulation results of the intrinsic limit-of-detection, coupling gap, temperature drift and the spectral devations due to fabrication errors.

7.1.1 Intrinstic Limit-of-Detection

The intrinsic limit-of-detection (as explained in section 4.1) can be calculated by determining both α and the sensitivity using the steps described in section 5.2 and section 5.3 respectively. With α , assuming $\tau = \alpha$ as well as $ng(\lambda_m)$ with the resonance order m that is the closest to the central wavelength of $\lambda_c = 1550 \, nm$, the FWHM can be determined using Equation 4.3.

Starting with determining α , both n_{eff} and n_g at different wavelengths and a cladding refractive index of $n_{clad}=1.3892$ from the bend loss dispersion simulations are shown in Figure 7.1 and Figure 7.2. The effective index at the central wavlength of $1550\,nm$ is $n_{eff}(\lambda_c)=2.34215+i\cdot 1.62335\cdot 10^{-6}$. This results in a radiation loss of $\alpha_{rad}=0.99991174$ or $0.244\,dB/cm$. Note that the extinction coefficient of the PDMS cladding is defined as mentioned in subsection 5.2.2. This means that α_{rad} also contains absorption losses in PDMS. As an approximation for this study, $\alpha_{rad}=0.99991174$ is assumed for all wavelengths, not just the central wavelength. The sidewall roughness and absorption induced propagation loss (α_{swa}) is varied from $3\,dB/cm$ to $10\,dB/cm$ with an increment of $1\,dB/cm$. The total roundtrip loss α for different α_{swa} is shown in Figure 7.3. It can be seen that α ranges from 0.99883 to 0.9963 for $\alpha_{swa}=3\,dB/cm$ to $\alpha_{swa}=10\,dB/cm$.

From the dispersion simulation, the group index n_g at the central wavelength is $n_g(\lambda_c)=4.17768$. With these variables and using Equation 3.2, the resonance order m that is the closest to the central wavelength is m=47, which corresponds to a resonance wavelength of $\lambda_{m=47}=1558.68\,nm$. The group index at this resonance wavelength according to the dispersion simulation is $n_g(\lambda_{m=47})=4.18172$. These values can be substituted in Equation 4.4 to calculate the Q-factor in the case of critical coupling (therefore $\alpha=\tau$). In Figure 7.5, the Q-factors at different sidewall roughness and absorption losses are shown.

The effective index with a cladding refractive index of $n_{clad}=1.39$ instead of $n_{clad}=1.3892$ is $n_{eff}(\lambda_c,n_{clad}=1.39)=2.34231$. Applying Equation 5.11 results in $\frac{\Delta n_{eff}}{\Delta n_{clad}}$ of 0.20625. The sensitivity of the ring resonator can be

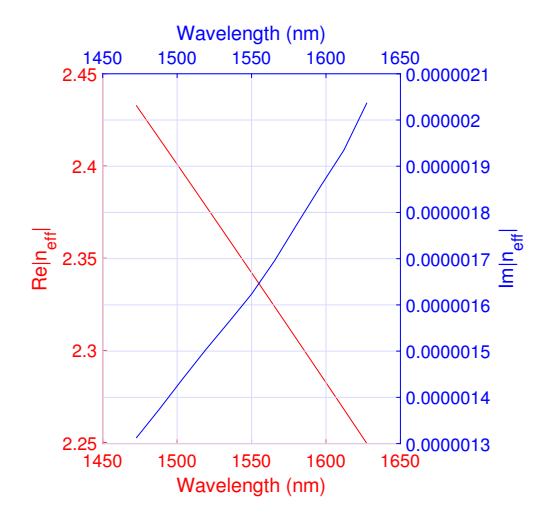


Figure 7.1: Complex refractive index at different wavelengths (radiation loss only)

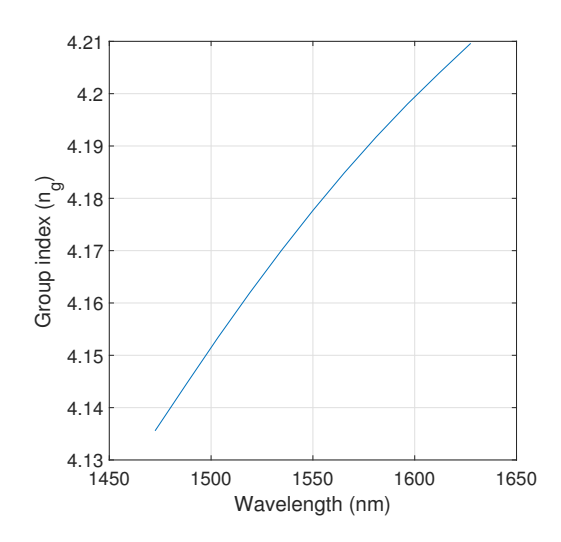
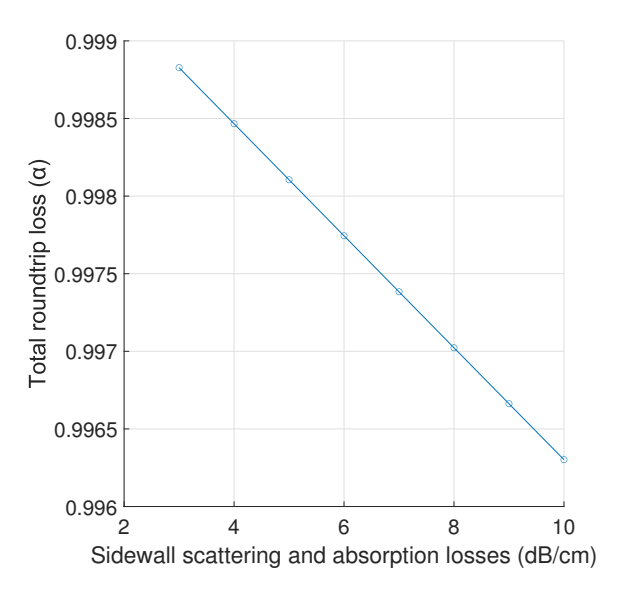


Figure 7.2: Group index at different wavelengths



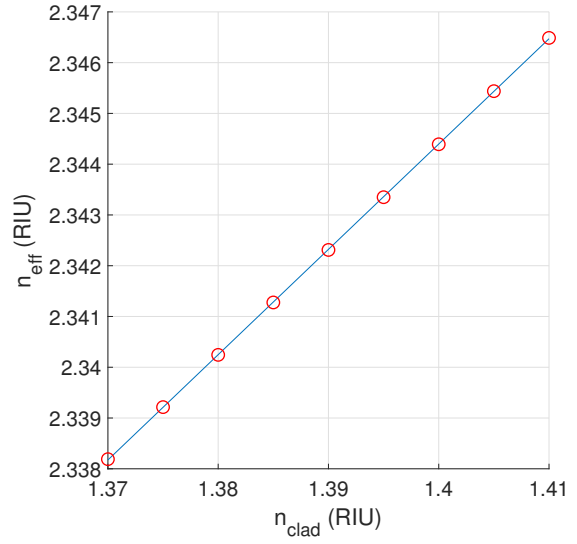


Figure 7.3: Different total roundtrip losses (α) for Figure 7.4: Effective refractive index data points caldifferent sidewall roughness and absorption induced culated with RSoft at different cladding refractive inpropagation losses.

dices (red) and a corresponding curve-fit (blue)

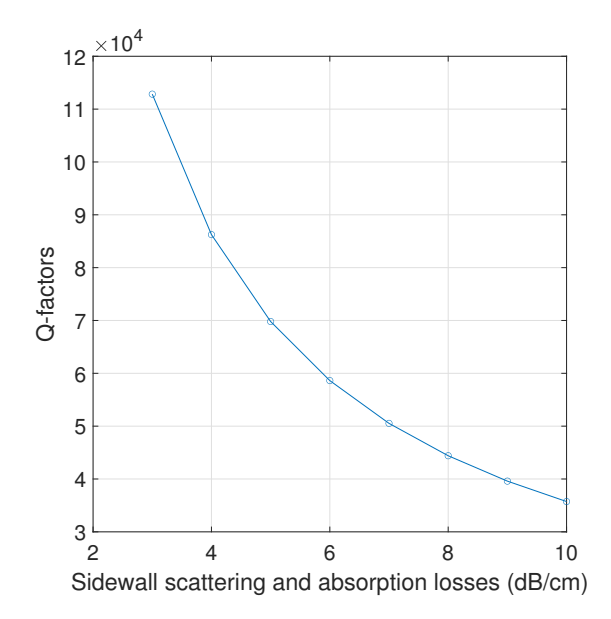
calculated using Equation 5.10. With the variables determined using RSoft, this results in $S = 76.52 \, nm/RIU$. Figure 7.4 shows that the effective refractive index is nearly linearly correlated to the cladding refractive index.

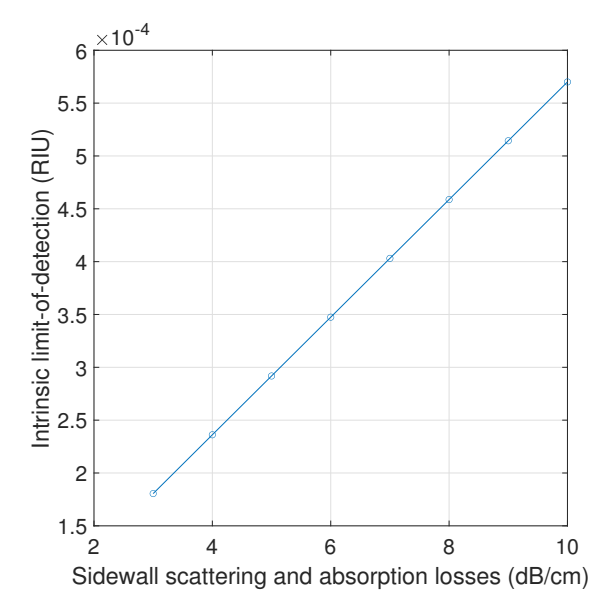
A curve that corresponds to a second-order polynomial equation is fitted in the data points as shown in Figure 7.4. The curve-fit errors of all these data points are ranging from around $4 \cdot 10^{-8}$ to roughly $4 \cdot 10^{-8}$. The first-order derivative (corresponding to $\frac{\partial n_{eff}}{\partial n_{clad}}$ from Equation 5.10) at the PDMS refractive index of $n_{clad} = 1.3892$ is 0.2073. This results in $S = 76.96 \, nm/RIU$ when substituting $\frac{\partial n_{eff}}{\partial n_{clad}} = 0.2073$ in Equation 5.10 with $n_g(\lambda_c)$ is still 4.17768. This is close to the previously calculated value of $S = 76.52 \, nm/RIU$.

Finally, the intrinsic limit-of-detection (which can be calculated using Equation 4.2) at different sidewall roughness and absorption losses are shown in Figure 7.6.

7.1.2 Temperature Drift

A 3D-plot showing the required width for the reference ring resonator for varying cladding refractive indices and thermo-optic coefficients in order for its temperature sensitivity to match the one of the force sensing reference sensor (cladded in PDMS) with the same waveguide height but a standard waveguide width of $450 \, nm$ is shown





with resonance order m = 47.

Figure 7.5: Q-factors versus propagation losses α_{swa} Figure 7.6: Intrinsic limit-of-detections versus propagation losses α_{swa} with resonance order m = 47.

in Figure 7.7. RectWG is used here for calculating the mode fields. The range of the cladding refractive indices and the thermo-optic coefficients is taken from the provided specifications of the commercial hybrid-polymer Ormocer [92]. If the refractive index and the thermo-optic coefficient of the reference cladding is for example 1.53 and $-2 \cdot 10^{-4} \, K^{-1}$ respectively (arbitrarily chosen), then the required reference waveguide width should be $360 \, nm$ according to RectWG.

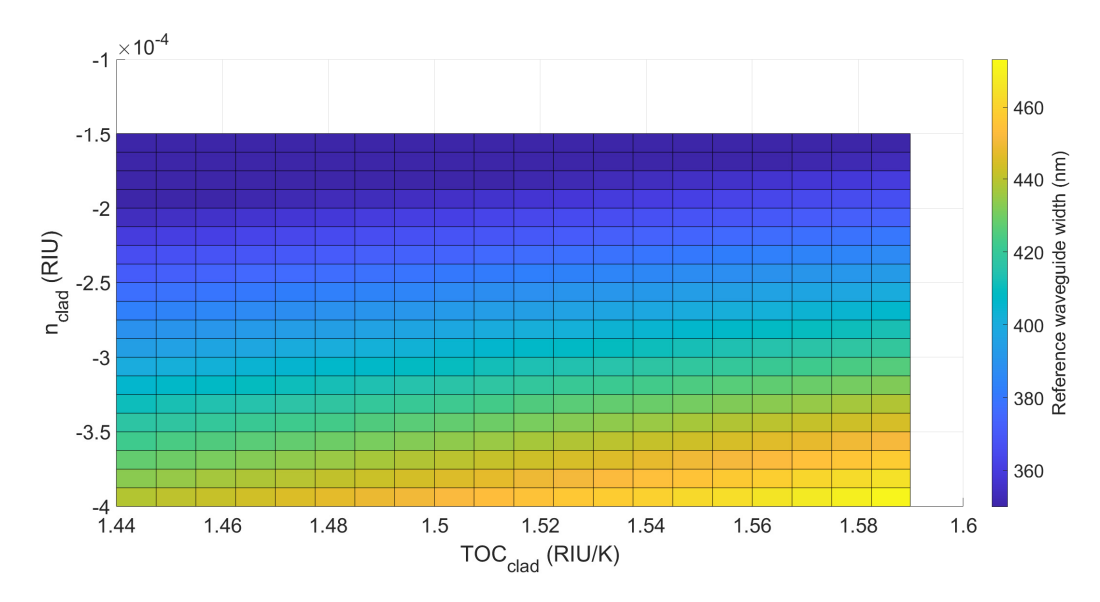


Figure 7.7: Different Ormocer properties versus required width in order for the temperature sensitivity of the reference sensor to be equal to the one of the force sensor, Note that the reference waveguide width does not go below the minimum of $350 \, nm$ specified by Cornerstone. RectWG is used for calculating mode fields.

A similar study is performed with RSoft with these example optical properties. $\frac{\partial n_{eff}}{\partial T}$ of both the force sensor as well as the reference sensors at the central wavelength obtained from RSoft is shown in Figure 7.8. By line-fitting the data points in Figure 7.8a using a first-order polynomial equation, $\frac{\partial n_{eff}}{\partial T}$ of the force sensor is equal to around $1.10 \cdot 10^{-4} RIU/K$ (see Figure 7.8a). Considering the central wavelength of $\lambda_c = 1550 \, nm$ and a group index of $n_a(\lambda_c) = 4.17768$ obtained from the dispersion simulation, the temperature sensitivity of the force sensor is around $40.84 \, pm/K$. The temperature sensitivity of the reference sensor shown in Figure 7.8b corresponds to a waveguide width equal to the one of the force sensor, which is 450nm. This has resulted in

 $\frac{\partial n_{eff}}{\partial T}=1.51\cdot 10^{-4}\,RIU/K$. With a corresponding groupd index $n_g(\lambda_c)=4.09385$ obtained from the dispersion simulation, the temperature sensitivity of the reference sensor is $57.02\,pm/K$. This is different compared to the one of the force sensor, resulting in a large minimum detectable wavelength shift as explained in section 5.5. To equalize the temperature sensitivity of both sensor types, the reference waveguide width must be decreased to $370\,nm$. This results in $\frac{\partial n_{eff}}{\partial T}=1.10\cdot 10^{-4}\,RIU/K$ (see Figure 7.8c), $n_g(\lambda_c)=4.18615$ and a temperature sensitivity of $40.63\,pm/K$. The curve-fitting errors of all the data points from Figure 7.8 are ranging from roughly $1.9\cdot 10^{-7}$ to $2.2\cdot 10^{-6}$.

When using Equation 5.18 to determine $\frac{\Delta n_{eff}}{\Delta T}$ with e.g. $T_1 = -10\,K$ and $T_2 = +10\,K$ instead of determining the slope of the fitted line, the temperature sensitivities of the force, reference and the adjusted width reference sensor are $40.77\,pm/K$, $57.01\,pm/K$ and $40.91\,pm/K$ respectively. This shows both methods of determining $\frac{\Delta n_{eff}}{\Delta T}$ will give similar results.

The required width for temperature sensitivity equalization is $10 \, nm$ larger compared to the result obtained from RectWG in Figure 7.7. The required waveguide width of $370 \, nm$ obtained with RSoft is taken as the final result of the design. The 3D-plot of Figure 7.7 obtained with RectWG is considered to be an intermediate result, which can be used as an input data for RSoft to calculate the required waveuguide width numerically.

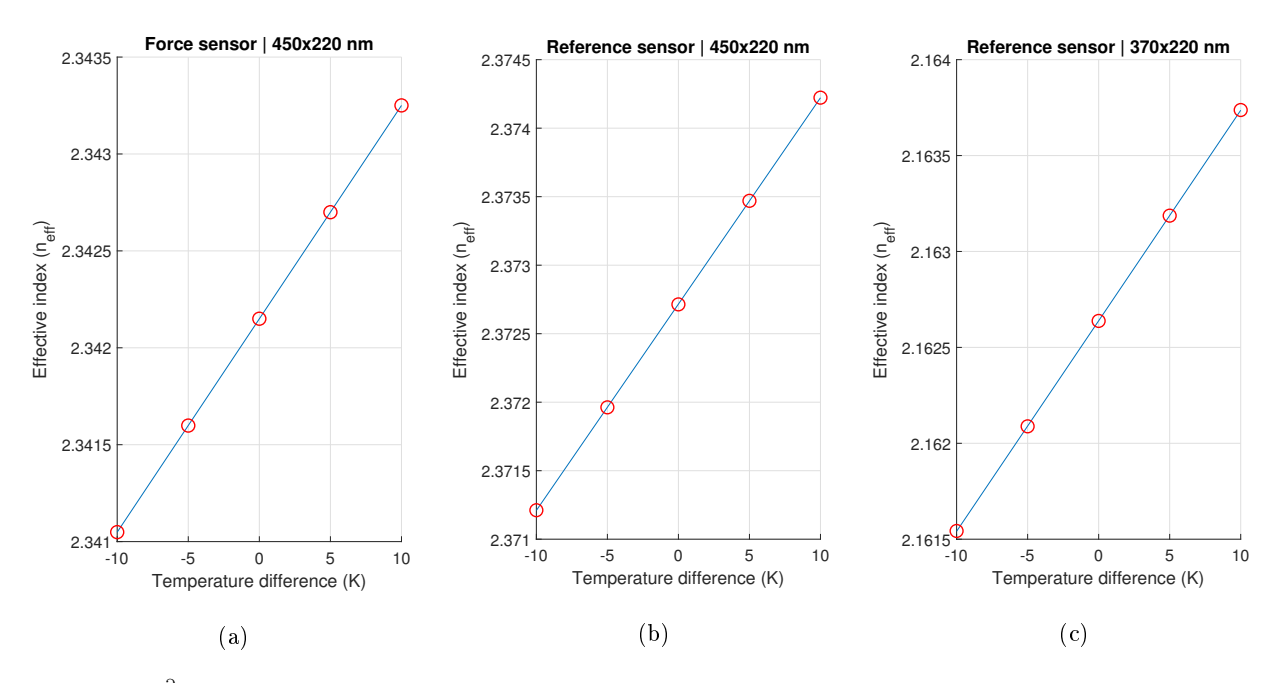


Figure 7.8: $\frac{\partial n_{eff}}{\partial T}$ at $\lambda = 1550 \, nm$ for (a) force sensor, (b) reference sensor with the same cross-sectional dimensions as the force sensor and (c) reference sensor with adjusted waveguide width to equalize temperature sensitivity with the one of the force sensor

The temperature sensitivities of both the force and reference sensors remain roughly the same at different wavelengths as shown in Figure 7.9. The wavelengths of $1580\,nm$ and $1610\,nm$ have been simulated as well besides the central wavelength. This shows that the temperature sensitivity of the force sensor is constantly higher at all wavelengths. Since the FSR of $R=5\,\mu m$ ring resonators is around $18.5\,nm$ (calculated with Equation 5.1 using $\lambda_{m=47}=1558.68\,nm$ and $n_g(\lambda_{m=47})=4.18172$), the temperature sensitivity errors between the reference sensor and all multiplexed force sensors due to the wavelength difference will remain below $2.5\,pm/K$. As an example, according to Figure 7.9, the temperature sensitivity of the force sensor at $\lambda=1570\,nm$ and the reference sensor at $\lambda=1570\,nm+18.5\,nm$ is $39.23\,pm/K$ and $37.56\,pm/K$ respectively. However, for smaller ring sizes which have increased FSR, multiple reference sensors can be considered to minimize the temperature sensitivity error caused by wavelength differences over the entire FSR.

Besides the group index of the reference sensor $(n_g(\lambda_c)=4.18615)$ as mentioned before, the complex effective index at the central wavelength calculated with FemSIM is $n_{eff}(\lambda_c)=2.16297+i\cdot 1.45959\cdot 10^{-8}$. This results in a radiation loss of $\alpha_{rad}=0.99999914$. The total roundtrip loss α decreases further to 0.9989 and 0.9964 when adding $\alpha_{swa}=3\,dB/cm$ and $\alpha_{swa}=10\,dB/cm$ from α_{rad} respectively as shown in Figure 7.10. The resonance peak that is the closest to the central wavelength according to Equation 3.4 is $\lambda=1547.08\,nm$, which corresponds to a group index of $n_g(1547.08\,nm)=4.18753$ obtained from the dispersion simulations. This results in a critical coupled Q-factor of 123003 to 36922 when considering $\alpha_{swa}=3\,dB/cm$ and $\alpha_{swa}=10\,dB/cm$ respectively.

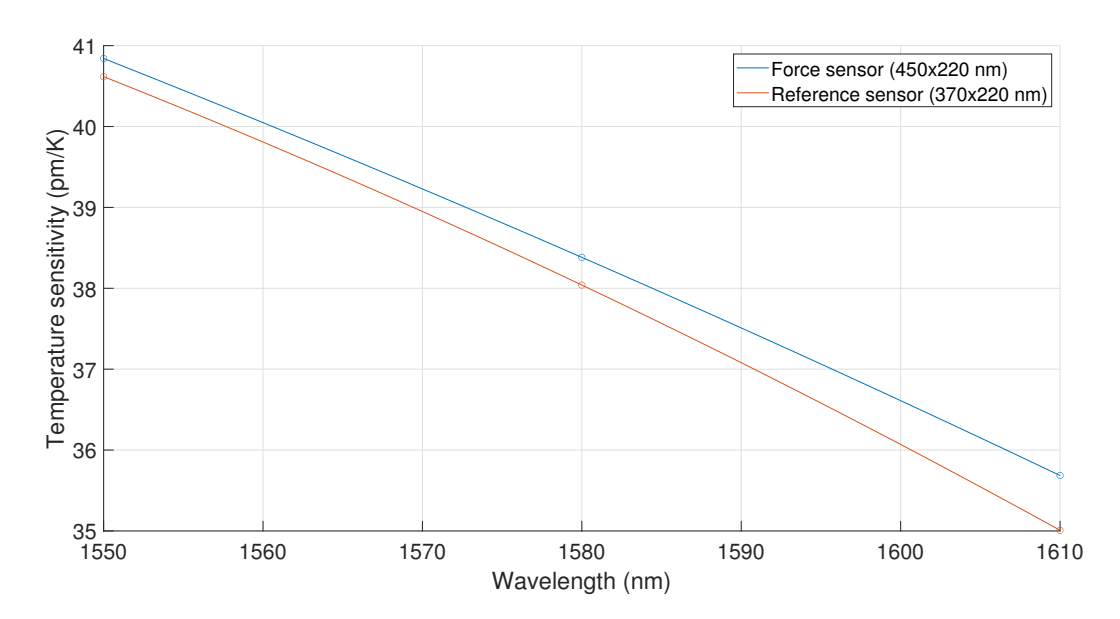


Figure 7.9: Temperature sensitivity of both the force and reference sensor at different wavelengths

These values are close to the ones of the force sensor as shown in Figure 7.11, indicating that the reference sensor and the force sensor have similar minimum detectable wavelength shifts $(\Delta \lambda_{min})$. It should be noted that the extinction coefficient of the force sensor cladding (PDMS) is considered, which results in the Q-factors being systematically lower than the Q-factors of the reference sensor by a little bit. Due to the reference sensor's lower cross-sectional area, a higher cladding refractive index and the absence of the cladding extinction coefficient, the Q-factors of the reference sensor is expected to be lower than the force sensor in practice, similar to what it is shown in subsection 7.2.2, specifically Figure 7.25.

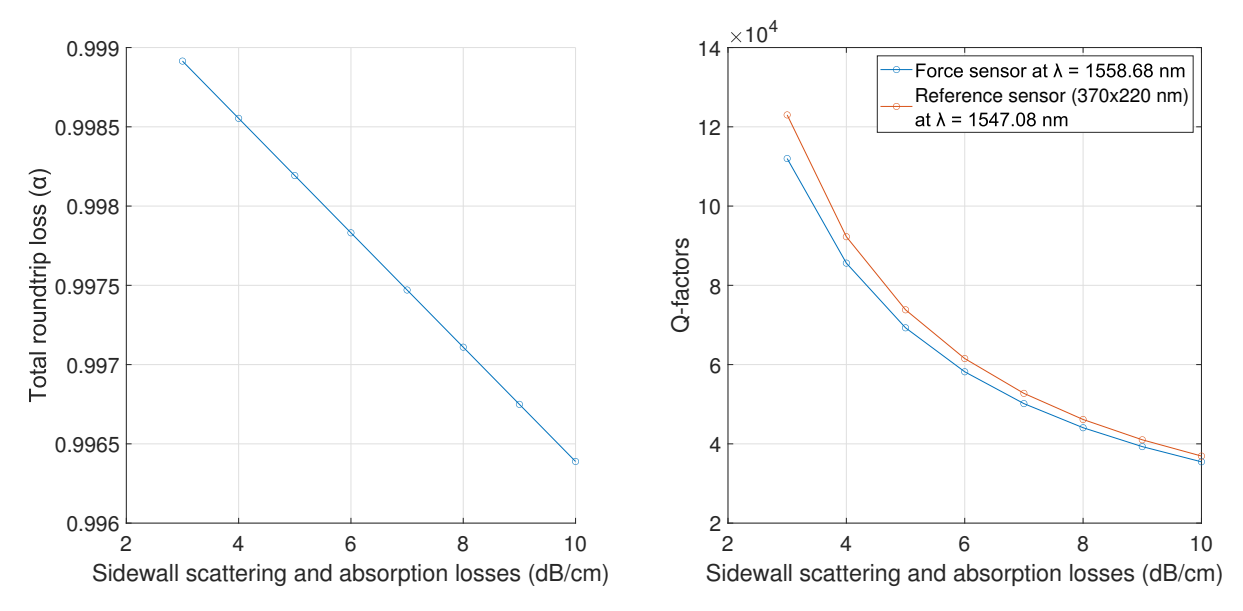


Figure 7.10: Total roundtrip loss of the reference sen- Figure 7.11: Q-factors of both the force and reference sor $(370x220 \, nm)$ at $\lambda = 1547.08 \, nm$ sensor at different propagation loss α_{wq} .

7.1.3 Coupling Simulations

The coupling process for a gap length of $200 \, nm$, $250 \, nm$ and $300 \, nm$ have been simulated for both the force and the reference sensor. The results are shown in Table 7.1 and Table 7.2 respectively.

Gap length (nm)	au	$\sqrt{1-\kappa^2}$	Intensity loss $(1 - \tau^2 - \kappa^2)$
200	0.99021	0.99065	$8.75 \cdot 10^{-4}$
250	0.99571	0.99594	$4.61 \cdot 10^{-4}$
300	0.99809	0.99823	$2.64 \cdot 10^{-4}$

Table 7.1: Coupling results of the force sensor obtained from the coupling simulations in FullWAVE.

$\begin{array}{ c c }\hline \text{Gap length}\\ (nm) \end{array}$	au	$\sqrt{1-\kappa^2}$	Intensity loss $(1 - \tau^2 - \kappa^2)$
200	0.98909	0.98935	$5.19 \cdot 10^{-4}$
250	0.99524	0.9953	$2.25 \cdot 10^{-4}$
300	0.99792	0.99794	$5.54\cdot10^{-5}$

Table 7.2: Coupling results of the reference sensor obtained from the coupling simulations in FullWAVE.

From Table 7.1 and Table 7.2, it can be determined that the intensity loss is much smaller than the κ^2 (κ^2 can be calculated for each gap length by taking the values of the third column (TC) of Table 7.6 and Table 7.7 and rewriting the equation $TC = \sqrt{1 - \kappa^2}$ to $\kappa^2 = 1 - TC^2$). As explained in section 5.4, this means the intensity loss can be neglected and the expression $\tau^2 + \kappa^2 \approx 1$ can be assumed (note that the values both τ and $\sqrt{1 - \kappa^2}$ are similar).

In order for the force sensor to get critically coupled, the transmission coefficient should be equal to the total roundtrip loss as shown in Figure 7.3. For a gap length of $200\,nm$ as well as sidewall scattering and absorption loss α_{swa} of $10\,dB/cm$, an additional intensity loss (due to scattering for example) of around $0.0533\,dB$ besides τ or $\sqrt{1-\kappa^2}$ from Table 7.1 is needed for that to be the case. When α_{swa} is $3\,dB/cm$ instead, the additional required itensity loss increases to $0.0753\,dB$. These additional intensity loss are on the higher end of the value range determined in section 6.3. However, when the gap length is increased to $250\,nm$, the extra intensity loss necessary for critical coupling reduces to $0.00513\,dB$ for $\alpha_{swa} = 10\,dB/cm$ and $0.0271\,dB/cm$ for $\alpha_{swa} = 3\,dB/cm$, which is on the lower end of the values determined in section 6.3. This means the gap length should be somewhere between $200\,nm$ and $250\,nm$ in order for the force sensor to be critically coupled, based on the additional intensity losses determined in section 6.3. Increasing the gap length beyond $250\,nm$ results in the transmission coefficient to be very close to the roundtrip losses from Figure 7.3 without any coupling scattering losses. Since scattering losses will happen in practice, a gap length of larger than $250\,nm$ will not critically couple the ring resonator based on this analysis.

A similar phenomenom can be seen for the reference sensor. For a gap length of $200\,nm$, the additional intensity loss must be around $0.06387\,dB$ and $0.08585\,dB$ for $\alpha_{swa}=10\,dB/cm$ and $3\,dB/cm$ respectively. If the gap length is $250\,nm$ instead, then the extra required intensity losses become $0.01005\,dB$ and $0.03206\,dB$ respectively. Further increasing the gap length can cause the reference sensor to be undercoupled for larger α_{swa} values.

7.1.4 Wafer-Scale Fabrication Error Induced Spectral Deviations

For wafer scale fabrication error analysis (as mentioned in section 6.1), both the width and the height of the waveguide have been sweeped individually to determine its effect on the Q-factor, sensitivity and the intrinsic limit-of-detection. The waveguide widths of $400 \, nm$, $450 \, nm$ and $500 \, nm$ and heights of $200 \, nm$, $220 \, nm$ and $240 \, nm$ are simulated. The change of Q-factor, sensitivity and the iLOD as a result of varying these cross-sectional dimensions are shown in Figure 7.12.

All plots in Figure 7.12 and Figure 7.13 are curve-fits of the simulated data using second-order polynomials. It can be seen in Figure 7.12a that the width change of $50\,nm$ can cause the Q-factor to increase or decrease by around 33%, while a height change of $20\,nm$ results in Q-factor change of roughly 15%. The Q-factors are taken at critical coupling with $\tau = \alpha_{rad}$. The reason why α_{swa} determined in section 6.3 is not considered is because the relation between α_{swa} and the waveguide width and height is unknown. Only considering radiation (and PDMS absorption) losses calculated using FemSIM results in very large Q-factors that are not likely to appear in practice, but its value in relation to the cross-sectional dimensions of the waveguide can be observed. Figure 7.12b shows that the width increase and decrease by $50\,nm$ result in a sensitivity changes of $-15.95\,nm/RIU$ and $+29.04\,nm/RIU$ respectively, while the height increase and decrease result in $-7.55\,nm/RIU$ and $+9.85\,nm/RIU$. This shows that the change in sensitivity due to cross-sectional dimension

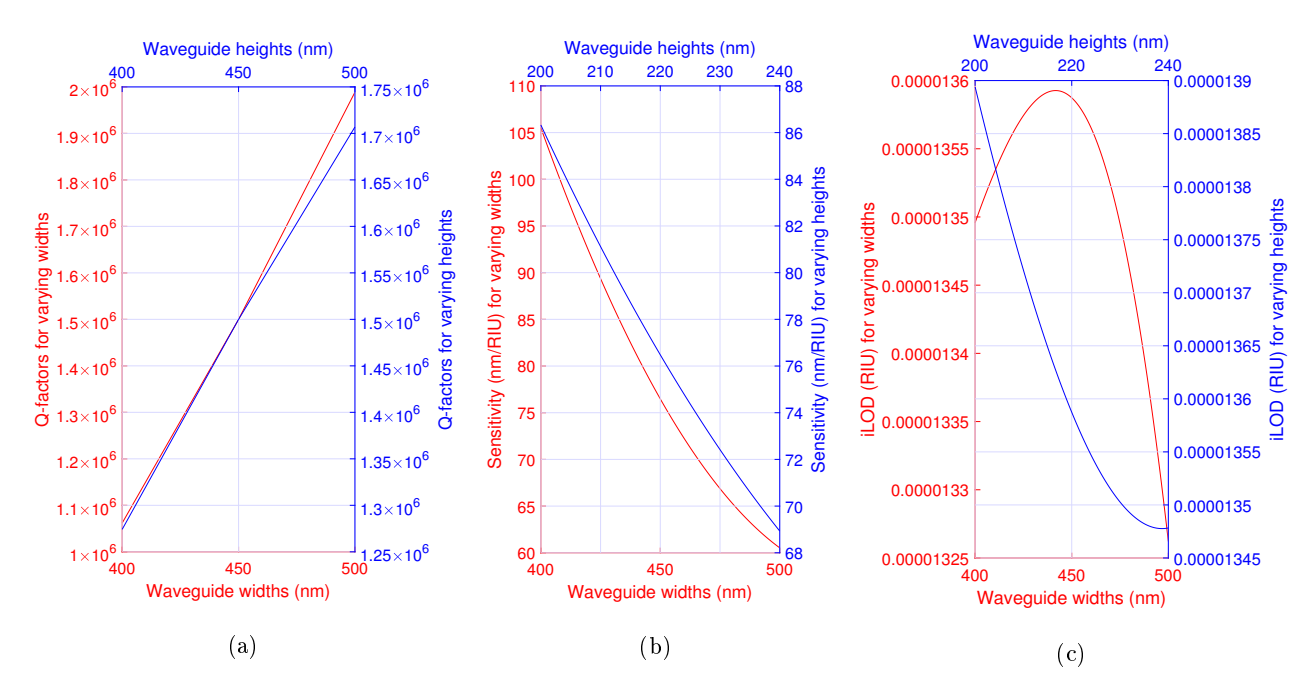


Figure 7.12: Varying waveguide widths and heights versus (a) Q-factors, (b) Sensitivities, (c) Intrinsic limit-of-detections.

changes is nonlinear. In the end, the iLOD stays between $1.3 \cdot 10^{-5} RIU$ and $1.4 \cdot 10^{-5} RIU$ despite the changes in the cross-sectional dimensions.

The difference between the temperature sensitivities of both the force sensor and the reference sensor for varying waveguide width and height changes is shown in Figure 7.13. It can be seen that the changes in the waveguide height have little effect on the temperature sensitivity difference and therefore also on the spectral deviations due to temperature drifts and wavelength repeatability. On the other hand, the temperature sensitivity difference can go up to $8\,pm/K$ when the widths vary up to $50\,nm$. The reasons for this could be that the nominal waveguide widths are different $(450\,nm$ versus $370\,nm)$, while the nominal waveguide heights remain the same $(220\,nm)$ and that the TE0 mode field is horizontally oriented. In Figure 7.13 at a width change of $-50\,nm$, the temperature sensitivity ratio $\left(\frac{\partial \lambda}{\partial T}\right)_{sense}/\left(\frac{\partial \lambda}{\partial T}\right)_{ref}$ appearing in Equation 5.25 is roughly 1.39.

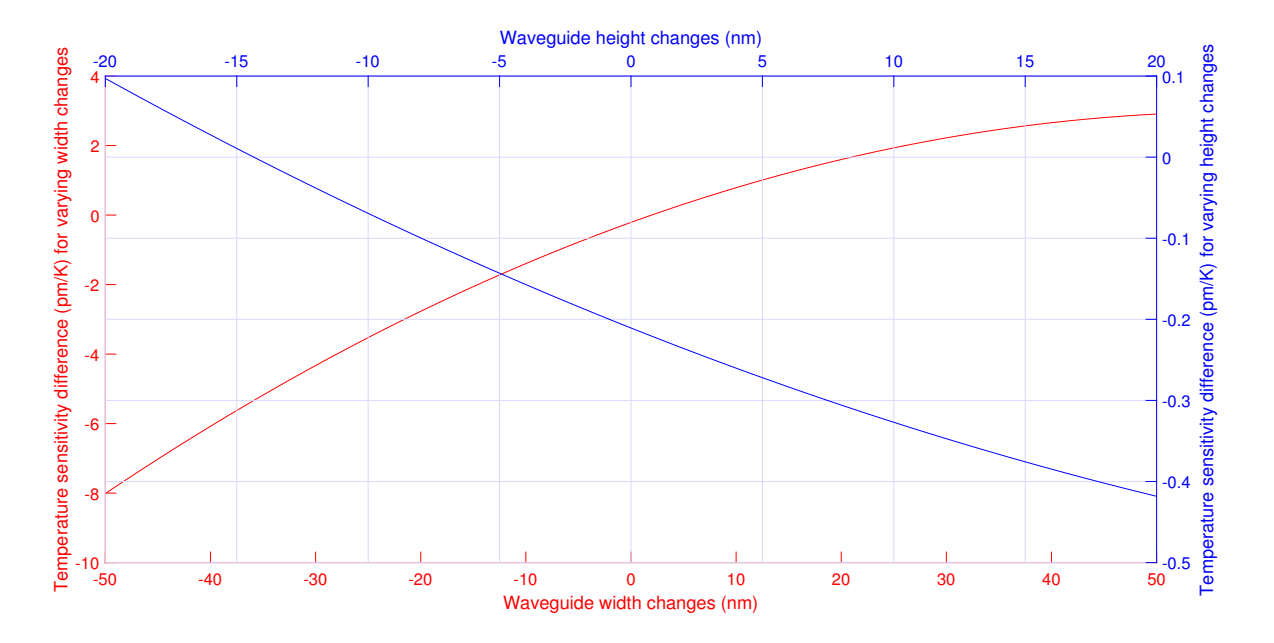


Figure 7.13: Difference in temperature sensitivity for varying waveguide widths and heights.

7.1.5 Die-Scale Fabrication Error Induced Spectral Deviations

To determine the resonance wavelength shifts due to die-scale fabrication errors, a $5 \,\mu m$ radius ring resonator with a nominal waveguide cross-section of $410x200\,nm$ (which is similar to the dimensions determined in section 6.2) has been analyzed. The widths are varied by $\pm 0.5\,nm$ (1σ) and $\pm 1.5\,nm$ (3σ), which are close to the values calculated in section 6.2. The resonance wavelength deviations for the force and reference sensor are shown in Table 7.3 and Table 7.4.

Width change (nm)	$n_{eff}(\lambda_c)$	$n_q(\lambda_c)$	Resonance wavelength (nm)	Resonance wavelength
vvidin change (mm)	$meff(N_c)$	$n_g(N_c)$	at resonance order $m=43$	shift (nm)
-1.5	2.15378	4.22280	1561.926	-1.626
-0.5	2.15667	4.22116	1563.010	-0.541
0	2.15811	4.22036	1563.551	0
+0.5	2.15955	4.21953	1564.091	+0.540
+1.5	2.16240	4.21796	1565.164	+1.613

Table 7.3: Resonance wavelength shift due to die-scale width deviations of the force sensing ring resonator $(R = 5 \,\mu m)$ with a nominal cross-section of $410x200\,nm$. Both n_{eff} and n_g at $\lambda_c = 1550\,nm$ are required to determine the resonance wavelength itself.

Width change (nm)	n())	$n_q(\lambda_c)$	Resonance wavelength (nm)	Resonance wavelength
width change (nm)	$n_{eff}(\lambda_c)$	$n_g(\lambda_c)$	at resonance order $m = 41$	shift (nm)
-1.5	2.00855	4.09654	1544.606	-2.306
-0.5	2.01263	4.10162	1546.144	-0.767
0	2.01467	4.10410	1546.912	0
+0.5	2.01669	4.10654	1547.677	+0.765
+1.5	2.02074	4.11119	1549.202	+2.291

Table 7.4: Resonance wavelength shift due to die-scale width deviation of the reference ring resonator $(R = 5 \,\mu m)$ with a nominal cross-section of $330x200\,nm$. Both n_{eff} and n_g at $\lambda_c = 1550\,nm$ are required to determine the resonance wavelength itself.

It can be seen that the standard width deviation of $0.5\,nm$ results in a standard resonance wavelength deviation of around $0.54\,nm$ for the force sensor. The group index at the resonance wavelength of $1563.551\,nm$ is 4.21963. Considering a ring radius of $5\,\mu m$, the FSR (calculated with Equation 5.1) is $18.4\,nm$. The reference sensor shows larger resonance peak shift for the same width nonuniformity compared to the force sensor as shown in Table 7.4.

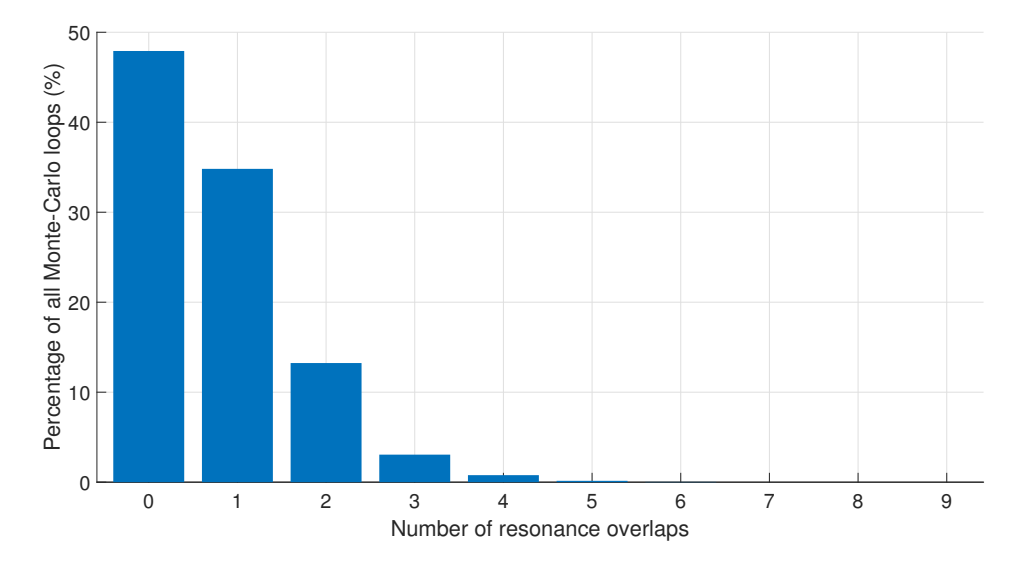


Figure 7.14: Resonance overlap percentage for multiplexed ring resonators with $5 \,\mu m$ radius and a cross-section of $410x200 \,nm$.

Afterwards, a resonance peak overlap analysis similar in subsection 6.2.2 can be made. The effective extinction coefficient $Im|n_{eff}|$ for a bend waveguide with a cross-section of $410x200\,nm$ and a radius of $5\,\mu m$ is $2.33571\cdot 10^{-6}$, resulting in $\alpha_{rad}=0.99986218$. Assuming that the sidewall roughness and absorption induced propagation loss is $6.5\,dB/cm$ or $\alpha_{swa}=0.9976518$ which is the average of the values from Table 6.4, the FWHM is then equal to $29.22\,pm$. All resonance seperation distance are equal, which can be calculated by dividing the FSR by the number of resonance peaks N_{rings} . Finally similar to subsection 6.2.2, the resonance peaks are considered to be overlapped when the seperation distance is below $3\cdot FWHM$. Using these and the aforementioned variables, the amount of multiplexable ring resonators (with $R=5\,\mu m$ and $410x220\,nm$) that results in 80% of all resonance peaks not being overlapped is 18. The overlap statistics are shown in Figure 7.14. Having 18 multiplexed ring resonators or resonance peaks in a FSR means that the amount of resonance overlaps should not exceed 1 (i.e. two resonance peaks overlapping one another) in order for 80% of all resonance peaks not to be overlapped. Figure 7.14 shows that the combined probability of zero and a single overlap is 82.74%.

7.2 Small-Sized Sensor Design

Small ring resonators are required to satisfy the maximum sensor seperation of $10\,\mu m$ as shown in section 1.3. Small ring resonators (i.e. ring resonators with radius of below $3\,\mu m$) show higher radiation loss due to the smaller radius of curvature of the waveguide bends. Although the sensitivity (for both the force and reference sensor) increases as a result of it due to more electromagnetic field being outside of the waveguide, the extra radiation loss causes the Q-factor of the resonance peak to decrease (which is also shown in Figure 7.5 for the $R=5\,\mu m$ ring resonator). A Q-factor for a ring resonator with $R=2\,\mu m$ of below 10000 has been reported [100]. Equation 4.4 shows that the decrease of the Q-factor results in an increase of the FWHM. This phenomenom prevents many ring resonators to be multiplexable on a single bus waveguide without any resonance peak overlap. It has been explained in the resonance peak overlap analysis from subsection 6.2.2 that a seperation distance of two resonance peaks of $> 3 \cdot \Delta \lambda_{FWHM}$ is required for it not to be considered overlapped. Therefore, a new ring resonator design as shown in Figure 7.15 has been proposed to overcome the radiation loss while keeping the design compact.

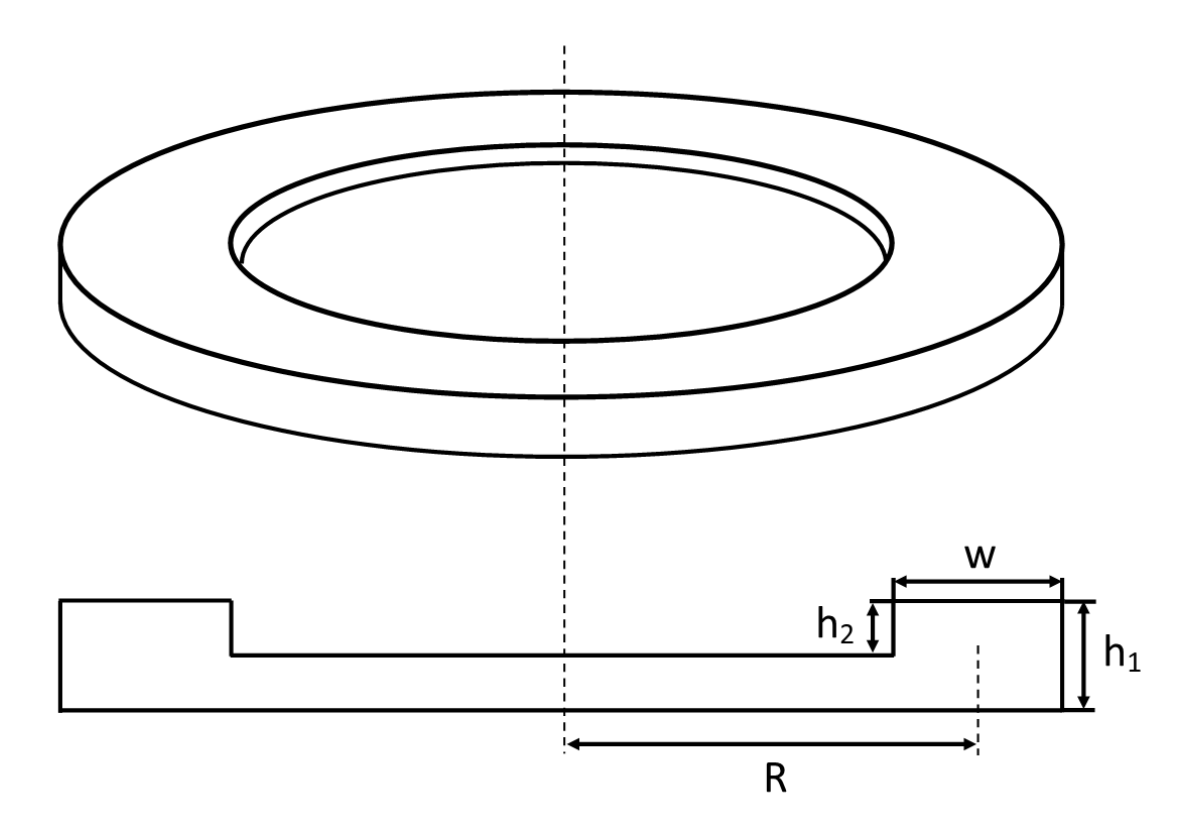


Figure 7.15: New small ring resonator design

The new ring resonator design consists of a ring radius R, waveguide width w and height h_1 similar to a strip waveguide as well as a slab layer in the inner part of the ring resonator resulting from a partial etch h_2 .

For the same reasons as the ones of the $R=5\,\mu m$ ring resonator that are explained in the introduction of section 7.1, the width w and height h_1 are $450\,nm$ and $220\,nm$ respectively for the force sensor. The radius R is chosen to be $2\,\mu m$, since this ring resonator radius satisfies the array density requirement as mentioned in section 1.3 and a regular shaped ring resonator with the same radius has already been successfully fabricated and experimentally characterized by W-Lab (unlike $R=1.5\,\mu m$).

Similar to a rib waveguide, the slab layer increases the mode field confinement and therefore decrease both the radiation as well as side-wall scattering losses (this has also been explained in subsection 3.2.2). The (partial) etch depth h_2 of $70\,nm$, $100\,nm$ and $220\,nm$ have been analyzed, as these etch depths can be fabricated at cornerstone [93]. When $h_2 = 0\,nm$, then this design will resemble a disk resonator, which has not been considered in this design report. The reason for this is that the waveguide widths of the reference ring resonator has been varied in order for its temperature sensitivity to become equal to the one of the force sensor (which is shown in subsection 7.1.3). A disk resonator does not have any waveguide width, making it impossible to apply this temperature sensitivity equalization technique. To equalize temperature sensitivities of disk resonators, the waveguide thickness or the disk radius can be varied. Fine tuning the thickness cannot be done at Cornerstone due to the very limit available etch depths [93]. Varying the radius also influences the resonance wavelength due to the change in the cavity length L from Equation 3.1. The change of the temperature sensitivity and the resonance wavelength become dependent on each other, which is not the case for ring resonators. It has been shown in section 7.3 that radius variation is restricted to fine tuning the resonance wavelengths only.

In this section, the new ring resonator design will be analyzed mostly in the same way as the $R=5\,\mu m$ ring resonator study from section 7.1. As explained in the introduction of section 7.1, the $R=5\,\mu m$ ring resonator analysis is intended as a platform for experimenting the temperature and wavelength repeatability compensation with the reference sensor. On the other hand, the $R=2\,\mu m$ ring resonator is specifically designed as a small force sensor that satisfies the requirements from section 1.3. These two ring resonator designs are considered to be separate results from this thesis. The simulations results of $R=2\,\mu m$ and $R=5\,\mu m$ ring resonator designs are not compared to each other, since the radius as well as the inner slab layer height (which is $0\,nm$ for the $R=5\,\mu m$ ring resonator design) differ for both designs.

7.2.1 Intrinsic Limit-of-Detection

By determining $n_{eff}(\lambda_c)$, $\kappa_{eff}(\lambda_c)$, $n_g(\lambda_c)$, $n_g(\lambda_m)$ with $\lambda_m \approx \lambda_c = 1550 \, nm$ and $n_{eff}(\lambda_c)$, $n_{clad} = 1.39$) (to calculate the sensitivity described in section 5.3) in a similar way as shown in subsection 7.1.1, the intrinsic limits-of-detection for critical coupling can be determined for the new ring resonator design for varying etch depths h_2 . This is shown in Table 7.5. Similar to the results from Figure 7.12c, only the radiation losses calculated with FemSIM have been considered in Table 7.5. The influence of the slab layer height on the sidewall scattering and absorption losses cannot be determined with RSoft.

Slab height $h_1 - h_2$ (nm)	FWHM (pm)	Sensitivity (nm/RIU)	iLOD (RIU)
0	3.965	81.29	$4.878 \cdot 10^{-5}$
100	1.643	64.65	$2.545 \cdot 10^{-5}$
150	0.941	50.74	$1.783 \cdot 10^{-5}$

Table 7.5: Sensor performance of different ring resonator designs.

From Table 7.5, it can be seen that the intrinsic limit-of-detection for the ring resonator design with a slab height of 150 nm is the lowest out of the three despite having the lowest sensitivity. However in section 7.4, it is shown that the sensitivity has a larger contribution to the limit-of-detection compared to the FWHM (or Q-factor). This makes a ring resonator without a slab height more suitable for reaching lower limits-of-detection due to having a sensitivity of $81.29 \, nm/RIU$. However, the decreased Q-factor (i.e. increased FWHM) makes it less suitable for multiplexing ring resonators on a bus due to higher probability of resonance peak overlaps. For this reason, it is decided to explore the characteristics of a slab height of $100 \, nm$. The reason why this slab height is chosen is to obtain sharper resonance peaks (i.e. lower FWHM and higher Q-factors) while maintaining a sensitivity that is as high as possible. It is shown in section 7.4 that a sensitivity of $64.65 \, nm/RIU$ is sufficient for $1 \, \mu N$ force limit-of-detection (in the case of most force exertion areas analyzed in section 7.4). Whether the Q-factor gets improved in practice should be determined with experiments as a follow-up research.

When $h_1 - h_2 = 100 \, nm$, the complex effective index and the group index at the central wavelength of $\lambda_c = 1550 \, nm$ are $n_{eff}(\lambda_c) = 2.41369 + i \cdot 2.43123 \cdot 10^{-6}$ and $n_g(\lambda_c) = 3.94450$ respectively. These values result in a roundtrip loss due to radiation of $\alpha_{rad} = 0.99994869$. The total roundtrip loss α can be determined for different sidewall scattering and absorption losses (α_{swa}) by adding α_{swa} to the radiation roundtrip loss (α_{rad}) .

A linear decrease of α can be observed in Figure 7.16 from 0.99951 to 0.99850 for scattering and absorption losses of $3\,dB/cm$ to $10\,dB/cm$.

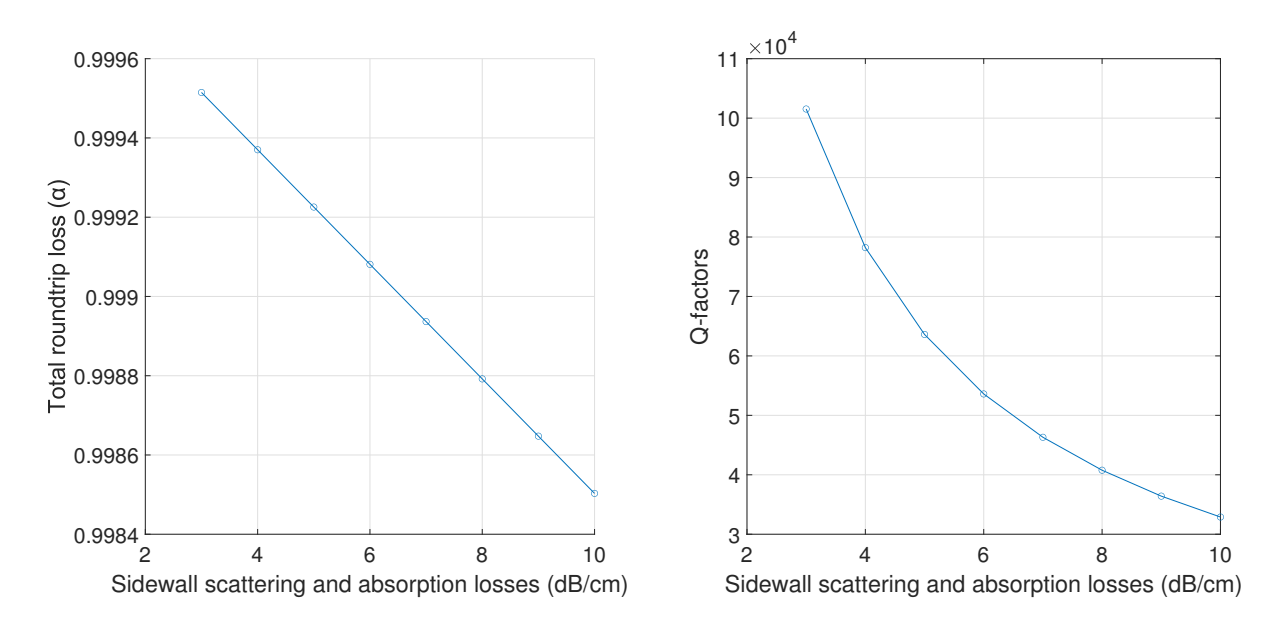


Figure 7.16: Total roundtrip loss for varying sidewall Figure 7.17: Q-factors versus propagation losses α_{swa} scattering and absorption losses of the force sensor—with resonance order m = 19.

Besides the total roundtrip loss, the FWHM as well as the Q-factor for different sidewall scattering and absorption losses (similar to Figure 7.5) can also be determined as shown in Figure 7.17. This is done by substituting $n_{eff}(\lambda_c) = 2.41369 + i \cdot 2.43123 \cdot 10^{-6}$ and $n_g(\lambda_c) = 3.94450$ in Equation 3.2, which shows a resonance wavelength of $\lambda_m = 1578.06 \, nm$ at m = 19 (this is the closest resonance wavelength to λ_c while still being inside the measurement spectrum of 1530-1620 nm as shown in e.g. Figure 6.3). This results in $n_g(\lambda_m = 1578.06 \, nm)$ of 3.3935. The Q-factor can then be calculated by substituting λ_m , $n_g(\lambda_m)$ and the total roundtrip losses (α) from Figure 7.16 in Equation 4.3 as well as Equation 4.4. From Figure 7.17, it can be seen that the Q-factor decreases from 101534 to 32895 for an increasing scattering and absorption loss from $3 \, dB/cm$ to $10 \, dB/cm$.

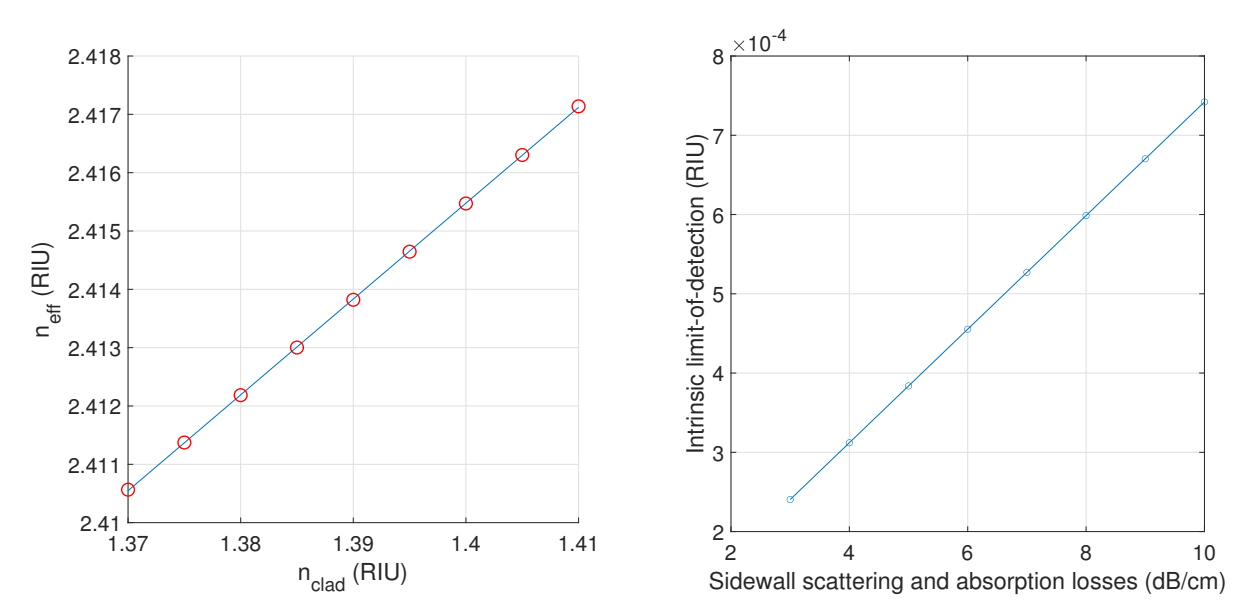


Figure 7.18: Effective refractive index data points cal- Figure 7.19: Intrinsic limit-of-detections versus vary-culated with RSoft at different cladding refractive in- ing propagation losses α_{swa} with resonance order at dices (red) and a corresponding curve-fit (blue) m = 19.

The effective index at $n_{clad} = 1.39$ is determined to be 2.41382, resulting in a sensitivity of $64.65 \, nm/RIU$

using the steps described in section 5.3. Figure 7.18 shows that a nearly linear relation between the effective refractive index and the cladding refractive index for the $R=2\,\mu m$ ring resonator design, similar to the $R=5\,\mu m$ design as shown in Figure 7.4. The derivative $\frac{\partial n_{eff}}{\partial n_{clad}}$ of the curve-fit equation at a PDMS refractive of $n_{clad}=1.3892$ is 0.164, which results in a sensitivity of $64.52\,nm/RIU$ (calculated using Equation 3.3 with $n_g(\lambda_c)=3.94450$). This value is very close to the aforementioned sensitivity of $64.65\,nm/RIU$. The curve-fitting errors of the data points in Figure 7.18 varies from approximately $-5.9 \cdot 10^{-8}$ to $-5.9 \cdot 10^{-7}$.

Combined with the Q-factors as shown in Figure 7.17, the intrinsic limits-of-detection for different scattering and absorption losses can be calculated using Equation 4.2. The results are shown in Figure 7.19. It can be seen that the iLOD can potentially decrease from $7.42 \cdot 10^{-4} \, RIU$ to $2.40 \cdot 10^{-4} \, RIU$ for decreased scattering and absorption loss.

7.2.2 Temperature Drift

A temperature drift analysis similar to subsection 7.1.2 is carried out for the $R=2\,\mu m$ ring resonator in this section. The same refractive index of 1.53 and a TOC of $-2\cdot 10^{-4}K^{-1}$ for the reference sensor cladding material is therefore taken (which is arbitrarily chosen from the optical property value range of Ormocer as shown in subsection 7.1.2). However in this temperature drift analysis, the temperature sensitivity of a force sensor with a 500 nm waveguide width and a reference sensor with a 350 nm width are calculated instead of widths of 450 nm and 370 nm used in subsection 7.1.2. A waveguide width of 350 nm is the smallest feature size Cornerstone can make for an etch depth of $220\,nm$ [93], while the waveguide width should also not exceed $500\,nm$ to prevent higher order mode excitations [101]. A force sensor with a waveguide width of $500\,nm$ has a group index at the central wavelength of $n_g(\lambda_c)=3.93686$, while $n_g(\lambda_c)=3.81114$ for a reference sensor with a waveguide width of $350\,nm$ (Determined with dispersion simulations of FemSIM as described in section 5.2). The effective index at different temperatures with the aforementioned cladding optical properties and waveguide widths are shown in Figure 7.20 and Figure 7.21. $\frac{\partial n_{eff}}{\partial T}$ can be determined by fitting first-order polynomial equation in the data or using Equation 5.18 (with e.g. $T_1=-10\,K$ and $T_2=+10\,K$) as described in subsection 5.5.3 and subsection 7.1.2.

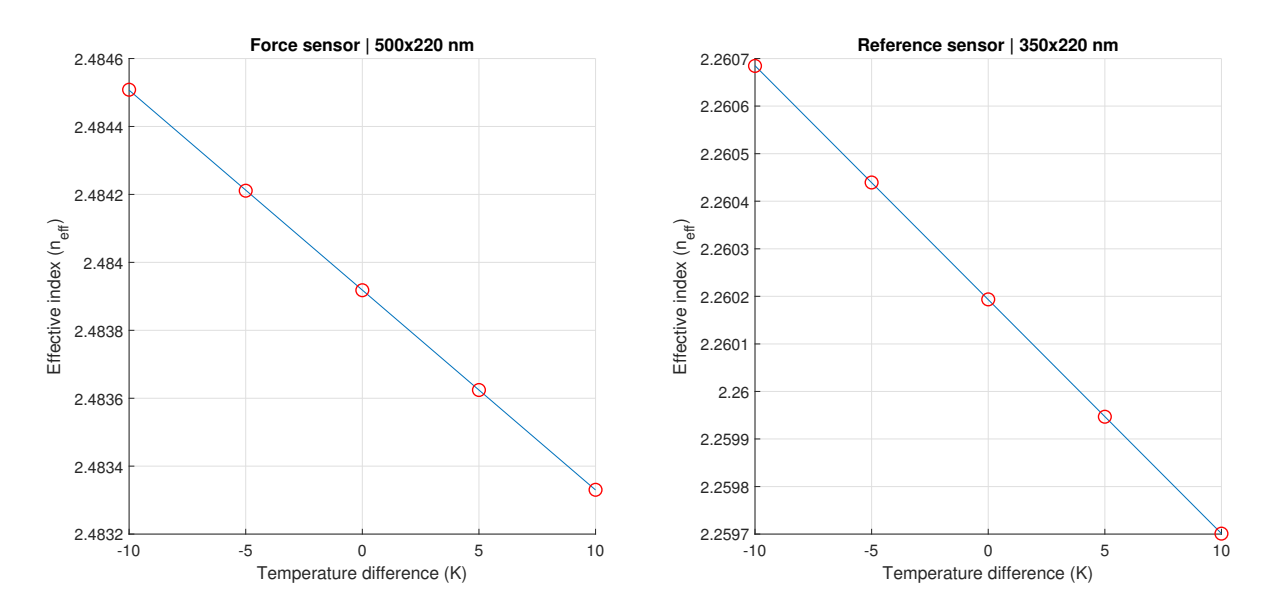


Figure 7.20: $\frac{\partial n_{eff}}{\partial T}$ at $\lambda=1550\,nm$ of the force sensor Figure 7.21: $\frac{\partial n_{eff}}{\partial T}$ at $\lambda=1550\,nm$ of the reference with $500x220\,nm$ ridge waveguide cross-section sensor with $n_{clad}=1.53$ and $TOC_{clad}=-2\cdot 10^{-4}\,K^{-1}$

Figure 7.20 shows that using the line-fit method results in $\frac{\partial n_{eff}}{\partial T} = -5.89 \cdot 10^{-5} \, K^{-1}$ for a force sensor with a waveguide width of $500 \, nm$, while $\frac{\partial n_{eff}}{\partial T}$ of the reference sensor with a width of $350 \, nm$ is equal to $-4.92 \cdot 10^{-5} \, K^{-1}$ according to the plot of Figure 7.21. Using Equation 5.17 with the aforementioned values of $n_g(\lambda_c)$ and $\frac{\partial n_{eff}}{\partial T}$, the temperature sensitivity of the force sensor is equal to $S_{t,force} = -23.17 \, pm/K$, while the one of the reference sensor is $S_{t,ref} = -20.00 \, pm/K$. The fitting error ranges from $7.2 \cdot 10^{-8}$ to $1.6 \cdot 10^{-6}$. When using Equation 5.18 instead of line-fitting, the temperature sensitivities become $23.18 \, pm/K$ and $20.00 \, pm/K$ respectively, which are identical to the results determine from the slope of the line-fit. This shows there is still noticable temperature sensitivity difference despite the large waveguide width difference. For $R = 5 \, \mu m$

ring resonator design with strip waveguides, the temperature sensitivities are $S_{T,force} = 40.84 \, pm/K$ and $S_{t,ref} = 40.64 \, pm/K$ after similar reference waveguide width changes (see subsection 7.1.2). The temperature sensitivity difference is much smaller for $R = 5 \, \mu m$ ring resonator design compared to the $R = 2 \, \mu m$ ring resonator design despite the large waveguide width changes. A slab height of $100 \, nm$ still allows for some variation in the optical properties of the reference cladding material, but not to the extend as shown for ring resonators with strip waveguides.

The temperature sensitivity of the $R=2\,\mu m$ reference ring resonator of $-20.00\,pm/K$ needs to be lower to more closely match the one of the force sensor $(-23.17\,pm/K)$. This can be done by taking a different refractive index and a TOC of the reference sensor cladding material. A hybrid-polymer called "Ormocore" produced by Micro Resist Technology GmbH, which is based on Ormocer, has a refractive index at $\lambda=1550\,nm$ of 1.543 (and an optical loss of $0.6\,dB/cm$ at $\lambda=1550\,nm$) [94]. Research has shown that the TOC value of Ormocore can reach $-3.385\cdot 10^{-4}\,K^{-1}$ at the same wavelength as well as at TE0 mode [102]. These optical properties replace the previously used refractive index of 1.53 and a TOC of $-2.0\cdot 10^{-4}\,K^{-1}$ to further equalize both temperature sensitivities (since the temperature sensitivities of $S_{T,force}=-23.17\,pm/K$ and $S_{T,ref}=-20.00\,pm/K$ are still not close enough compared to the $R=5\,\mu m$ ring resonator temperature sensitivities of $S_{T,force}=40.84\,pm/K$ and $S_{t,ref}=40.64\,pm/K$). Finally, the Young's modulus of Ormocore is around $1\,GPa$ [103], which allows the reference ring resonators to be shielded from external forces.

Taking the optical properties of Ormocore instead result in $n_g(\lambda_c) = 3.89365$ the reference sensor with a cross-section of $450 \times 220 \, nm$. For the force sensor with the same cross-section, $n_g(\lambda_c) = 3.94450$ (which was determined in subsection 7.2.1). The effective index at different temperatures for both the force and reference sensor are shown in Figure 7.22.

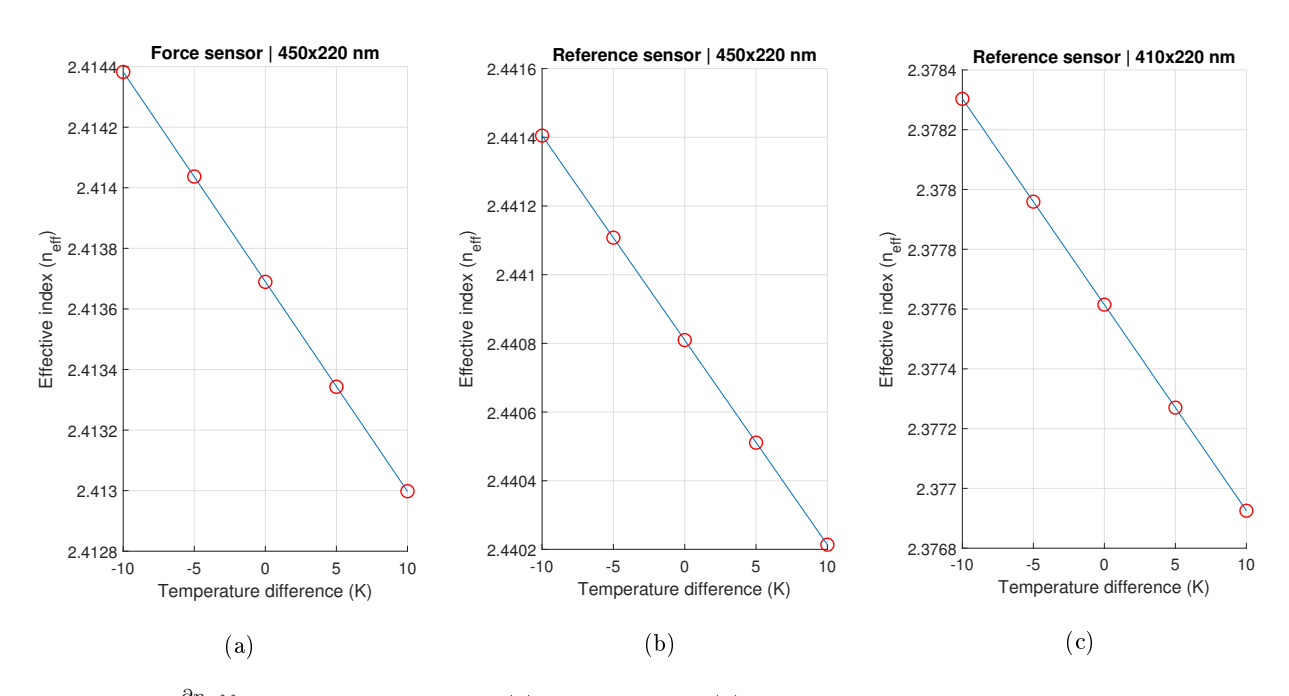


Figure 7.22: $\frac{\partial n_{eff}}{\partial T}$ at $\lambda=1550\,nm$ for (a) force sensor, (b) reference sensor with the same cross-sectional dimensions as the force sensor and (c) reference sensor with adjusted waveguide width to equalize temperature sensitivity with the one of the force sensor

It can be seen from the line-fits in Figure 7.22a and Figure 7.22b that $\frac{\partial n_{eff}}{\partial T}$ is $-6.93 \cdot 10^{-5}$, K^{-1} for the force sensor and $\frac{\partial n_{eff}}{\partial T}$ is $-5.96 \cdot 10^{-5}$, K^{-1} for the reference sensor, both having a cross-section of $450 \times 220 \, nm$. The temperature sensitivities that can be calculated with Equation 5.17 are $S_{T,force} = -27.21 \, pm/K$ and $S_{T,ref} = -23.72 \, pm/K$ assuming group indices of $n_{g,force} = 3.94450$ and $n_{g,ref} = 3.89365$ respectively. To equalize the temperature sensitivities, the waveguide width of the reference sensor must be decreased to $410 \, nm$. This results in $n_g(\lambda_c) = 3.88061$, $\frac{\partial n_{eff}}{\partial T} = -6.89 \cdot 10^{-5}$, K^{-1} (see Figure 7.22c) and finally a temperature sensitivity of $S_{T,ref} = -27.51 \, pm/K$. The temperature sensitivity difference is therefore around $0.3 \, pm/K$. The error of the fit varies from $9.6 \cdot 10^{-8}$ to $9.1 \cdot 10^{-7}$. If Equation 5.18 is used with $T_1 = -10 \, K$ and $T_2 = +10 \, K$, then the temperature sensitivities are $27.20 \, pm/K$, $23.71 \, pm/K$ and $27.51 \, pm/K$ respectively, indicating that both methods of determining $\frac{\partial n)eff}{\partial T}$ result in identical answers. It can also be seen that this temperature sensitivity difference remain roughly equal at different wavelengths as shown in Figure 7.23.

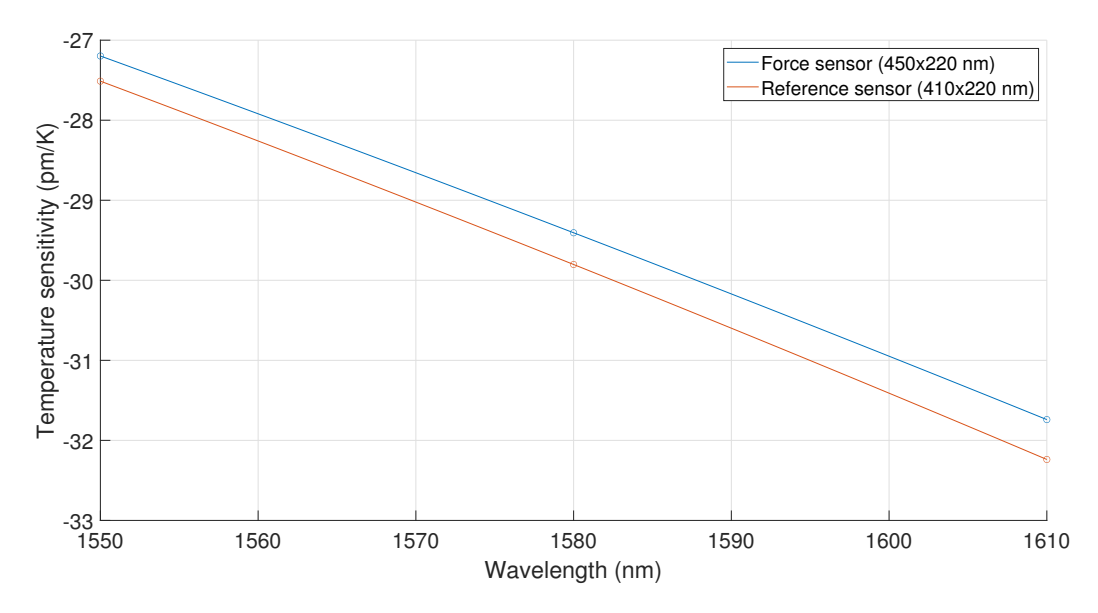
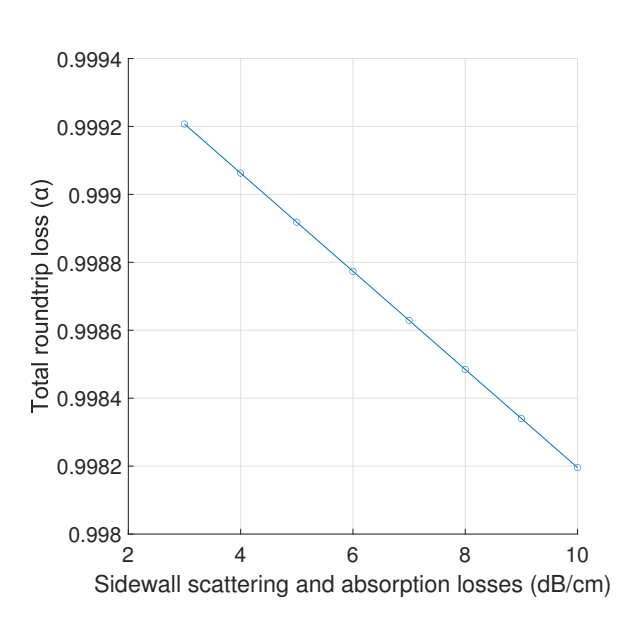


Figure 7.23: Temperature sensitivities of both the force and reference sensor at different wavelengths

Finally, the total roundtrip loss well as Q-factors of the reference sensor for different scattering and absorption loss are shown, with the latter one are also compared with the Q-factors of the force sensor from Figure 7.25. The Q-factors can be determined in the same way as described in subsection 7.1.1. It can be seen in Figure 7.24 that α decreases linearly from 0.99921 to 0.99820. It can also be seen that the difference in Q-factors is larger than for ring resonators with strip waveguides as shown in Figure 7.11, although the difference is getting smaller for larger scattering and absorption losses α_{swa} . The lower Q-factor of the reference sensor is caused by the smaller cross-sectional dimensions and the higher refractive index of the cladding. This means the intensity noise of the interrogation setup has a larger influence on the minimimum detectable wavelength shift $(\Delta \lambda_{min})$ of the reference sensor.

From this analysis, it can be observed that taking a reference sensor cladding material refractive index of higher than 1.53 and/or a TOC-value of lower than $-2 \cdot 10^{-4} \, K^{-1}$ can allow the temperature sensitivities of both the force and the reference sensor to be equalized with a error of $0.3 \, pm/K$.



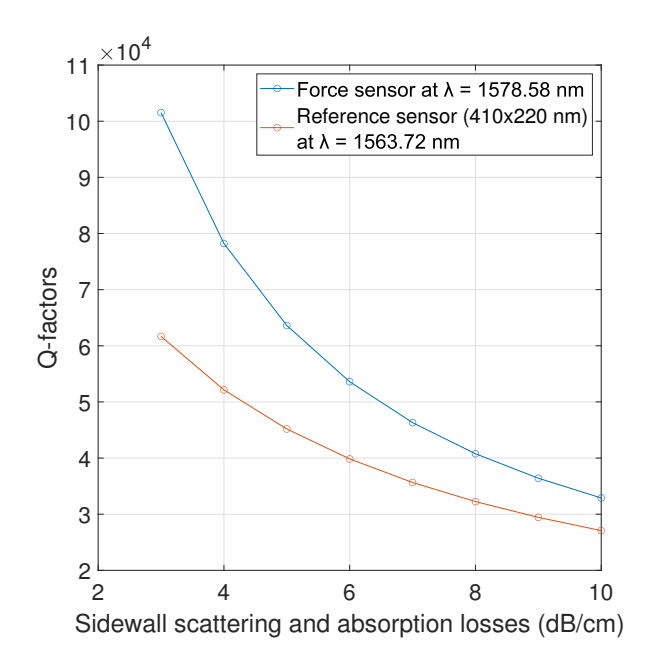


Figure 7.24: Total roundtrip loss of the reference sen- Figure 7.25: Q-factors (in the case of critical coupling) of sor (410x220 nm) at $\lambda = 1563.72 nm$

both the force sensor and the reference sensor (410×220) at different scattering and absorption losses (α_{swa})

7.2.3 Coupling Simulations

The results of the FDTD coupling simulations for the force sensor and the reference sensor are shown in Table 7.6 and Table 7.7 respectively.

Gap length (nm)	au	$\sqrt{1-\kappa^2}$	Intensity loss $(1 - \tau^2 - \kappa^2)$
200	0.99675	0.99725	$1.00 \cdot 10^{-3}$
250	0.99855	0.99883	$4.47 \cdot 10^{-4}$
300	0.99938	0.99487	$2.22 \cdot 10^{-4}$

Table 7.6: Coupling results of the force sensor obtained from the coupling simulations in FullWAVE.

$\begin{array}{ c c }\hline \text{Gap length}\\ (nm) \end{array}$	au	$\sqrt{1-\kappa^2}$	Intensity loss $(1 - \tau^2 - \kappa^2)$
200	0.99511	0.99571	$1.19 \cdot 10^{-3}$
250	0.99784	0.99813	$5.86 \cdot 10^{-4}$
300	0.99901	0.99918	$3.25 \cdot 10^{-4}$

Table 7.7: Coupling results of the reference sensor obtained from the coupling simulations in FullWAVE.

From Table 7.6 and Table 7.7, it can be determined that the intensity loss is not noticably smaller compared to κ^2 (even larger for a gap length of 300 nm) unlike the values found in Table 7.1 and Table 7.2 (κ^2 can be calculated for each gap length by taking the values of the third column (TC) of Table 7.6 and Table 7.7 and rewriting the equation $TC = \sqrt{1 - \kappa^2}$ to $\kappa^2 = 1 - TC^2$). The actual transmission coefficient value is therefore somewhere between τ (second column) and $\sqrt{1 - \kappa^2}$ (third column). The transmission coefficient should be equal to the roundtrip losses as shown in Figure 7.16 for the force sensor and Figure 7.24 for the reference sensor.

In order for that to happen for the force sensor with a gap length of $200\,nm$ as well as ring resonator sidewall scattering and absorption loss of $\alpha_{swa}=10\,dB/cm$, the additional intensity loss must be around $0.0109\,dB$ to $0.0153\,dB$. For the same gap length but with $\alpha_{swa}=3\,dB/cm$, the extra intensity loss should be roughly $0.0197\,dB$ to $0.0243\,dB$. These values for the additional intensity loss are lower than the ones calculated in section 6.3. It should be noted that the values from section 6.3 are measured and calculated for ring resonator with $5\,\mu m$ radius instead of $2\,\mu m$ for this ring resonator design. When the radius is smaller, the coupling length is shorter, resulting in coupling of lower optical intensities to the ring resonator. This could indicate that the optical intensity loss during the coupling process (τ_{loss} from Equation 6.3) is lower as well. However, this also shows that a coupling gap of larger than $200\,nm$ results in even lower required scattering loss (which may not be achievable in practice) to critically couple the ring resonator.

The results are similar for the reference sensor. In order to critically couple a reference sensor with $\alpha_{swa} = 10\,dB/cm$ and a gap length of $200\,nm$, an additional intensity loss of $0.0217\,dB$ to $0.0269\,dB$ is required. For α_{swa} , the extra intensity loss range needs to be from $0.0305\,dB$ to $0.0357\,dB$. These values are similar to the additional itensity losses of the force sensor, hence lower than the values determined in section 6.3.

Therefore, it can be observed that the coupling gap of 200 nm (which is the minimum gap length allowed by Cornerstone [93]) can potentially result in critical coupling (as it was the case with the experimentally characterized ring resonator with $R = 2 \mu m$ for graphene sensing).

7.2.4 Wafer-Scale Fabrication Error Induced Spectral Deviations

Similar to subsection 7.1.4, dispersion simulations have been carried out for varying waveguide cross-sectional dimensions. The width and height variation remain the same in this chapter (400-500 nm and 200-240 nm respectively). The inclusion of the slab layer results in an additional potential fabrication error. Cornerstone has stated an etch depth (and therefore also the slab height) error of $\pm 10 nm$ [93].

The effect of these three wafer-scale fabrication errors on the Q-factor, the sensitivity and the iLOD have been shown in Figure 7.26 and Figure 7.27. Similar to subsection 7.1.4, only the radiation and PDMS cladding absorption losses are considered in these plots, since the relation between α_{swa} and the cross-sectional dimensions is unknown. It can be seen that the Q-factor increases from $40 \cdot 10^5 - 50 \cdot 10^5$ up to around $1.5 \cdot 10^6$ for an increasing waveguide width or height, while the sensitivity drops by $20 \, nm/RIU$. This results in the iLOD decreasing for the most part when the cross-sectional area increases as shown in Figure 7.26c. The iLOD varies

between $5 \cdot 10^{-5}RIU$ and $1.7 \cdot 10^{-5}RIU$. A similar behavior can be seen for varying slab heights as shown in Figure 7.27. The Q-factor increases for an increasing slab height from $86 \cdot 10^4$ to $1.07 \cdot 10^6$, whiel the sensitivity decreases by around $4 \, nm/RIU$. Finally, this results in the iLOD dropping by roughly $0.4 \cdot 10^{-5}RIU$.

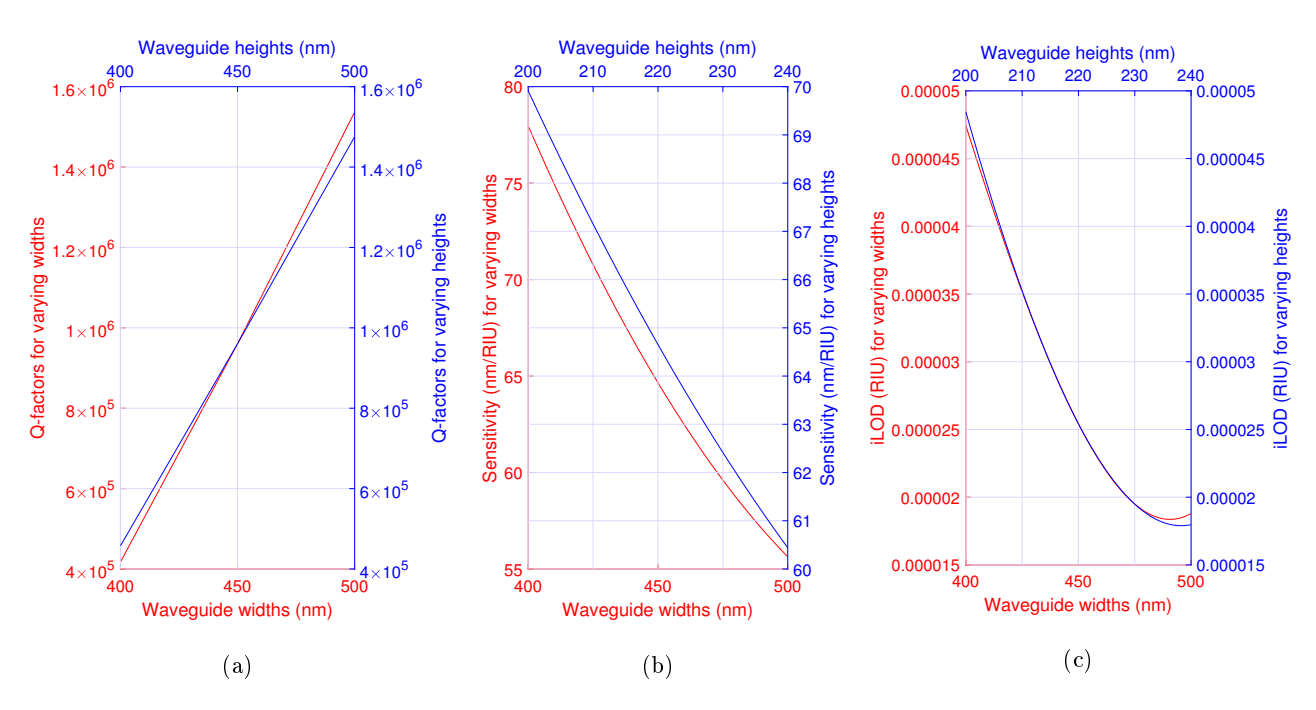


Figure 7.26: Varying waveguide widths and heights versus (a) Q-factors, (b) Sensitivities, (c) Intrinsic limit-of-detections.

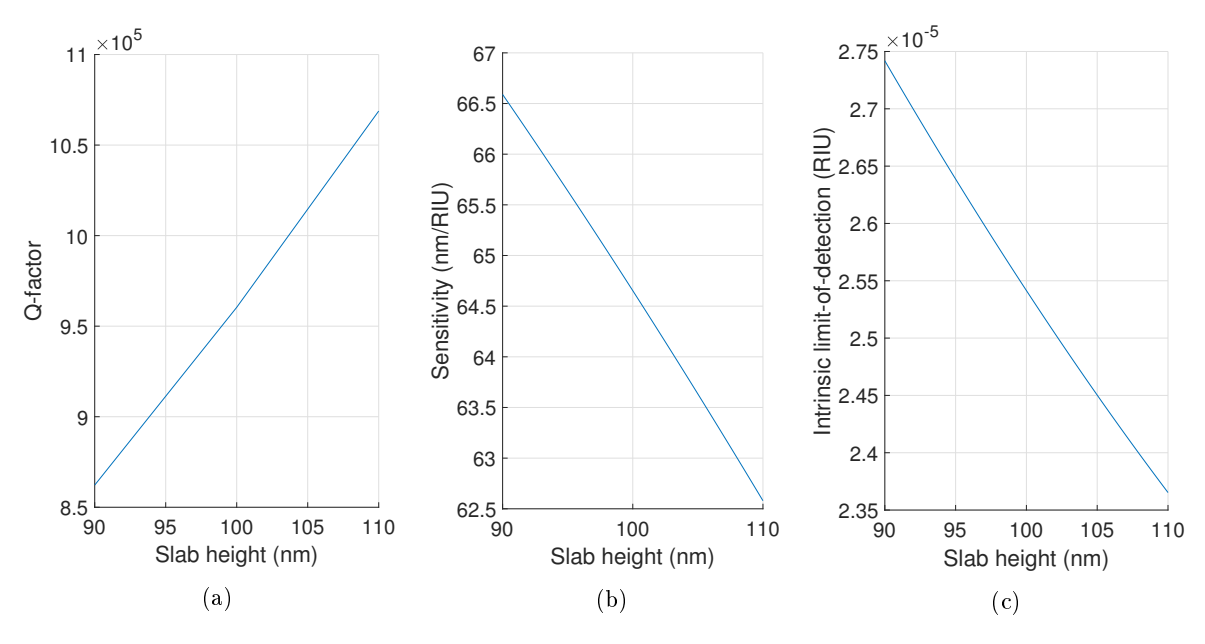


Figure 7.27: Varying slab heights versus (a) Q-factors, (b) Sensitivities, (c) Intrinsic limit-of-detections.

The effect of wafer-scale fabrication errors on the temperature sensitivity difference between the force and the reference sensor are shown in Figure 7.28. The temperature sensitivity difference for varying fabrication errors are smaller for this ring resonator design compared to the results form Figure 7.13. The difference does exceed much beyond $1\,pm/K$ for any waveguide dimension change (e.g. see the width decrease of $50\,nm$ in Figure 7.28a), making the $R=2\,\mu m$ ring resonator design more robust to wafer-scale fabrication error compared to the $R=5\,\mu m$ ring resonator from a temperature sensitivity point-of-view. However, it should be noted that the cladding material optical properties between these two ring resonator designs are different as explained in subsection 7.2.2.

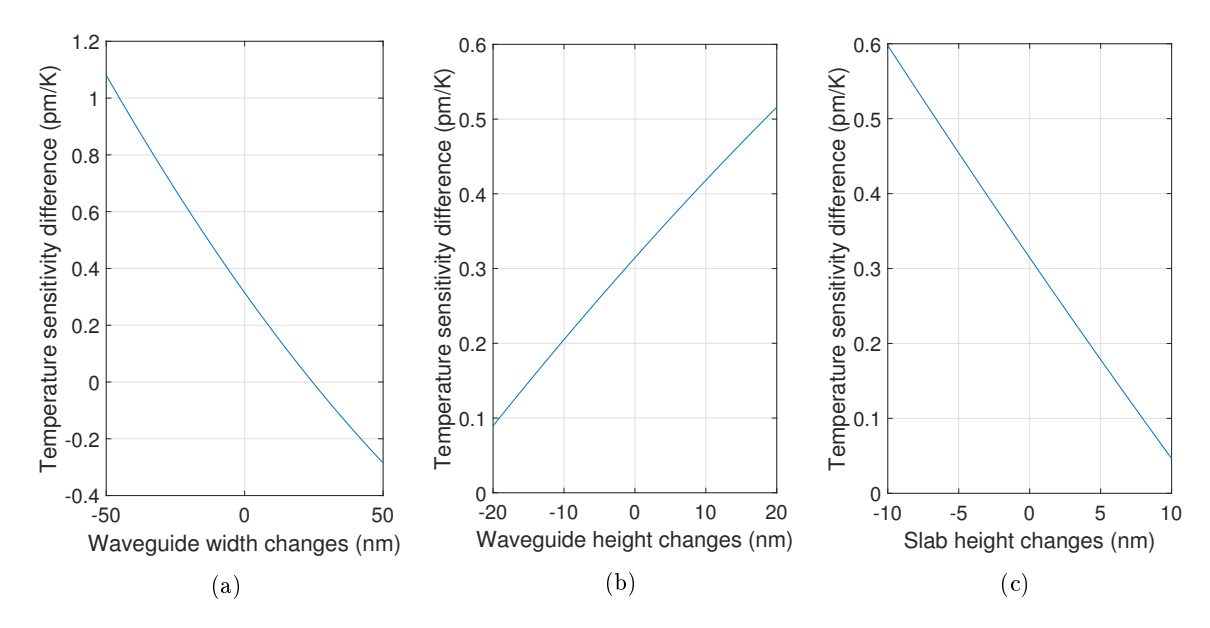


Figure 7.28: Temperature sensitivity difference between the force and reference sensor (with adjusted waveguide width) for varying waveguide (a) widths, (b) heights and (c) slab heights.

7.2.5 Die-Scale Fabrication Error Induced Spectral Deviations

An analysis similar to the one from subsection 7.1.5 has been carried out for the $R = 2 \mu m$ ring resonator design as well. The width and height of the waveguide for both the reference and the force sensor have been reduced by 40 nm and 20 nm respectively (which is a similar wafer-scale fabrication error observed in section 6.2). The results of the die-scale fabrication induced resonance wavelength shift are shown in Table 7.8 and Table 7.9.

Width change (nm)	$n_{eff}(\lambda_c)$	$n_g(\lambda_c)$	Resonance wavelength (nm)	Resonance wavelength
			at resonance order $m = 18$	shift (nm)
-1.5	2.27889	3.85942	1573.930	-1.049
-0.5	2.28059	3.86015	1574.628	-0.352
0	2.28144	3.86043	1574.980	0
+0.5	2.28229	3.86090	1575.328	+0.349
+1.5	2.28397	3.86165	1576.019	+1.040

Table 7.8: Resonance wavelength shift due to die-scale width deviations of the force sensing ring resonator $(R=2\,\mu m)$ with a nominal cross-section of $410x200\,nm$ and a slab height of $100\,nm$. Both n_{eff} and n_g at $\lambda_c=1550\,nm$ are required to determine the resonance wavelength itself.

Width abanga (mm)	m ())	m ())	Resonance wavelength (nm)	Resonance wavelength
Width change (nm)	$n_{eff}(\lambda_c)$	$n_g(\lambda_c)$	at resonance order $m=18$	shift (nm)
-1.5	2.24392	3.74894	1559.864	-1.124
-0.5	2.24572	3.75073	1560.613	-0.375
0	2.24662	3.75157	1560.988	0
+0.5	2.24752	3.75253	1561.361	+0.373
+1.5	2.24931	3.75421	1562.107	+1.119

Table 7.9: Resonance wavelength shift due to die-scale width deviation of the reference ring resonator $(R=2 \,\mu m)$ with a nominal cross-section of $370x200\,nm$ and a slab height of $100\,nm$. Both n_{eff} and n_g at $\lambda_c=1550\,nm$ are required to determine the resonance wavelength itself.

Unlike the results from subsection 7.1.5, the spectral behavior of both sensor types are more similar. The probability of resonance peak overlap is discussed in section 7.3 along with the final PIC design.

7.3 Chip Design and Fabrication

The final photonic integrated circuit design is shown in Figure 7.29.

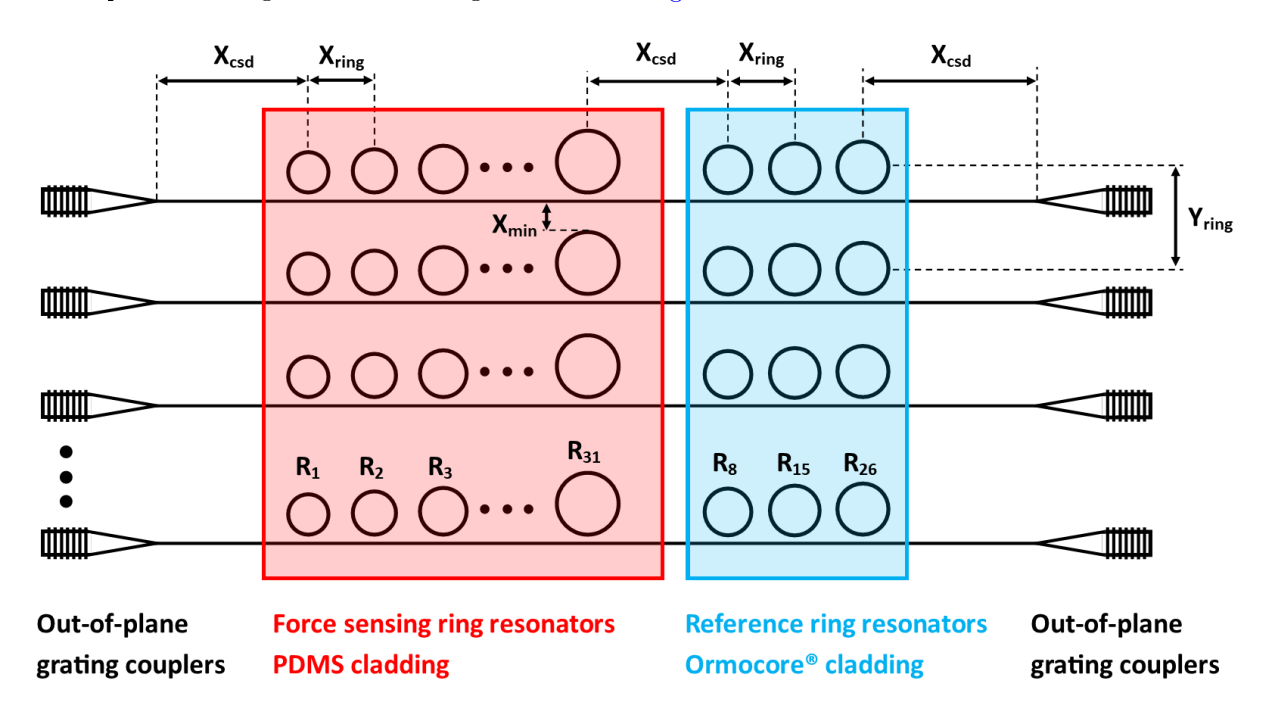


Figure 7.29: Schematic distributed force sensor design. Y_{ring} represents the center-to-center distance of ring resonators with $R = 2 \mu m$.

The chip consists of 28 identical bus waveguides $(450 \times 220\,nm)$ parallel to one other. Each of the bus waveguide contains Cornerstone's standard out-of-plane grating coupler components for coupling light into and away from the chip [93]. There are in total of 31 ring resonators with a radius of around $2\,\mu m$ on each of the bus waveguide, three of which are reference sensors. The ring resonator design used for this chip is shown in section 7.2 (i.e. force sensor waveguide cross-sectional dimensions of $450 \times 220\,nm$ and reference sensor waveguide cross-section of $410 \times 220\,nm$ with an inner slab height of $100\,nm$ for both sensor types). Based on the results of subsection 7.2.3, a gap length of $200\,nm$ has the highest chance of creating critical coupling, but this should be experimentally verified in the follow-up research.

The ring resonator center-to-center distance of $X_{ring} = Y_{ring} = 8 \,\mu m$ has been chosen. Taking this separation results in X_{min} from Figure 7.29 of (not smaller than) 2.832 μm for a reference sensor with $R=2.054 \,\mu m$ (the reason for this radius value is explained below). The propagation of the magnetic field in the y-direction from the cross-talk simulation described in section 5.6 has been shown in Figure 7.30 for $X_{min}=2.5 \,\mu m$ and a reference ring resonator with $R=2 \,\mu m$. It can be seen from Figure 7.30 that the field H_y remains inside the ring resonator (This is also the case for the other fields from the simulations). The monitor values of monitor 1 and 2 (as shown in subsection 5.6.2) are in the order of 10^{-8} . This confirms that $X_{ring}, Y_{ring}=8 \,\mu m$ result in negligible cross-talk. Considering the biological cell size is around $80 \times 80 \,\mu m$, the amount of rings that are required to cover the surface area of the cell is therefore 10×10 with $X_{ring}, Y_{ring}=8 \,\mu m$. Since the distributed force sensor has a 28×28 force sensing ring resonator grid, some cell positioning errors are allowed for it to be still covered by the force sensor grid.

It should also be noted that the waveguide width of standard out-of-plane grating coupler of Cornerstone used for this design is $10 \,\mu m$, which is smaller than $Y_{ring} = 8 \,\mu m$. If the bus waveguides are straight the entire length as shown in Figure 7.29, the grating couplers will be overlapping one other. Therefore, the actual bus waveguide design should have bends outside the force and reference region in order to create more space between the grating couplers.

An interrogation bandwidth from $1550\,nm$ to $1600\,nm$ has been chosen. The reason for this is because the standard grating coupler component from Cornerstone has high coupling efficiency at around these wavelengths, which is shown in for example Figure 6.2. The FSR of this ring resonator design is also $50\,nm$. The resonance order that corresponds to a resonance peak inside the interrogation bandwidth is m=19 for all ring resonators on the bus waveguide.

A force sensing ring resonator with a radius of $1.949 \, \mu m$ has a resonance wavelength at m=19 of $R_1=$

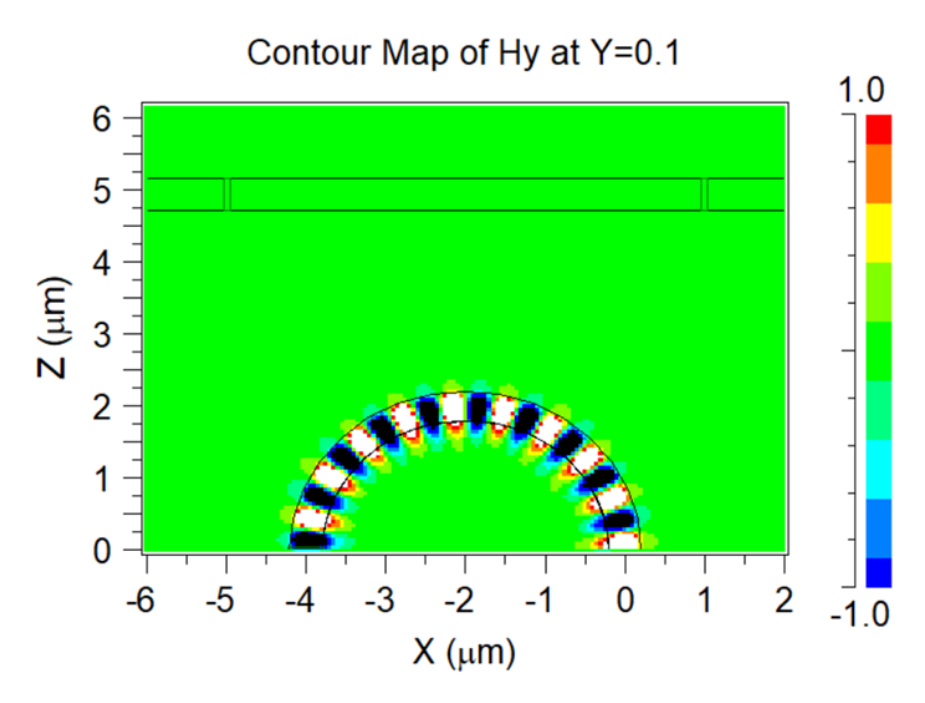


Figure 7.30: Magnetic field H_y propagation from the cross-talk simulation of the reference sensor. Other fields show similar results.

1553.167 nm (calculated with RSoft using steps described in section 5.2), which is the first resonance peak of the spectrum. By increasing the subsequent force sensing ring resonator radii with increments of $3\,nm$ up to $R_{force}=2.039\,\mu m$, 30 extra resonance peaks can be added with a seperation distance of approximately $1.452\,nm$. Therefore, the final resonance peak (corresponding to $R_{force}=2.039\,\mu m$) is calculated to be $R_{31}=1596.785\,nm$. The higher and lower resonance mode orders (m=18 and m=20) do not overlap with m=19, since $\lambda_{m=18}=1604.737\,nm$ for the first force sensor (R_1) and $\lambda_{m=20}=1547.858\,nm$ for the last force sensor (R_{31}).

Afterwards, three force sensing ring resonators with radii of $1.97 \,\mu m$, $1.994 \,\mu m$ and $2.024 \,\mu m$ are replaced by reference sensors with radii of $2 \,\mu m$, $2.024 \,\mu m$ and $2.054 \,\mu m$ respectively (i.e. R_8 , R_{15} and R_{18} from Figure 7.29). These three reference sensors have roughly the same resonance wavelengths at m=19 compared to the three force sensors they are replacing, which are $1563.724 \,nm$, $1575.268 \,nm$ and $1589.558 \,nm$ respectively. Three reference rings have been used instead of one to consider the varying temperature sensitivities at different wavelengths as shown in Figure 7.23. More of this will be explaiend in section 7.4.

The overlap probability (explained for the first time in subsection 6.2.2) of 31 ring resonators on a bus waveguide as describe above is shown in Figure 7.31. For this analysis similar to subsection 7.1.5, the waveguide cross-section is reduced to $410 \times 200 \, nm$ to take into account wafer-scale fabrication errors similar to the ones observed in section 6.2. In this case similar, the resonance wavelength standard deviation due to die-scale fabrication error is taken as $0.38 \, nm$, which is based on the values from Table 7.9. The FSR is $50 \, nm$ and the FWHM for each resonance peak is taken as $2 \cdot 35 \, pm$. A FWHM of $35 \, pm$ corresponds to sidewall scattering and absorption losses of $\approx 7 \, dB/cm$ (or Q = 46312 from Figure 7.17). The FWHM is also multiplied by 2 to consider the possible appearance of an extra resonance peak (resulted from resonance splitting) that can make the non-backscattered resonance peak appear less sharp due to the resonance peaks overlapping one another (The value of 2 is an estimated value that mimics a FWHM increase due to resonance splitting). Similar to subsection 6.2.2 and subsection 7.1.5, two resonance peaks are considered to be overlapped when the seperation distance between peaks is below $3 \cdot \Delta \lambda_{FWHM}$ and the amount of Monte-Carlo simulation is 10000. These parameters resulted in a probability of zero resonance peak overlaps of 74.29% and a 22.23% chance of a single overlap. Considering there are 31 resonance peaks in total, these statistics show it is likely that most if not all resonance peaks can be interrogated despite the die-scale waveguide fabrication errors.

The photonic integrated circuits will be fabricated from a $200 \, nm$ SOI-wafer with a top silicon layer thickness of $220 \, nm$ at Cornerstone using a photolithography machine with a KrF laser at $\lambda = 248 \, nm$. Cornerstone's process flow will be utilized [93], which is shown and explained in Appendix A. This process flow leaves a SiO_2 hard mask layer with a thickness of $180 \, nm$ on top of the silicon waveguide. The removal of this layer is left as a follow-up research.

After fabricating the photonic integrated circuit, both PDMS and Ormocore polymer thin film layers must

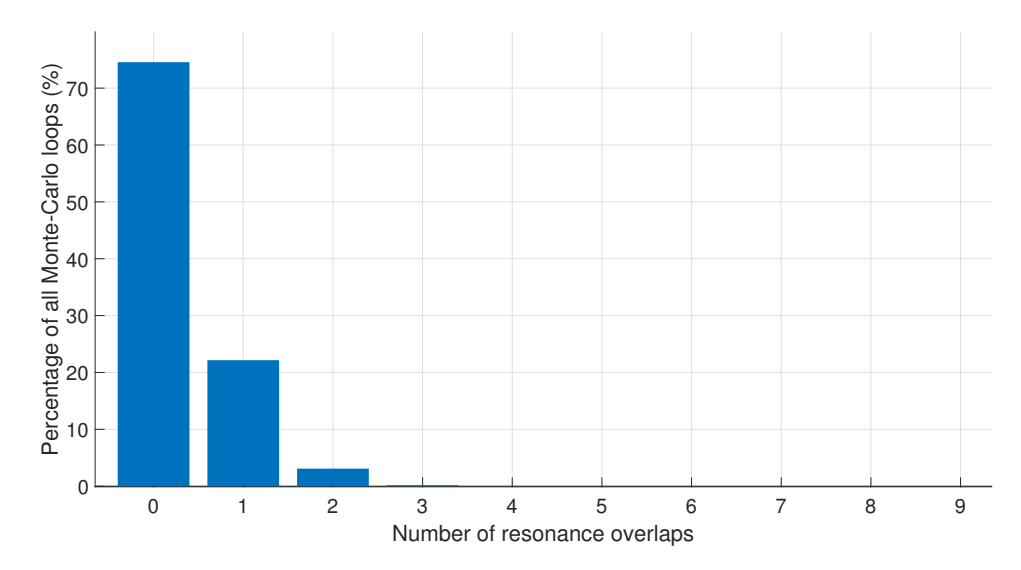


Figure 7.31: Resonance overlap percentage for multiplexed ring resonators with $2 \mu m$ radius and a cross-section of $410 \times 200 \, nm$.

be put on top of the chip covering the force and reference sensors respectively. The out-of-plane grating coupler will be cladded in air to ensure optimal coupling efficiency. A proposed process flow of thin polymer film layers on top of the photonic integrated circuit is shown in Appendix B.

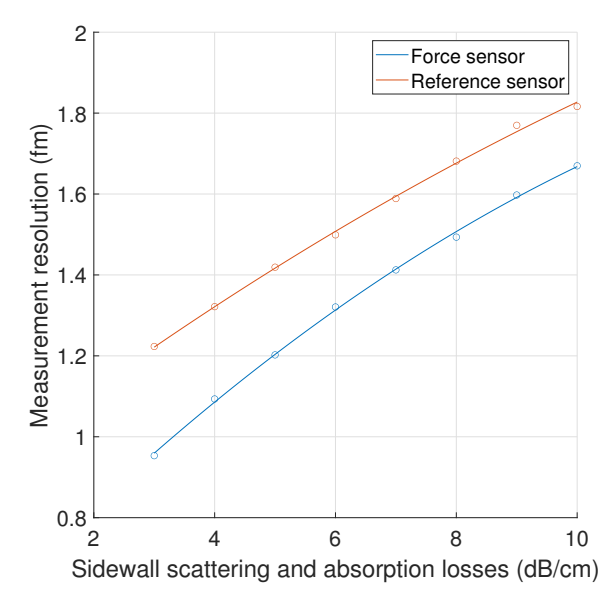
The microfabrication of these thin film layers starts by depositing the Ormocore resin on the entire chip using spin coating. The manufacturer states the possibility of spin coating Ormocore, while other deposition methods such as inkjet printing is not suitable due to Ormocore's high viscosity [103][104]. The high thermal stability of Ormocore (up to 270°C for a short term) allows it to withstand the PDMS curing process without degrading the material properties, as the curing process of PDMS does not exceed 90°C (T. Erdogan and W.J. Westerveld, personal communication, November 2, 2022). For this reason, Ormocore is deposited and UV cured before PDMS. Afterwards, a photoresist mask is deposited on top of the Ormocore resin with only the location of the reference ring resonators not being covered by the mask (similar to [105]). In this way, only the region of the reference ring resonators will be UV cured, while the resin on top of all the other parts of the chip gets washed away. The same process (spin coating, masking and UV curing) can also be done for PDMS, which is only possible if its viscosity is lowered by diluting PDMS with solvents first [106]. Due to the presence of Ormocore layer on the chip, the second spin coating process can locally accumulate near the Ormocore layer. This is not a problem as long as the PDMS layer thickness is uniform at the force sensors. To ensure this, the separation distance between both sensor type (i.e. X_{csd} from Figure 7.29) should be around hundred of microns such as $500 \,\mu m$ (T. Erdogan, W.J. Westerveld, personal communication, November 2, 2022). The exact required value of the component separation distance X_{csd} should be determined with experiments (as a follow-up research).

7.4 Interrogation Performance

In this section, the sensor interrogation performance of the $R=2\,\mu m$ ring resonator from section 7.2 will be discussed. The analysis from chapter 4 is included and expanded upon by adding the actual force sensing mechanics in the calculatios, allowing both the sensitivity and the limit-of-detection in terms of force to be determined. It has been described by Equation 4.1 that both the measurement resolution $(\Delta \lambda_{min})$ and the sensitivity are required to determine the limit-of-detection. The interrogation setup (and its noise values) as described in subsection 4.2.1 are used in the interrogation performance analysis of the $R=2\,\mu m$ ring resonator design as well.

As explained in section 4.1, the measurement resolution is caused by temperature drift, laser source wavelenght repeatability as well as intensity noise of the measurement setup. It has been observed from Monte-Carlo simulations in subsection 4.2.5 that the latter results in very low resonance wavelength fluctuations. The same can be said for both the force sensing and the reference ring resonator as shown in Figure 7.32.

Figure 7.32 shows the measurement resolution for sidewall scattering and absorption losses of 3 dB/cm to 10 dB/cm in the case of critical coupling using curve-fitting methods as described in subsection 4.2.2. The



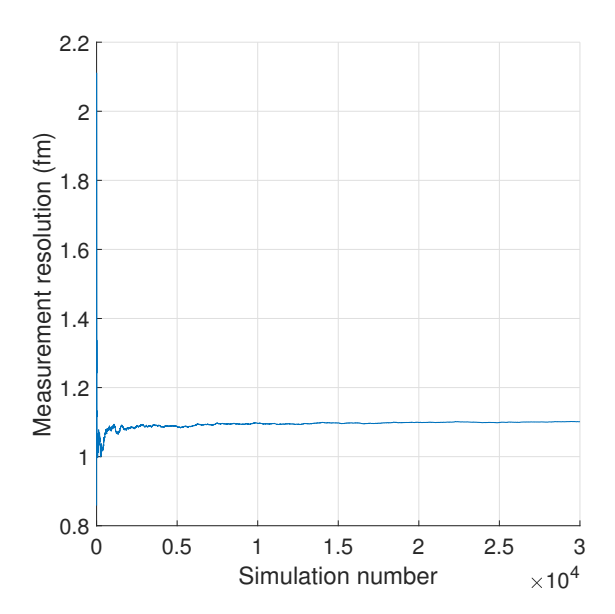


Figure 7.32: Intensity noise measurement resolution in Figure 7.33: Simulation convergence for 30000 Montethe case of critical coupling for varying sidewall scattering and absorption losses. Carlo simulations. At around 20000 iterations, the calculation does not give much more accurate results.

optical properties (e.g. n_{eff} , n_g and α) calculated in subsection 7.2.1 (and subsection 7.2.2 for the reference sensor with Ormocore cladding and a waveguide cross-section of $410 \times 220 \, nm$) have been used for this analysis. The maximum normalized intensity is 0.37, since this is the approximate lowest maximum intensity within the interrogation bandwidth of $\lambda = 1550 \, nm$ to $1600 \, nm$ due to the grating coupler losses (as shown in e.g. Figure 6.2). For this study, the amount of Monte-Carlo simulations is increased from 1000 to 20000. Although 1000 simulations do give an approximate answer, more simulations are required to obtain a better convergence as shown in Figure 7.33. The measurement resolution remains between $1 \, fm$ and $2 \, fm$ with higher propagation losses resulting in larger measurement resolutions as shown in Figure 7.32. At sidewall scattering and absorption loss of $10 \, dB/cm$, the measurement resolution of the force and reference sensors are $1.67 \, fm$ and $1.82 \, fm$ respectively. Adding these up result in a combined measurement resolution of roughly $3.5 \, fm$. The reason for considering the intensity noise of both sensor types is because both total resonance wavelength shifts (i.e. $\Delta \lambda_{sense,tot}$ and $\Delta \lambda_{ref,tot}$) are subtracted from each other in Equation 5.25. As a result, the noise values may potentially add up in the process.

According to Equation 5.25, the wavelength repeatability term $\Delta \lambda_{WLR}$ can only be cancelled out if the temperature sensitivities of both the force and the reference sensors are exactly the same. For example, it has been shown in subsection 7.2.2 that the temperature sensitivities are $S_{T,force} = -27.20 \, pm/K$ and $S_{T,ref} = -27.51 \, pm/K$ respectively. This causes uncertainty in determining the resonance wavelength (that is the measurement resolution), which can be described by rewriting Equation 5.25.

$$\Delta \lambda_{sense,force} = \left[\Delta \lambda_{sense,tot} - \frac{\left(\frac{\partial \lambda}{\partial T}\right)_{sense}}{\left(\frac{\partial \lambda}{\partial T}\right)_{ref}} \Delta \lambda_{ref,tot} \right] + \left[\Delta \lambda_{WLR} \left(\frac{\left(\frac{\partial \lambda}{\partial T}\right)_{sense}}{\left(\frac{\partial \lambda}{\partial T}\right)_{ref}} - 1 \right) \right]$$
(7.1)

The left square bracket component represents the temperature drift cancellation without considering the wavelength repeatability, which exactly describes Equation 5.22. On the other hand, the square bracket component on the right-hand side represents the resonance wavelength error (or the measurement resolution $\Delta \lambda_{min}$) caused by the wavelength repeatabilty. This is shown in Equation 7.2

$$\Delta \lambda_{min} = \left| \Delta \lambda_{WLR} \left(\frac{\left(\frac{\partial \lambda}{\partial T} \right)_{sense}}{\left(\frac{\partial \lambda}{\partial T} \right)_{ref}} - 1 \right) \right|$$
 (7.2)

If the temperature sensitivities of both sensor types are not equal, then $\Delta \lambda_{min}$ will not become equal to zero. Since there are 28 force sensors with slightly different radii on a single bus waveguide as shown in section 7.3, a few reference ring resonators cannot have the same temperature sensitivities compared to all these 28 force sensors to cancel out the wavelength repeatability. As shown in section 7.3, three reference ring resonators with resonance peaks at $1563.724\,nm$, $1575.268\,nm$ and $1589.558\,nm$ have been used to determine temperature

sensitivities at other wavelengths as well by curve-fitting. This is shown in Figure 7.34 and Figure 7.35. It should be noted beforehand that this method of determining temperature sensitivities at different wavelengths is a concept demonstration in which the temperature drifts ΔT for all the temperature sensitivity calculations are assumed to be very small as explained in section 5.5. Additional analysis is required to determine the temperature sensitivities changes at larger ΔT and resonance wavelength shifts ($\Delta \lambda_{m=19}$).

The temperature sensitivities of the three reference ring resonators with radii of $2.000 \,\mu m$, $2.024 \,\mu m$ and $2.054 \,\mu m$ at the three aforementioned resonance wavelenghts are $-28.49 \,pm/K$, $-29.30 \,pm/K$ and $-30.27 \,pm/K$ respectively, calculated using the steps described in section 5.5. Figure 7.34 and Figure 7.35 show the relation between temperature sensitivities and both the ring resonator radius as well as the resonance wavelength can be described by a second-order polynomial function. The errors of the curve-fit are within the magnitude of $10^{-14} \, pm/K$ to $10^{-13} \, pm/K$, which is small considering the temperature sensitivities are around $-29 \, pm/K$. The green dot from Figure 7.34 and Figure 7.35 represents the temperature sensitivity of the first force sensor of the bus waveguide (with $R_1 = 1.949 \,\mu m$ and $\lambda_{m=19} = 1553.167 \,nm$), which is equal to $-27.59 \,pm/K$. By using the polynomial function used for curve-fitting, both the resonance wavelength and the reference ring resonator radius at which the reference temperature sensitivity is theoretically equal to the one of the force sensing ring resonator (i.e. $-27.59 \, pm/K$) can be calculated by extrapolation (denoted by the black dot). In this case, the extrapolated radius and resonance wavelength is $R = 1.974 \,\mu m$ and $\lambda_{m=19} = 1551.144 \,nm$ respectively. Using the calculation steps described in section 5.2 and section 5.5 and taking a reference ring resonator radius of $R = 1.974 \,\mu m$, the resonance wavelength at m = 19 is $1551.135 \,nm$ and the temperature sensitivity is equal to $-27.70 \, pm/K$ instead. This indicates that the temperature sensitivities are not exactly equal to each other despite what the curve-fitting and extrapolation results show in e.g. Figure 7.34.

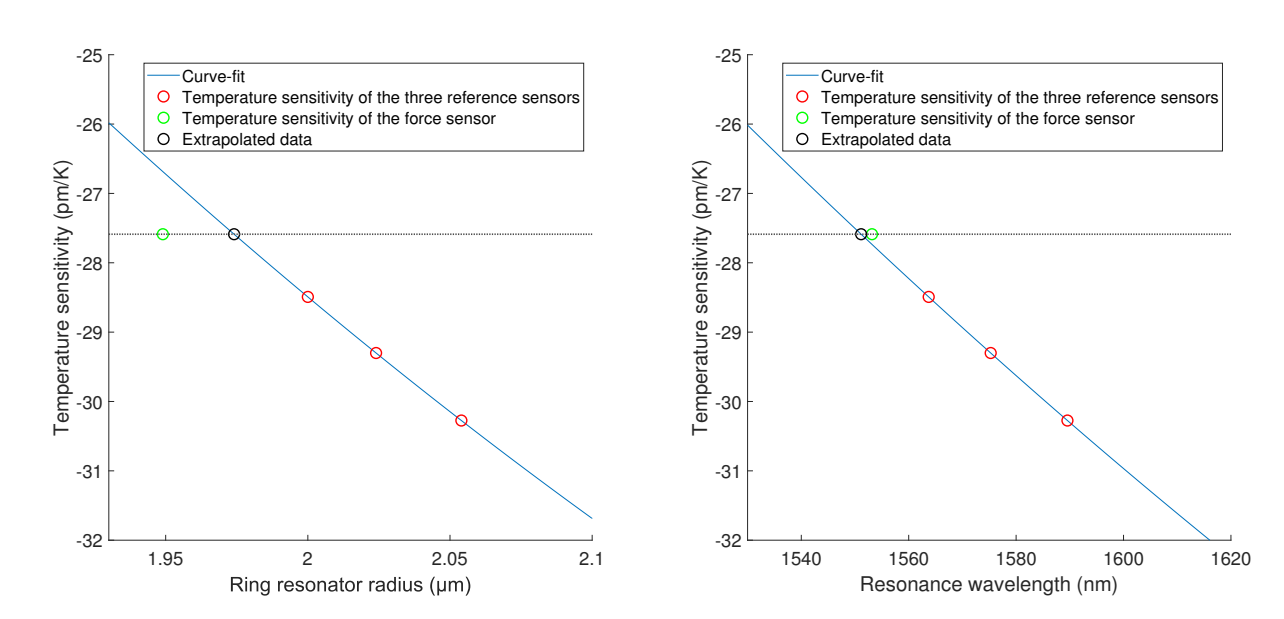


Figure 7.34: Temperature sensitivities at different ring Figure 7.35: Temperature sensitivities at different resresonator radii. Here, the temperature sensitivities onance wavelengths (which depends on the ring resholds for temperature drifts ΔT being very small. onator radius and ΔT being very small in this case)

In practice, a plot similar to Figure 7.34 and Figure 7.35 can be made by characterizing the fabricated photonic integrated circuit. This is in order to determine (by interpolating or extrapolating the data points of the three reference ring resonators) at which resonance wavelength ($\lambda_{res,ref}$) the reference temperature sensitivity is theoretically equal to the one of a force sensing ring resonator at a certain resonance wavelength ($\lambda_{res,sense}$). The resonance wavelength shift of the force sensor from $\lambda_{res,sense}$ can be directly measured from the data obtained by the photoreceiver. In order to determine the theoretical resonance wavelength shift from $\lambda_{res,ref}$, the resonance wavelength shifts of the three reference sensors must be determined and interpolated or extrapolated at e.g. $R = 1.974 \,\mu m$ (which is the theoretical reference ring resonator radius at which both temperature sensitivities are equal). After obtaining both resonance wavelength shifts ($\Delta \lambda_{sense,tot}$ and $\Delta \lambda_{ref,tot}$) and knowing the temperature sensitivity of both ring resonator types, Equation 5.25 can be used to filter out the temperature drift and wavelength repeatability induced noise and determine the resonance wavelength shift due to the exerted force only.

In Table 7.10, the measurement resolution resulting from the wavelength repeatabilities for four different

cases are shown. The first two cases correspond to the comparison between the temperature sensitivity of the aforementioned force sensing ring resonator $(R = 1.949 \,\mu m, \, \lambda_{m=19} = 1553.167 \,nm)$ of $-27.59 \,pm/K$ with the one of the extrapolated data of $-27.70 \,pm/K$. The temperature sensitivity of the same force sensing ring resonator has also been compared to the reference temperature sensitivity of the first reference ring resonator $(R = 2.000 \,\mu m, \, \lambda_{m=19} = 1563.724 \,nm)$ of $-28.49 \,pm/K$ to analyze the measurement resolution in a more pessimistic scenario (i.e. a scenario where both temperature sensitivities are noticably different from one another).

It is shown in Table 7.10 that the measurement resolution ranges from 0.012 pm to 0.508 pm, depending on the case. It can be seen that the contribution of the wavelength repeatability to the measurement resolution is much larger than the combined contribution of the force and reference sensor intensity noise of 3.5 fm (at sidewall scattering and absorption loss of 10 dB/cm) as shown in Figure 7.32.

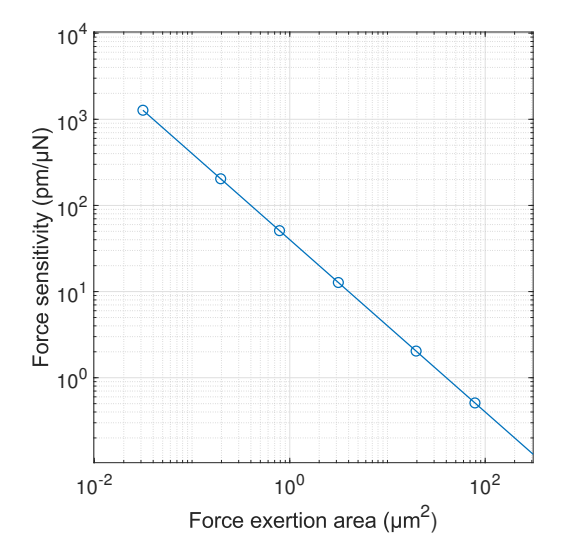
$ \frac{\left(\frac{\partial \lambda}{\partial T}\right)_{force}}{(pm/K)} $	$\left(\frac{\partial \lambda}{\partial T}\right)_{ref} \ (pm/K)$	$\Delta \lambda_{WLR} \ (pm)$	$\Delta \lambda_{min} \ (pm)$	Notes
-27.59	-27.70	±8.0	0.067	Temperature sensitivity of the extrapolated data
-27.59	-27.70	± 1.5	0.012	Temperature sensitivity of the extrapolated data
-27.59	-28.49	± 8.0	0.508	Temperature sensitivity of the first reference ring resonator.
-27.59	-28.49	± 1.5	0.095	Temperature sensitivity of the first reference ring resonator.

Table 7.10: Measurement resolution caused by the wavelength repeatability for different cases. Wavelength repeatabilities of $\pm 8.0 \, pm$ and $\pm 1.5 \, pm$ correspond to Santec TSL-570 type A and C respectively [87]

The sensitivity of the aforementioned force sensing ring resonator (with $R=1.949\,\mu m$ and $\lambda_{m=19}=1553.167\,nm$) is $65.41\,nm/RIU$ (calculated using the steps described in section 5.3). In order to determine the sensitivity in terms of force, Equation 3.3 must be expanded by including a coefficient that relates the change in the cladding refractive index to the force applied to it, resulting in Equation 7.3.

$$S_f \equiv \frac{\partial \lambda_m}{\partial F} = \frac{\lambda_c}{n_g} \frac{\partial n_e}{\partial n_{clad}} \frac{\partial n_{clad}}{\partial F}$$
 (7.3)

A study has been carried out that obtained a stress-optic coefficient for PDMS film layer at the bottom surface of $612\,RIU/TPa$ [107]. This value can be used to determine $\partial n_{clad}/\partial F$ from Equation 7.3 and subsequently $\partial \lambda_m/\partial F$ for varying force exertion area as shown in Figure 7.36. For a ring resonator without any fabrication errors, the sensitivity decreases from $1274.25\,pm/\mu N$ to $0.127425\,pm/\mu N$ for an increasing circular area with a radius of $0.1\,\mu m$ to $10\,\mu m$ respectively. This is also shown in Figure 7.36.



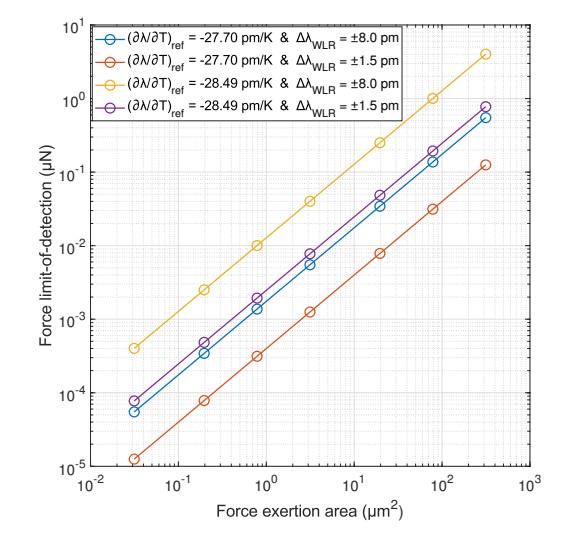


Figure 7.36: Force sensitivities for different force exer- Figure 7.37: Force limit-of-detection for different force tion areas.

In Figure 7.37, the force limits-of-detection are shown for the four different cases from Table 7.10. The sensitivity of the aforementioned force sensing ring resonator $(R=1.949\,\mu m$ and $\lambda_{m=19}=1553.167\,nm)$ in all four cases are $65.41\,nm/RIU$, while the measurement resolutions from Table 7.10 plus the intensity noise contribution of both the force sensor as well as the reference sensor of $3.5\,fm$ (from Figure 7.32) are taken. It can be seen that the force limit-of-detection remain well below $1\,\mu N$ for the most part. In the best case scenario (i.e. the dark orange line from Figure 7.37), the force limit-of-detection approaches $10\,pN$. However in practice, the fabrication errors may cause larger curve-fit errors than the ones mentioned in $10^{-14}\,pm/K$ to $10^{-13}\,pm/K$, which could result in larger measurement resolutions and force limits-of-detection. However, the extend of this analyzing this error is left as a follow-up research.

Finally, the force distribution over the force exertion areas is assumed to be uniform in this analysis. As a follow-up research, the actual force exertion distribution of biological cells should be analyzed to obtain a more accurate force sensitivity.

Chapter 8

Discussion

8.1 Fabrication Error Analysis

The different fabrication errors discussed in chapter 6 that can result in resonance wavelength, Q-factor and propagation loss are analyzed from a silicon photonic integrated circuit with air cladding as well as a SiO_2 hard mask layer with a thickness of $180\,nm$ on top of the waveguide that has not been removed yet. However, the ring resonators of the distributed force sensor are either cladded in PDMS or Ormocore instead. The refractive indices of these polymer claddings are different than the one of air, meaning the magnitude of sidewall scattering, absorption loss, and the resonance wavelength deviations due to die-scale waveguide width nonuniformity will differ. In the case of the $R=2\,\mu m$ ring resonator design, the radius is also decreased from $R=5\,\mu m$. In other words, the fabrication error analysis performed in chapter 6 is device specific. Nevertheless, the fabrication error induced propagation losses and spectral deviations data obtained in chapter 6 are considered for the distributed force sensor. The reason for this is that these data can still provide some idea of how the distributed force sensor can perform differently due to fabrication errors. It can be assumed that in practice the polymer claddings of the distributed force sensor result in lower sidewall scattering (due to the lower refractive index contrast ratio), but also cause higher absorption losses.

It should also be noted that the effects of fabrication errors (both at wafer-scale as well as at die-scale) are analyzed at a wavelength of $\lambda = 1550 \, nm$ only. The effects of fabrication error will differ at different wavelengths and for varying radii. Analyzing it solely at $\lambda = 1550 \, nm$ can still give an insight of the fabrication error effects.

Finally, the curve-fitting of measured data as described in section 6.3 show some error in e.g. the fitted resonance wavelength, lowest intensity or FWHM due to the noisy signals coming from the measurements. This can affect the sidewall scattering and absorption losses that are calculated in that section.

8.2 Intrinsic Ring Resonator Performance

In chapter 7, ring resonators with radii of both $5\,\mu m$ and $2\,\mu m$ have been analyzed. A $R=2\,\mu m$ small ring resonator needs to be designed, since one of the requirements states that the sensor seperation distance should not exceed $10\,\mu m$. On the other hand, a $R=5\,\mu m$ is also analyzed to test out the multiplexibility and the temperature compensation method by proposed in subsection 5.5.4 with ring resonators that have been characterized already by W-Lab.

The cladding material properties of the reference ring resonator design used for simulations are either manufacturer specifications or measurements of a third party. Although these data give an idea what material property values to expect, the actual values may differ in practice. This can result in e.g. different required adjusted reference ring resonator waveguide width for temperature sensitivity equalization.

For coupling FDTD simulations, integral monitors have been placed at both the output of the bus waveguide as well as the output of the ring resonator (see Figure 5.3). The reason for this is to analyze the magnitude of the additional intensity loss during the coupling process. If the extra intensity loss $1-\tau^2-\kappa^2$ is large relatively to the coupling κ^2 , then the real transmission coefficient is somewhere between $\sqrt{\tau^2}$ and $\sqrt{1-\kappa^2}$, because the latter calculation also includes the radiation loss (since the monitor is placed far away from the coupling gap in order for it to be aligned with the grid).

8.3 Interrogation Performance

The addition of three reference ring resonators increases the measurement resolution by cancelling out the temperature drift as shown in section 7.4. Although the minimum amount to describe a second-order polynomial function is three data points, in practice due to fabrication errors, using more than three reference ring resonators may result in a more accurate description of the curve. The minimization of curve-fitting errors can result in smaller measurement resolutions.

The coefficient that describes the relation between the exerted force and the refractive index change of PDMS is determined by Park et al. [107]. The stress-optic coefficient of a $10\,\mu m$ thick PDMS film layer is taken for this assignment, which is the thinnest film layer analyzed by Park et al. No definitive PDMS film thickness has been defined in this thesis. Therefore, it should be taken into account that this stress-optic coefficient can vary if a different film layer thickness will be chosen in the follow-up research. Also, the refractive index of the unloaded PDMS film is approximately 1.42, which is higher than the one used for the simulations in chapter 7. The reason for this could be that the PDMS types are different from each other (due to e.g. difference in mass ratio between main agent and curing agent [90]). Despite the (potential) material property differences, the stress-optic coefficient of $612\,RIU/TPa$ can still provide an idea of how large the force sensitivity and how small the minimum detectable force is.

Also, the temperature sensitivity simulations described in subsection 5.5.2 consider both changes of refractive indices due to temperature change as well as changes in waveguide cross-sectional dimensions due to thermal expansion, with the latter's contribution being very small in comparison. However, both PDMS and Ormocer or Ormocore will also expand due to temperature changes which can also influence the effective refractive index. This has not been taken into account in this thesis. As a follow-up research, the contribution of the thermal expansion of these polymer claddings to the overall change of effective refractive index could be analyzed.

Figure 7.32 shows that the propagation loss of the ring resonator have little influence on the intensity noise measurement resolution, as long as it is critically coupled. Even for $\alpha_{swa}[dB/cm] = 10\,dB/cm$, the minimum detectable wavelength shift $(\Delta\lambda_{min})$ stays much smaller than the ones caused by the wavelength repeatability (as shown in Table 7.10). The reason for this is the high signal-to-noise ratio used for this analysis. The standard intensity deviation is $\delta P_{stdev} = 44.49\,nW$ while the laser input power equal to the photodetector saturation power is $55\,\mu W$ (Both values are presented in subsection 4.2.1). If the signal-to-noise ratio decreases, measurement resolution $\Delta\lambda_{min}$ is expected to increase.

Finally, the force exertion distribution on the sensor is assumed to be uniform over an area. In practice, this may not be the case for biological cells, resulting in less accurate force sensitivity results.

8.4 Distributed Force Sensor Design

The sensor design shown in Figure 7.29 has 28 bus waveguides placed parallel from each other. Each bus waveguide contains 31 ring resonators and its own grating couplers. This allows each 31 multiplexed ring resonators on a bus to be interrogated seperately, which is one of the design requirements (see section 1.3).

The resonance peak placement of the distributed force sensor design as described in section 7.3 is done by varying the ring resonator radii for waveguides without any fabrication errors (i.e. $450 \times 220 \, nm$ cross-section and a $100 \, nm$ slab height). Due to fabrication errors, both the FSR and the resonance wavelengths can change, which results in overlap probabilities that are different than the one from Figure 7.31.

8.5 Sensor Fabrication

The CMOS fabrication processes defined by Cornerstone are used to fabricate the photonic integrated circuit. This leaves a hard SiO_2 mask on top of the waveguides, which must be removed to prevent sensitivity decrease of the ring resonators. Also, the proposed polymer resin deposition and UV curing processes described in section 7.3 are general steps that show the possibility of having multiple types of polymer film layers on top of a single chip. However, the required fabrication parameters should be determined in a follow-up research. This process flow can also be adjusted as long as the final results are the same. For example, inkjet printing or spray coating are also promising options to locally deposit PDMS instead of spin coating [104]. These two deposition methods do not have the "local PDMS accumulation issue" as explained in section 7.3, since the material deposition happens locally. The reason why spin coating has been presented instead in section 7.3 is because this deposition process has been successfully carried out by W-Lab before.

Chapter 9

Conclusion and Outlook

9.1 Conclusion

From the literature review, it was concluded that silicon material platform, strip waveguides, ring or disk resonators and reference sensor for temperature drift compensation were the most suitable sensor design choices. Due to silicon's high refractive index, the mode field gets more confined compared to other material platforms. This makes small waveguide bends with low radiation losses possible, which is crucial for designing small sized integrated photonic sensors. For the same reason, the strip waveguide is also the most ideal waveguide cross-section geometry. Furthermore, both ring and disk resonators can be used to make small and fabrication error robust sensors compared to the other options. The reference sensor is the only option that can potentially cancel out both the temperature drift and the wavelength repeatability of the laser.

Ring resonators with radii of both $5\,\mu m$ and $2\,\mu m$ have been analyzed. For both ring resonators, a PDMS cladding layer is fabricating on top it, which allows cell exerted forces to be measured. This is done by detecting PDMS refractive index changes due to the induced strain in the PDMS layer caused by exerted cell forces. Therefore, the second requirement from section 1.3 has been satisfied. The $R=2\,\mu m$ has an inner slab layer with a thickness of $100\,nm$ to further reduce the radiation loss. Both sensors show resonance peaks with Q-factors of Q>20000), which include contributions of sidewall scattering and absorption losses defined in a seperate fabrication error analysis. The coupling gap of $200\,nm$ (and perhaps $250\,nm$) is required in order to potentially critical couple the ring resonators while taking into account the extra intensity losses (during the coupling process) determined in the same fabrication error analysis. The reference ring width should be $370\,nm$ and $410\,nm$ for the $R=5\,\mu m$ and $R=2\,\mu m$ ring resonator respectively in order to equalize the temperature sensitivity of both the reference and the force ring resonator (this is neccessary to minimize measurement error caused by the wavelength repeatability of the laser). A commercial hybrid-polymer (Ormocore for $R=2\,\mu m$ reference ring resonators) is used with a Young's modulus of around $1\,GPa$ to shield the reference ring resonator from the forces exerted by the biological cells.

The interrogation performance analysis of the $R=2\,\mu m$ sensor designs shows that the measurement resolution is mainly determined by the wavelength repeatability of the laser. Having three reference ring resonators with adjusted waveguide widths and being cladded in Ormocore, the measurement resolution can be potentially decreased to $0.012\,pm$. These three reference ring resonators are put on a single bus in order to determine the variation of the reference temperature sensitivities at different wavelengths.

Using a stress-optic coefficient of $612\,RIU/TPa$, the force limit-of-detection remains well below $1\,\mu N$ (even with waveguide cross-sectional dimension errors) as long as the force exertion area does not exceed around $80\,\mu m^2$. This indicates the possibility of sensing submicronewton level of forces using the designed force sensor, satisfying the first requirement of section 1.3.

The distributed force sensor array is 28×28 with a seperation distance of around $8 \mu m$ in both the horizontal and vertical direction and a radius of around $2 \mu m$, satisfying the third requirement of section 1.3. This also means the biological cell that is $80 \times 80 \mu m$ in size can be completely covered by the sensor array. The resonance peaks of the 28 force sensors and three reference sensors on a single bus waveguide can be simultaneously interrogated, which satisfies the fourth requirement of section 1.3. The probability of one or more resonance peak overlap is 25.71%.

The photonic integrated circuit (and its waveguide dimensions) can be fabricated at Cornerstone using their own defined CMOS fabrication processes, satisfying the fifth requirement of section 1.3. Subsequently, polymer resins can be deposited and UV cured to create PDMS force sensing layer as well as an Ormocore reference force shield on a single chip.

9.2 Outlook

This thesis focusses on the theoretical part of designing a integrated photonic distributed force sensor which can be used to measure forces exerted by biological cells. However, experimental characterization of integrated photonic components and materials are required to better understand its properties and adjust the design accordingly.

First of all, the ring resonator design from section 7.2 has to be fabricated (including the polymer claddings) and its Q-factor, (temperature) sensitivity, free spectral range resonance wavelengths as well as the coupling gap required for critical coupling must be determined and compared with the simulation results from this thesis. Experimentally characterizing the temperature sensitivities of both the force and reference sensors (at different wavelengths) is essential to ensure small measurement resolution as described in section 7.4. In practice, the temperature sensitivities could be different, meaning the required adjusted waveguide width for temperature sensitivity equalization will be different compared to $w_{ref} = 410 \, nm$ which was calculated in subsection 7.2.2. Additionally, as mentioned in section 5.5, the temperature sensitivity calculation only holds for small temperature drifts, since the temperature sensitivity changes when the resonance wavelength shifts due to temperature changes. The resonance wavelength shifts over large temperature drifts should be analyzed as well.

Also, multiple ring resonators with slightly different radii have to be multiplexed on the same bus waveguide in order to test the resonance peak overlap probability. In this thesis, 31 ring resonators have been multiplexed on a ring resonator with a resonance seperation of $1.452\,nm$. Assuming a ring resonator center-to-center seperation of $10\,\mu m$ as mentioned in section 7.3, this amount of ring resonators is sufficient to cover the entire $80\times80\,\mu m$ biological cell size while keeping a low resonance peak overlap probability. It is possible to further increase the amount of multiplexed ring resonators in order to get a larger force sensor array by allowing more resonance peak overlaps than what is shown in Figure 7.31. The maximum allowable resonance peak overlaps should also be determined as a follow-up research.

After characterizing the photonics part, the force sensing capabilities of the distributed force sensor needs to be determined either numerically, experimentally or both. The required cladding layer thickness for both polymers that gives desired results (i.e. high and low sensitivity for PDMS and Ormocore respectively) must be determined. Other material properties such as the (measured) refractive indices and TOC's need to be found out as well. Furthermore, the contribution of the thermal expansion of both PDMS and Ormocore claddings could be determined as mentioned in section 8.3.

The biological cell force exertion distribution should also be determined to get an more accurate force sensitivity results of the distributed force sensor. In section 7.4, the force exertion is assumed to be uniform over an area, which may not be accurate.

Besides experimental characterization, extra attention to the fabrication of the distributed force sensor needs to be paid as well. The CMOS fabrication process defined by Cornerstone to manufacture the photonic integrated circuits involves using SiO_2 hard masks. This $180\,nm$ thick mask layer will not be removed during their fabrication process. It is important to remove this hard mask in order for the ring resonators to have high sensitivities. As for fabricating polymer claddings which has been explained in section 7.3, the necessary fabrication parameters and materials as well as the required seperation distance x_{csd} between the force and reference sensors (to prevent excessive PDMS accumulation on top of the force sensors) need to be determined as follow-up research.

Finally, the multi-mode propagation in waveguides has not been analyzed in this thesis. This can occur due to the slab layer inside the ring resonator that allows mode fields to propagate similar to a disk waveguide, It has been observed that small ring and disk resonators show single mode propagation due to the higher order modes being suppressed by extra radiation losses resulted from small waveguide bends [108][109] As a follow-up research, the possibility of multi-mode propagation should be determined using both simulations and experiments.

Bibliography

- [1] De Vos, Katrien, "Label-free silicon photonics biosensor platform with microring resonators," Ph.D. dissertation, Ghent University, 2010.
- [2] S. J. Callens, R. J. Uyttendaele, L. E. Fratila-Apachitei, and A. A. Zadpoor, "Substrate curvature as a cue to guide spatiotemporal cell and tissue organization," *Biomaterials*, vol. 232, p. 119739, 2020. [Online]. Available: https://www.sciencedirect.com/science/article/pii/S0142961219308579
- [3] E. C. Yusko and C. L. Asbury, "Force is a signal that cells cannot ignore," *Molecular Biology of the Cell*, vol. 25, no. 23, pp. 3717–3725, 2014, pMID: 25394814. [Online]. Available: https://doi.org/10.1091/mbc.e13-12-0707
- [4] P. Roca-Cusachs, V. Conte, and X. Trepat, "Quantifying forces in cell biology," *Nature cell biology*, vol. 19, no. 7, pp. 742–751, 2017.
- [5] U. S. Schwarz and J. R. Soiné, "Traction force microscopy on soft elastic substrates: A guide to recent computational advances," *Biochimica et Biophysica Acta (BBA)-Molecular Cell Research*, vol. 1853, no. 11, pp. 3095–3104, 2015.
- [6] J. L. Tan, J. Tien, D. M. Pirone, D. S. Gray, K. Bhadriraju, and C. S. Chen, "Cells lying on a bed of microneedles: an approach to isolate mechanical force," *Proceedings of the National Academy of Sciences*, vol. 100, no. 4, pp. 1484–1489, 2003.
- [7] A. V. Taubenberger, D. W. Hutmacher, and D. J. Muller, "Single-cell force spectroscopy, an emerging tool to quantify cell adhesion to biomaterials," *Tissue Engineering Part B: Reviews*, vol. 20, no. 1, pp. 40–55, 2014.
- [8] W. J. Polacheck and C. S. Chen, "Measuring cell-generated forces: a guide to the available tools," *Nature Methods*, vol. 13, no. 5, pp. 415–423, May 2016. [Online]. Available: https://doi.org/10.1038/nmeth.3834
- [9] Y. Amemiya, Y. Tanushi, T. Tokunaga, and S. Yokoyama, "Photoelastic effect in silicon ring resonators," *Japanese journal of applied physics*, vol. 47, no. 4S, p. 2910, 2008.
- [10] X. Zhao, J. Tsai, H. Cai, X. Ji, J. Zhou, M. Bao, Y. Huang, D. Kwong, and A. Q. Liu, "A nano-opto-mechanical pressure sensor via ring resonator," Optics Express, vol. 20, no. 8, pp. 8535–8542, 2012.
- [11] X. Liu, W. Liu, Z. Ren, Y. Ma, B. Dong, G. Zhou, and C. Lee, "Progress of optomechanical micro/nano sensors: a review," *International Journal of Optomechatronics*, vol. 15, no. 1, pp. 120–159, 2021.
- [12] L. K. Chin, Y. Shi, and A.-Q. Liu, "Optical forces in silicon nanophotonics and optomechanical systems: science and applications," *Advanced Devices & Instrumentation*, vol. 2020, 2020.
- [13] C. Lee and J. Thillaigovindan, "Optical nanomechanical sensor using a silicon photonic crystal cantilever embedded with a nanocavity resonator," *Applied optics*, vol. 48, no. 10, pp. 1797–1803, 2009.
- [14] W. J. Westerveld and H. P. Urbach, *Silicon Photonics*, ser. 2053-2563. IOP Publishing, 2017. [Online]. Available: https://dx.doi.org/10.1088/978-0-7503-1386-5
- [15] W. J. Westerveld, S. M. Leinders, K. W. A. van Dongen, H. P. Urbach, and M. Yousefi, "Extension of marcatili's analytical approach for rectangular silicon optical waveguides," *Journal of Lightwave Technology*, vol. 30, no. 14, pp. 2388–2401, 2012.
- [16] The Basics of Guided Waves. John Wiley & Sons, Ltd, 2004, ch. 2, pp. 11–36. [Online]. Available: https://onlinelibrary.wiley.com/doi/abs/10.1002/0470014180.ch2

- [17] E. A. J. Marcatili, "Dielectric rectangular waveguide and directional coupler for integrated optics," *Bell System Technical Journal*, vol. 48, no. 7, pp. 2071–2102, 1969. [Online]. Available: https://onlinelibrary.wiley.com/doi/abs/10.1002/j.1538-7305.1969.tb01166.x
- [18] C. Yeh and F. I. Shimabukuro, The essence of dielectric waveguides. Springer, 2008.
- [19] "Westerveld w j 2013 rectwg: Matlab implementation of the extended marcatili approaches for rectangular silicon optical waveguides (free open-source software). distributed in *RECTWG package for Matlab—Version 0.1*. delft university of technology," https://waveguide.sourceforge.net/index.html.
- [20] Q. Xu, D. Fattal, and R. G. Beausoleil, "Silicon microring resonators with 1.5-μm radius," Optics express, vol. 16, no. 6, pp. 4309–4315, 2008.
- [21] D. J. Blumenthal, R. Heideman, D. Geuzebroek, A. Leinse, and C. Roeloffzen, "Silicon nitride in silicon photonics," *Proceedings of the IEEE*, vol. 106, no. 12, pp. 2209–2231, 2018.
- [22] A. Rahim, E. Ryckeboer, A. Z. Subramanian, S. Clemmen, B. Kuyken, A. Dhakal, A. Raza, A. Hermans, M. Muneeb, S. Dhoore et al., "Expanding the silicon photonics portfolio with silicon nitride photonic integrated circuits," *Journal of lightwave technology*, vol. 35, no. 4, pp. 639-649, 2017.
- [23] R. Heideman, M. Hoekman, and E. Schreuder, "Triplex-based integrated optical ring resonators for labon-a-chip and environmental detection," *IEEE Journal of Selected topics in quantum electronics*, vol. 18, no. 5, pp. 1583–1596, 2012.
- [24] M. Smit, X. Leijtens, H. Ambrosius, E. Bente, J. Van der Tol, B. Smalbrugge, T. De Vries, E.-J. Geluk, J. Bolk, R. Van Veldhoven et al., "An introduction to inp-based generic integration technology," Semiconductor Science and Technology, vol. 29, no. 8, p. 083001, 2014.
- [25] S. Zou, F. Wang, R. Liang, L. Xiao, and M. Hu, "A nanoscale refractive index sensor based on asymmetric plasmonic waveguide with a ring resonator: A review," *IEEE Sensors Journal*, vol. 15, no. 2, pp. 646–650, 2014.
- [26] A. Dolatabady, N. Granpayeh, and V. F. Nezhad, "A nanoscale refractive index sensor in two dimensional plasmonic waveguide with nanodisk resonator," *Optics Communications*, vol. 300, pp. 265–268, 2013.
- [27] M. Hochberg, T. Baehr-Jones, C. Walker, and A. Scherer, "Integrated plasmon and dielectric waveguides," *Optics express*, vol. 12, no. 22, pp. 5481–5486, 2004.
- [28] G. Dabos, A. Manolis, D. Tsiokos, D. Ketzaki, E. Chatzianagnostou, L. Markey, D. Rusakov, J.-C. Weeber, A. Dereux, A.-L. Giesecke et al., "Aluminum plasmonic waveguides co-integrated with si3n4 photonics using cmos processes," Scientific reports, vol. 8, no. 1, pp. 1–10, 2018.
- [29] S. K. Selvaraja, W. Bogaerts, and D. Van Thourhout, "Loss reduction in silicon nanophotonic waveguide micro-bends through etch profile improvement," *Optics Communications*, vol. 284, no. 8, pp. 2141–2144, 2011. [Online]. Available: https://www.sciencedirect.com/science/article/pii/S0030401811000046
- [30] W. Bogaerts, P. De Heyn, T. Van Vaerenbergh, K. De Vos, S. Kumar Selvaraja, T. Claes, P. Dumon, P. Bienstman, D. Van Thourhout, and R. Baets, "Silicon microring resonators," *Laser & Photonics Reviews*, vol. 6, no. 1, pp. 47–73, 2012. [Online]. Available: https://onlinelibrary.wiley.com/doi/abs/10.1002/lpor.201100017
- [31] Silicon-On-Insulator (SOI) Photonics. John Wiley & Sons, Ltd, 2004, ch. 4, pp. 57–110. [Online]. Available: https://onlinelibrary.wiley.com/doi/abs/10.1002/0470014180.ch4
- [32] S. T. Fard, V. Donzella, S. A. Schmidt, J. Flueckiger, S. M. Grist, P. T. Fard, Y. Wu, R. J. Bojko, E. Kwok, N. A. F. Jaeger, D. M. Ratner, and L. Chrostowski, "Performance of ultra-thin soi-based resonators for sensing applications," *Opt. Express*, vol. 22, no. 12, pp. 14166–14179, Jun 2014. [Online]. Available: https://opg.optica.org/oe/abstract.cfm?URI=oe-22-12-14166
- [33] A. Splett and K. Petermann, "Low loss single-mode optical waveguides with large cross-section in standard epitaxial silicon," *IEEE Photonics Technology Letters*, vol. 6, no. 3, pp. 425–427, 1994.
- [34] L. Vivien, F. Grillot, E. Cassan, D. Pascal, S. Lardenois, A. Lupu, S. Laval, M. Heitzmann, and J.-M. Fédéli, "Comparison between strip and rib soi microwaveguides for intra-chip light distribution," *Optical Materials*, vol. 27, no. 5, pp. 756–762, 2005, si-based Photonics: Towards True Monolithic Integration. [Online]. Available: https://www.sciencedirect.com/science/article/pii/S092534670400223X

- [35] T. Claes, J. Gironès Molera, K. De Vos, P. Bienstman, and R. Baets, "Label-free biosensing with silicon-on-insulator slotted racetrack resonator," in *Annual Symposium of the IEEE/LEOS Benelux Chapter*, 2008. IEEE-LEOS, 2008, pp. 23–26.
- [36] J. T. Robinson, L. Chen, and M. Lipson, "On-chip gas detection in silicon optical microcavities," *Optics Express*, vol. 16, no. 6, pp. 4296–4301, 2008.
- [37] V. Donzella, A. Sherwali, J. Flueckiger, S. M. Grist, S. T. Fard, and L. Chrostowski, "Design and fabrication of soi micro-ring resonators based on sub-wavelength grating waveguides," *Optics express*, vol. 23, no. 4, pp. 4791–4803, 2015.
- [38] E. Yablonovitch, "Photonic crystals: Towards nanoscale photonic devices," *Physics Today*, vol. 59, no. 8, pp. 54–55, 2006. [Online]. Available: https://doi.org/10.1063/1.2349736
- [39] L. Thylén, M. Qiu, and S. Anand, "Photonic crystals—a step towards integrated circuits for photonics," *ChemPhysChem*, vol. 5, no. 9, pp. 1268–1283, 2004. [Online]. Available: https://chemistry-europe.onlinelibrary.wiley.com/doi/abs/10.1002/cphc.200301075
- [40] D. M. Beggs, L. O'Faolain, and T. F. Krauss, "Accurate determination of the functional hole size in photonic crystal slabs using optical methods," *Photonics and Nanostructures Fundamentals and Applications*, vol. 6, no. 3, pp. 213–218, Dec 2008. [Online]. Available: https://www.sciencedirect.com/science/article/pii/S156944100800028X
- [41] T. Asano and S. Noda, "Photonic crystal devices in silicon photonics," *Proceedings of the IEEE*, vol. 106, no. 12, pp. 2183–2195, 2018.
- [42] P. Steglich, D. G. Rabus, C. Sada, M. Paul, M. G. Weller, C. Mai, and A. Mai, "Silicon photonic micro-ring resonators for chemical and biological sensing: A tutorial," *IEEE sensors journal*, 2021.
- [43] R. J. Van Gulik, B. M. de Boer, and P. J. Harmsma, "Refractive index sensing using a three-port interferometer and comparison with ring resonators," *IEEE Journal of Selected Topics in Quantum Electronics*, vol. 23, no. 2, pp. 433–439, 2017.
- [44] A. Yariv, "Universal relations for coupling of optical power between microresonators and dielectric waveguides," *Electronics Letters*, vol. 36, pp. 321 322, 03 2000.
- [45] K. De Vos, I. Bartolozzi, E. Schacht, P. Bienstman, and R. Baets, "Silicon-on-insulator microring resonator for sensitive and label-free biosensing," *Optics express*, vol. 15, no. 12, pp. 7610–7615, 2007.
- [46] M. Iqbal, M. A. Gleeson, B. Spaugh, F. Tybor, W. G. Gunn, M. Hochberg, T. Baehr-Jones, R. C. Bailey, and L. C. Gunn, "Label-free biosensor arrays based on silicon ring resonators and high-speed optical scanning instrumentation," *IEEE Journal of selected topics in quantum electronics*, vol. 16, no. 3, pp. 654–661, 2010.
- [47] P. Liu and Y. Shi, "Simultaneous measurement of refractive index and temperature using a dual polarization ring," *Applied optics*, vol. 55, no. 13, pp. 3537–3541, 2016.
- [48] T. Claes, W. Bogaerts, and P. Bienstman, "Experimental characterization of a silicon photonic biosensor consisting of two cascaded ring resonators based on the vernier-effect and introduction of a curve fitting method for an improved detection limit," *Optics express*, vol. 18, no. 22, pp. 22747–22761, 2010.
- [49] D.-X. Xu, A. Densmore, A. Delâge, P. Waldron, R. McKinnon, S. Janz, J. Lapointe, G. Lopinski, T. Mischki, E. Post et al., "Folded cavity soi microring sensors for high sensitivity and real time measurement of biomolecular binding," Optics express, vol. 16, no. 19, pp. 15137–15148, 2008.
- [50] K. Misiakos, I. Raptis, E. Makarona, A. Botsialas, A. Salapatas, P. Oikonomou, A. Psarouli, P. Petrou, S. Kakabakos, K. Tukkiniemi et al., "All-silicon monolithic mach-zehnder interferometer as a refractive index and bio-chemical sensor," Optics Express, vol. 22, no. 22, pp. 26803–26813, 2014.
- [51] V. Toccafondo and C. Oton, "Robust and low-cost interrogation technique for integrated photonic biochemical sensors based on mach-zehnder interferometers," *Photonics Research*, vol. 4, no. 2, pp. 57–60, 2016.

- [52] K. Misiakos, I. Raptis, A. Salapatas, E. Makarona, A. Botsialas, M. Hoekman, R. Stoffer, and G. Jobst, "Broad-band mach-zehnder interferometers as high performance refractive index sensors: Theory and monolithic implementation," Optics Express, vol. 22, no. 8, pp. 8856–8870, 2014.
- [53] X. Jiang, Y. Chen, F. Yu, L. Tang, M. Li, and J.-J. He, "High-sensitivity optical biosensor based on cascaded mach-zehnder interferometer and ring resonator using vernier effect," *Optics letters*, vol. 39, no. 22, pp. 6363–6366, 2014.
- [54] P. Xing and J. Viegas, "Broadband cmos-compatible soi temperature insensitive mach-zehnder interferometer," *Optics express*, vol. 23, no. 19, pp. 24098–24107, 2015.
- [55] R. W. Boyd and J. E. Heebner, "Sensitive disk resonator photonic biosensor," Applied optics, vol. 40, no. 31, pp. 5742–5747, 2001.
- [56] S. M. Grist, S. A. Schmidt, J. Flueckiger, V. Donzella, W. Shi, S. T. Fard, J. T. Kirk, D. M. Ratner, K. C. Cheung, and L. Chrostowski, "Silicon photonic micro-disk resonators for label-free biosensing," *Optics express*, vol. 21, no. 7, pp. 7994–8006, 2013.
- [57] M. Soltani, S. Yegnanarayanan, and A. Adibi, "Ultra-high q planar silicon microdisk resonators for chip-scale silicon photonics," *Optics express*, vol. 15, no. 8, pp. 4694–4704, 2007.
- [58] T. Ma, J. Yuan, L. Sun, Z. Kang, B. Yan, X. Sang, K. Wang, Q. Wu, H. Liu, J. Gao et al., "Simultaneous measurement of the refractive index and temperature based on microdisk resonator with two whispering-gallery modes," *IEEE Photonics Journal*, vol. 9, no. 1, pp. 1–13, 2017.
- [59] X. Wang, X. Guan, Q. Huang, J. Zheng, Y. Shi, and D. Dai, "Suspended ultra-small disk resonator on silicon for optical sensing," *Optics letters*, vol. 38, no. 24, pp. 5405–5408, 2013.
- [60] W. Shi, H. Yun, W. Zhang, C. Lin, T. K. Chang, Y. Wang, N. A. Jaeger, and L. Chrostowski, "Ultra-compact, high-q silicon microdisk reflectors," Optics express, vol. 20, no. 20, pp. 21840–21846, 2012.
- [61] S. Schmidt, J. Flueckiger, W. Wu, S. M. Grist, S. T. Fard, V. Donzella, P. Khumwan, E. R. Thompson, Q. Wang, P. Kulik, X. Wang, A. Sherwali, J. Kirk, K. C. Cheung, L. Chrostowski, and D. Ratner, "Improving the performance of silicon photonic rings, disks, and Bragg gratings for use in label-free biosensing," in *Biosensing and Nanomedicine VII*, H. Mohseni, M. H. Agahi, and M. Razeghi, Eds., vol. 9166, International Society for Optics and Photonics. SPIE, 2014, p. 91660M. [Online]. Available: https://doi.org/10.1117/12.2062389
- [62] T. Ma, J. Yuan, F. Li, L. Sun, Z. Kang, B. Yan, Q. Wu, X. Sang, K. Wang, H. Liu *et al.*, "Microdisk resonator with negative thermal optical coefficient polymer for refractive index sensing with thermal stability," *IEEE Photonics Journal*, vol. 10, no. 2, pp. 1–12, 2018.
- [63] C. Ciminelli, F. Dell'Olio, D. Conteduca, C. Campanella, and M. Armenise, "High performance soi microring resonator for biochemical sensing," *Optics & laser technology*, vol. 59, pp. 60–67, 2014.
- [64] P. Prabhathan, V. M. Murukeshan, Z. Jing, and P. V. Ramana, "Compact soi nanowire refractive index sensor using phase shifted bragg grating," *Opt. Express*, vol. 17, no. 17, pp. 15 330–15 341, Aug 2009. [Online]. Available: https://opg.optica.org/oe/abstract.cfm?URI=oe-17-17-15330
- [65] A. Yariv, Photonics: optical electronics in modern communications. 6th ed. New York: Oxford University Press, 2007., 2007, revised edition of: Optical electronics in modern communications. 5th ed., c1997.;Includes bibliographical references and indexes. [Online]. Available: https://search.library.wisc.edu/catalog/9910026655902121
- [66] R. Cheng and L. Chrostowski, "Spectral design of silicon integrated bragg gratings: A tutorial," Journal of Lightwave Technology, vol. 39, no. 3, pp. 712-729, 2020.
- [67] S. Noda, A. Chutinan, and M. Imada, "Trapping and emission of photons by a single defect in a photonic bandgap structure," *nature*, vol. 407, no. 6804, pp. 608–610, 2000.
- [68] E. Chow, A. Grot, L. W. Mirkarimi, M. Sigalas, and G. Girolami, "Ultracompact biochemical sensor built with two-dimensional photonic crystal microcavity," *Opt. Lett.*, vol. 29, no. 10, pp. 1093–1095, May 2004. [Online]. Available: https://opg.optica.org/ol/abstract.cfm?URI=ol-29-10-1093

- [69] D. Yang, C. Wang, W. Yuan, B. Wang, Y. Yang, and Y. Ji, "Silicon on-chip side-coupled high-q micro-cavities for the multiplexing of high sensitivity photonic crystal integrated sensors array," Optics Communications, vol. 374, pp. 1–7, 2016. [Online]. Available: https://www.sciencedirect.com/science/article/pii/S0030401816303017
- [70] A. S. Barough, M. Noori, and A. Abbasiyan, "Slow light-based refractive index sensor in single mode photonic crystal waveguide," *Physica Scripta*, vol. 96, no. 8, p. 085508, 2021.
- [71] M. W. McCutcheon and M. Lončar, "Design of a silicon nitride photonic crystal nanocavity with a quality factor of one million for coupling to a diamond nanocrystal," *Optics express*, vol. 16, no. 23, pp. 19136– 19145, 2008.
- [72] Y. Zhang, J. Xue, W. Liu, Y. Zhang, Z. Liu, B. Lai, J. Zhang, X. Yang, and L. Yuan, "Measurement of liquid thermo-optical coefficient based on all-fiber hybrid fpi-spr sensor," Sensors and Actuators A: Physical, vol. 331, p. 112954, 2021.
- [73] D.-X. Xu, M. Vachon, A. Densmore, R. Ma, S. Janz, A. Delâge, J. Lapointe, P. Cheben, J. Schmid, E. Post *et al.*, "Real-time cancellation of temperature induced resonance shifts in soi wire waveguide ring resonator label-free biosensor arrays," *Optics express*, vol. 18, no. 22, pp. 22867–22879, 2010.
- [74] M. Uenuma and T. Motooka, "Temperature-independent silicon waveguide optical filter," *Optics letters*, vol. 34, no. 5, pp. 599–601, 2009.
- [75] Y. Zhang, J. Zou, and J.-J. He, "Temperature sensor with enhanced sensitivity based on silicon mach-zehnder interferometer with waveguide group index engineering," *Optics Express*, vol. 26, no. 20, pp. 26 057–26 064, 2018.
- [76] B. Guha, A. Gondarenko, and M. Lipson, "Minimizing temperature sensitivity of silicon mach-zehnder interferometers," Optics express, vol. 18, no. 3, pp. 1879–1887, 2010.
- [77] S. Dwivedi, H. D'heer, and W. Bogaerts, "Maximizing fabrication and thermal tolerances of all-silicon fir wavelength filters," *IEEE Photonics Technology Letters*, vol. 27, no. 8, pp. 871–874, 2015.
- [78] Z. Li, J. Zou, H. Zhu, B. T. T. Nguyen, Y. Shi, P. Y. Liu, R. C. Bailey, J. Zhou, H. Wang, Z. Yang et al., "Biotoxoid photonic sensors with temperature insensitivity using a cascade of ring resonator and mach-zehnder interferometer," ACS sensors, vol. 5, no. 8, pp. 2448–2456, 2020.
- [79] J. Komma, C. Schwarz, G. Hofmann, D. Heinert, and R. Nawrodt, "Thermo-optic coefficient of silicon at 1550 nm and cryogenic temperatures," *Applied Physics Letters*, vol. 101, no. 4, p. 041905, 2012.
- [80] N. Lin, L. Jiang, S. Wang, L. Yuan, and Q. Chen, "Simultaneous measurement of refractive index and temperature using a microring resonator," *Chinese Optics Letters*, vol. 10, no. 5, p. 052802, 2012.
- [81] M. Bahadori, A. Gazman, N. Janosik, S. Rumley, Z. Zhu, R. Polster, Q. Cheng, and K. Bergman, "Thermal rectification of integrated microheaters for microring resonators in silicon photonics platform," *Journal of Lightwave Technology*, vol. 36, no. 3, pp. 773–788, 2017.
- [82] K. Padmaraju and K. Bergman, "Resolving the thermal challenges for silicon microring resonator devices," *Nanophotonics*, vol. 3, no. 4-5, pp. 269–281, 2014.
- [83] K. B. Gylfason, C. F. Carlborg, A. Kaźmierczak, F. Dortu, H. Sohlström, L. Vivien, C. A. Barrios, W. van der Wijngaart, and G. Stemme, "On-chip temperature compensation in an integrated slotwaveguide ring resonator refractive index sensor array," Optics express, vol. 18, no. 4, pp. 3226–3237, 2010.
- [84] A. Densmore, M. Vachon, D.-X. Xu, S. Janz, R. Ma, Y.-H. Li, G. Lopinski, A. Delâge, J. Lapointe, C. Luebbert et al., "Silicon photonic wire biosensor array for multiplexed real-time and label-free molecular detection," Optics letters, vol. 34, no. 23, pp. 3598–3600, 2009.
- [85] A. W. Poon, X. Luo, F. Xu, and H. Chen, "Cascaded microresonator-based matrix switch for silicon on-chip optical interconnection," *Proceedings of the IEEE*, vol. 97, no. 7, pp. 1216–1238, 2009.
- [86] P. Steglich, D. G. Rabus, C. Sada, M. Paul, M. G. Weller, C. Mai, and A. Mai, "Silicon photonic microring resonators for chemical and biological sensing: A tutorial," *IEEE Sensors Journal*, vol. 22, no. 11, pp. 10089–10105, 2022.

- [87] "High performance tunable laser tsl-570," https://www.santec.com/dcms_media/other/instruments_TSL-570-C-E.pdf.
- [88] "Fiber-optic receiver, 900-1700 nm ingaas detector, 25 khz to 125 mhz, fc," https://www.newport.com/p/1811-FC-AC.
- [89] J. Hu, X. Sun, A. Agarwal, and L. C. Kimerling, "Design guidelines for optical resonator biochemical sensors," *JOSA B*, vol. 26, no. 5, pp. 1032–1041, 2009.
- [90] X. Zhang, J. Qiu, J. Zhao, X. Li, and L. Liu, "Complex refractive indices measurements of polymers in infrared bands," *Journal of Quantitative Spectroscopy and Radiative Transfer*, vol. 252, p. 107063, 2020.
- [91] Z. Zhu, L. Liu, Y. Liu, Y. Zhang, and Y. Zhang, "Surface-plasmon-resonance-based optical-fiber temperature sensor with high sensitivity and high figure of merit," *Optics Letters*, vol. 42, no. 15, pp. 2948–2951, 2017.
- [92] "Inorganic-organic hybrid polymers (ormocer®s) for micro systems technology," https://www.isc. fraunhofer.de/content/dam/isc/de/documents/Publikationen/Inorganic-organic_hybrid_polymers_ ORMOCER for micro systems technology.pdf.
- [93] "Process design kit (pdk)," https://www.cornerstone.sotonfab.co.uk/mpw-design-rules/process-design-kit-pdkf.
- [94] "Core and cladding systems for waveguiding," https://www.microresist.de/wp-content/uploads/2020/02/PI_waveguides_materials_2015.
- [95] S. K. Selvaraja, P. Jaenen, W. Bogaerts, D. Van Thourhout, P. Dumon, and R. Baets, "Fabrication of photonic wire and crystal circuits in silicon-on-insulator using 193-nm optical lithography," *Journal of lightwave technology*, vol. 27, no. 18, pp. 4076–4083, 2009.
- [96] T. Horikawa, D. Shimura, S.-H. Jeong, M. Tokushima, K. Kinoshita, and T. Mogami, "The impacts of fabrication error in si wire-waveguides on spectral variation of coupled resonator optical waveguides," *Microelectronic Engineering*, vol. 156, pp. 46–49, 2016.
- [97] S. K. Selvaraja, W. Bogaerts, P. Dumon, D. Van Thourhout, and R. Baets, "Subnanometer linewidth uniformity in silicon nanophotonic waveguide devices using cmos fabrication technology," *IEEE Journal of Selected Topics in Quantum Electronics*, vol. 16, no. 1, pp. 316–324, 2009.
- [98] A. Li, T. Van Vaerenbergh, P. De Heyn, P. Bienstman, and W. Bogaerts, "Backscattering in silicon microring resonators: a quantitative analysis," *Laser & Photonics Reviews*, vol. 10, no. 3, pp. 420–431, 2016.
- [99] W. J. Westerveld, "Silicon photonic micro-ring resonators to sense strain and ultrasound," 2014.
- [100] M. S. Nawrocka, T. Liu, X. Wang, and R. R. Panepucci, "Tunable silicon microring resonator with wide free spectral range," Applied physics letters, vol. 89, no. 7, p. 071110, 2006.
- [101] X. Guan, Y. Ding, and L. H. Frandsen, "Ultra-compact broadband higher order-mode pass filter fabricated in a silicon waveguide for multimode photonics," *Optics letters*, vol. 40, no. 16, pp. 3893–3896, 2015.
- [102] A. Yusop, A. Kassir, A. A. Ehsan, and S. Shaari, "Determination of thermo-optic coefficient of a uv curable polymer using prism coupling technique," in 2004 IEEE International Conference on Semiconductor Electronics. IEEE, 2004, pp. 4–pp.
- [103] "Uv-curable hybrid polymers for micro optical components," https://www.microresist.de/wp-content/uploads/2021/07/flyer_hybridpolymers_2021_kl.pdf.
- [104] F. C. Krebs, "Fabrication and processing of polymer solar cells: A review of printing and coating techniques," Solar energy materials and solar cells, vol. 93, no. 4, pp. 394–412, 2009.
- [105] E. D. Patamia, N. A. Ostrovsky-Snider, and A. R. Murphy, "Photolithographic masking method to chemically pattern silk film surfaces," *ACS applied materials & interfaces*, vol. 11, no. 37, pp. 33612–33619, 2019.

- [106] S. Wang, A. Kallur, and A. Goshu, "Fabrication and characterization of pdms thin film," in *Organic Photonic Materials and Devices XIII*, vol. 7935. SPIE, 2011, pp. 109–114.
- [107] J. S. Park, R. Cabosky, Z. Ye, and I. I. Kim, "Investigating the mechanical and optical properties of thin pdms film by flat-punched indentation," *Optical Materials*, vol. 85, pp. 153–161, 2018.
- [108] Z. Xia, A. A. Eftekhar, M. Soltani, B. Momeni, Q. Li, M. Chamanzar, S. Yegnanarayanan, and A. Adibi, "High resolution on-chip spectroscopy based on miniaturized microdonut resonators," *Optics express*, vol. 19, no. 13, pp. 12356–12364, 2011.
- [109] M. Soltani, Q. Li, S. Yegnanarayanan, and A. Adibi, "Ultimate miniaturization of single and coupled resonator filters in silicon photonics," in 2009 Conference on Lasers and Electro-Optics and 2009 Conference on Quantum electronics and Laser Science Conference. IEEE, 2009, pp. 1–2.

Appendix A

CMOS Fabrication Process Flow

The CMOS process flow for fabricating the photonic integrated circuit of the distributed force sensor is shown in Figure A.1. These fabrication steps are as follows:

- 1. The fabrication starts with a $200 \, nm$ silicon-on-insulator wafer with a top silicon layer thickness of $220 \, nm$
- 2. Photoresist layer is deposited and patterned for fabricating the out-of-plane grating couplers only.
- 3. A $70 \, nm$ etch is performed.
- 4. Photoresist layer for fabricating the out-of-plane grating couplers is removed.
- 5. SiO_2 hard mask is deposited on top of the die.
- 6. Photoresist layer is deposited and patterned for fabricating both the strip waveguides and the ring resonators.
- 7. The hard mask is being etched.
- 8. Remove photoresist layer for patterning the hard mask.
- 9. Using the etched hard mask, a 120 nm (intermediate) etch is performed, leaving a silicon slab layer of 100 nm thick.
- 10. Photoresist is patterned on top of the ring resonator to protect the inner slab layer from getting etched. It should be checked whether the photoresist material gets into the gap between the strip waveguide and the ring resonator.
- 11. The exposed silicon layers are etched to the silicon substrate.
- 12. The remaining photoresist layer is removed. The out-of-plane grating couplers, strip waveguides and ring resonators are fabricated. Only the SiO_2 hard mask is still remaining

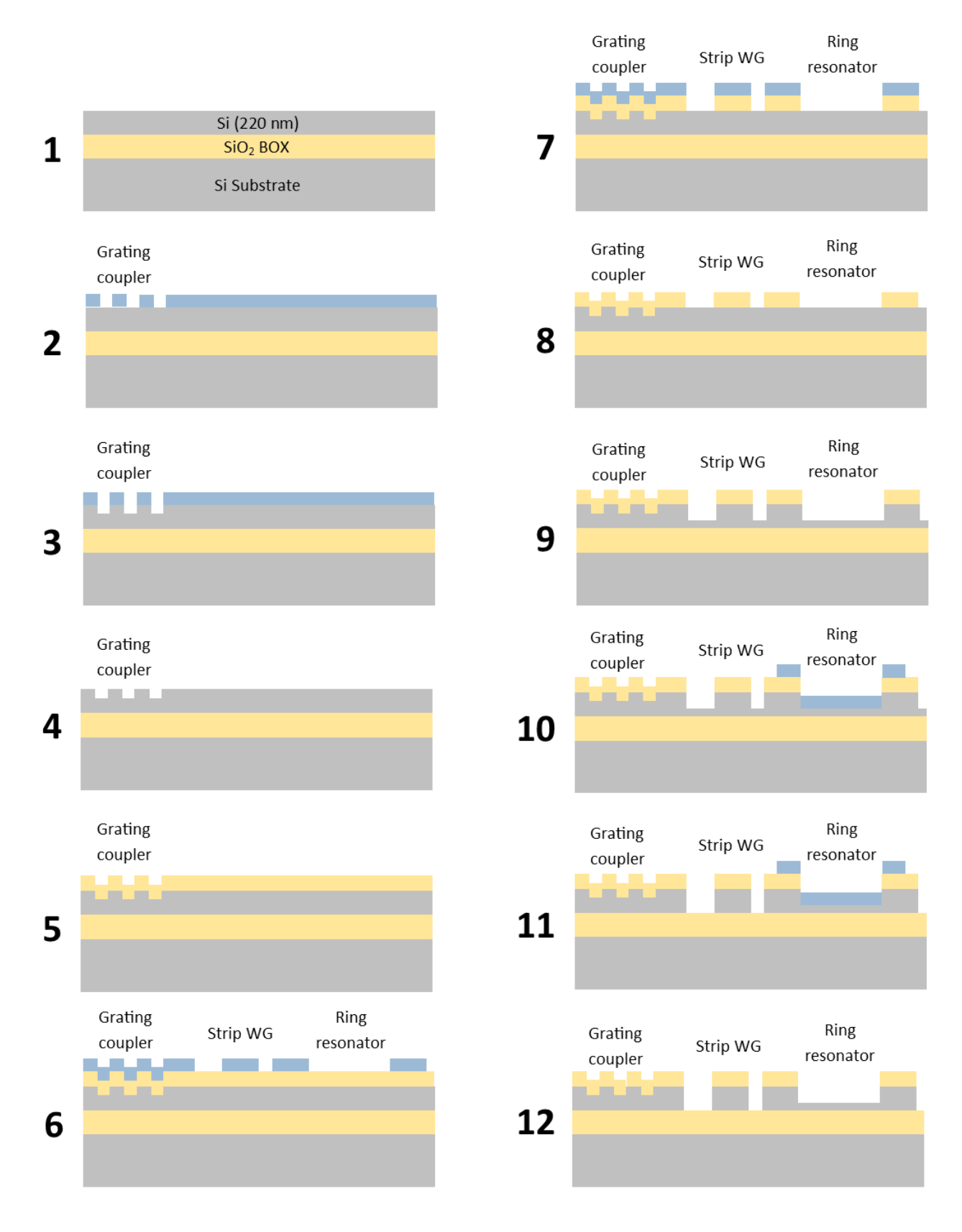


Figure A.1: CMOS fabrication process flow for fabricating the PIC based on Cornerstone's defined processes [93]

Appendix B

Polymer Cladding Fabrication Process Flow

The process flow for fabricating polymer thin film layers on top of both the force and reference sensors is shown in Figure B.1. These fabrication steps are as follows:

- 1. The fabrication process starts with a fabricated photonic integrated circuit of which the hard mask has been removed.
- 2. Ormocore hybrid polymer resin is spin coated on top of the entire die.
- 3. Photoresist mask is applied and patterned to locally UV cure Ormocore at the reference sensors region.
- 4. UV curing Ormocore.
- 5. Photoresist mask is removed and the uncured Ormocore resin is washed away.
- 6. PDMS is spin coated on top of the entire chip. Note that there is local PDMS accumulation on top of the Ormocore layer. This is not a problem as long as the PDMS film layer at the force sensors are uniform in thickness.
- 7. Photoresist mask is applied and patterned to locally UV cure PDMS at the force sensors region.
- 8. PDMS resin is UV cured.
- 9. The photoresist mask is removed and the remaining uncured PDMS resin is washed away.

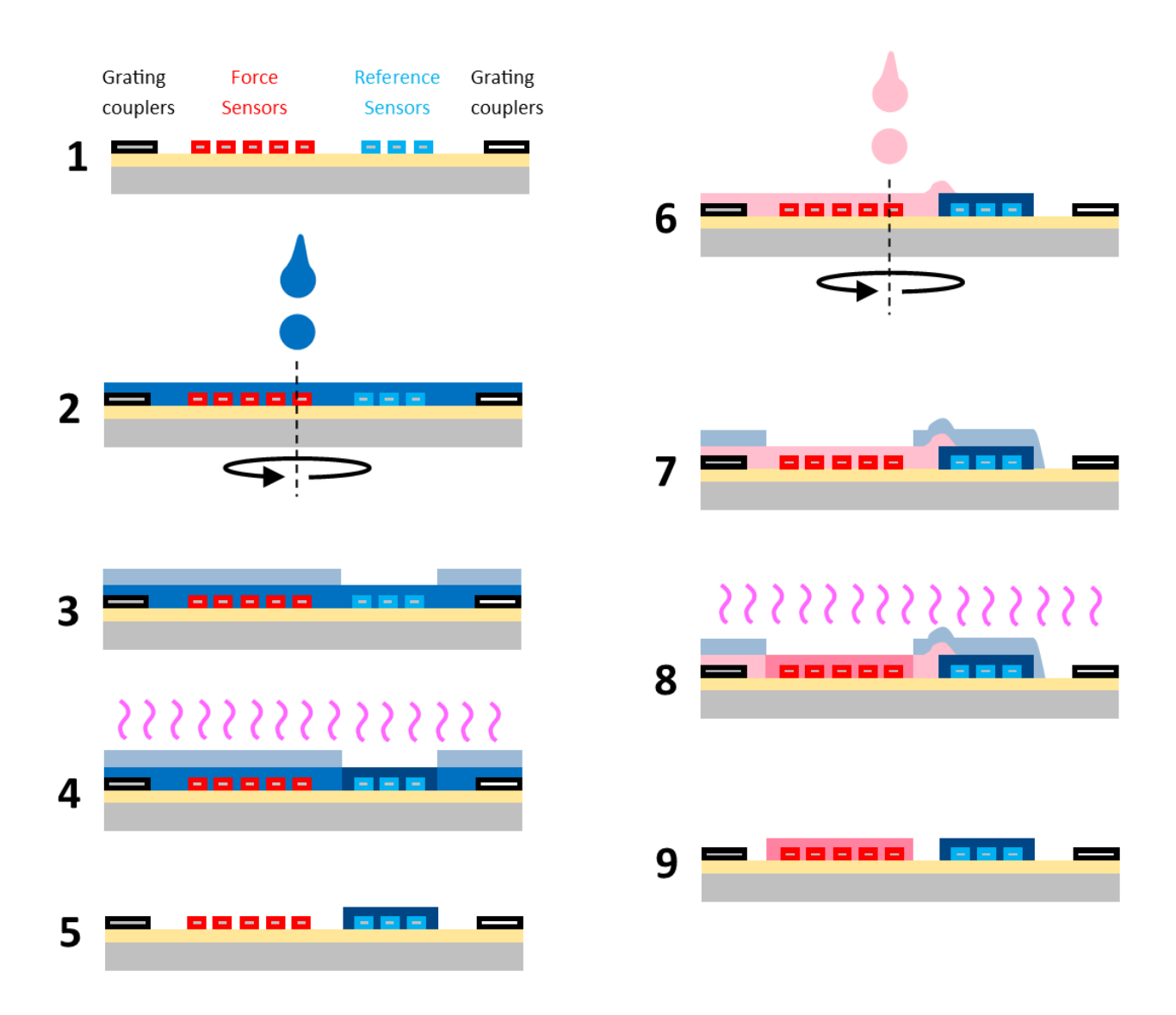


Figure B.1: Fabrication of polymer thin film layers on top of the photonic integrated circuit.